

Measurement of Soot Precursor Particles under Atmospheric and Low Pressure Conditions by means of Time-Of-Flight Mass Spectrometry

A thesis accepted by the Faculty of Aerospace Engineering and Geodesy
of the Universität Stuttgart in partial fulfilment of the requirements for
the degree of Doctor of Engineering Sciences (Dr.-Ing.)

by

Dipl.-Ing. Tania González Baquet

born in Avilés (Spain)

Main referee: Prof. Dr.-Ing. M. Aigner

Co-referee: Prof. Dr.-Ing. H. Seifert

Date of defence: 06.03.2009

Institute of Combustion Technology

Universität Stuttgart

2009

To Miguel

Y ahora...

¡dejemos que el futuro nos sorprenda!

Acknowledgements

This work has been carried out at the Institute of Combustion Technology of the German Aerospace Center in Stuttgart (Germany) under the direction of Prof. Dr. M. Aigner. I would like to thank him in the first instance for enabling and supporting this research project. I would like also to thank Prof. Dr. H. Seifert from the Institute for Technical Chemistry (Thermal Waste Treatment Division) of the Forschungszentrum Karlsruhe (Germany) for the friendly acceptance of the co-assessment of this thesis.

I wish to express my gratitude in particular to Dr. H.-H. Grotheer, supervisor of this work and responsible for the nanoparticle research at the Institute of Combustion Technology of the German Aerospace Center in Stuttgart. I thank him for his constant support, his exhaustless motivation and his thoughtful advice and knowledge. My thanks also to H. Pokorny for his assistance during the construction of the test bench and during the realization of the measurements. My thanks also to Dr. R. Stirn and S. R. Kanjarkar for carrying out the LII and EEPS measurements, respectively.

I am very grateful to Dr. C. Baumstark-Khan from the Institute of Aerospace Medicine (Radiation Biology) of the German Aerospace Center in Cologne (Germany) and her team, who kindly carried out the necessary tests to evaluate the toxicological potential of combustion generated soot precursor particles.

And last but not least, thanks to all my colleagues at the Institute of Combustion Technology of the German Aerospace Center in Stuttgart for the pleasant working atmosphere and above all for the friendly get-together.

Finally, I would like to thank my family for their understanding and support throughout these years in Germany.

I dedicate this thesis to Miguel. I thank him for his love, support and never-ending patience.

Contents

Symbols, Abbreviations and Constants	9
Abstract	12
Zusammenfassung	14
1. Introduction	16
1.1. The Role of Combustion in today's society	16
1.2. Motivation and Aim of this Work	20
2. Experimental Set-Up	22
2.1. Time-Of-Flight Mass Spectrometer	22
2.1.1. Measurement Principle	22
2.1.2. Arrangement and Function of the Different Electric Fields	23
2.2. Sampling Procedure	25
2.2.1. Sampling and Sample Inlet System	25
2.2.2. Molecular Beam Inlet System	27
2.2.3. Cross and Axial Arrangement	29
2.3. Laser System	31
2.4. Signal Processing	32
2.5. Synchronization	34
3. Burners and Measuring Procedure	35
4. Sampling Line Effects	38
4.1. Coagulation	38
4.2. Temperature Effects	43
5. Photo Ionization	48
5.1. Fragmentation Threshold	49
5.2. Fullerenes	53
6. Flame Measurements	55
6.1. Particle Mass Distributions in Premixed Flames	55
6.1.1. Premixed Ethylene/Air Flames at Atmospheric Pressure	55
Variation of the Equivalence Ratio	55
Variation of the Height above the Burner	58
Photo Ionization Behavior	59
Particles outside of the Flame	64
6.1.2. Premixed Ethylene/Oxygen Flames at Low Pressure	69
Variation of the Equivalence Ratio	69

Variation of the Operation Pressure	71
6.2. Conclusions	74
7. Engine Exhaust Measurements	76
8. Discussion	83
8.1. Source of Errors of the Mass Spectrometric Measurements	83
8.1.1. Reproducibility	83
8.1.2. Systematic Errors	84
8.2. Particle Size Distributions: Comparison with other Particle Sizing Techniques	86
8.3. Limitation of MS for the Detection of very large Masses ($m > 100000 u$) .	90
8.4. Improvement of the Detection of Soot Precursor Particles ($m < 100000 u$) .	92
8.5. Identification of Modes A and B: Chemical and Physical Composition . . .	93
8.6. Lower Φ Limit for Particle Generation	98
Appendices	102
A. Wet Samples of Soot Precursor Particles	103
A.1. Preparation of Wet Samples for Calibration and Toxicological Analysis . .	103
A.1.1. Experimental Set-Up	103
A.1.2. Detailed Sampling Procedure and Parametric Study	105
A.2. Calibration	108
A.2.1. Method	108
A.2.2. Results	109
A.3. Toxicological Analysis	113
A.3.1. Method	113
A.3.2. Results	115
B. Other Sampling Line Effects	121
B.1. Influence of the Residence Time	121
B.2. Particle Losses	124
B.2.1. General Considerations	124
B.2.2. Variation of the Stoichiometry	126
List of Figures	134
List of Tables	138
Bibliography	139

Symbols, Abbreviations and Constants

Symbols

Abs_{rel}	Relative absorbance
Abs_0	Absorbance of the untreated bacterial culture
Abs_i	Absorbance of the treated bacterial culture
a	Distance between nozzle and skimmer; also absorption cross section
b	Distance between skimmer and ionization point
C	Mass concentration of soot precursor particles
C_c	Slip correction factor
D	Diffusion coefficient
d_i	Inner diameter of the sampling line
d_{Nozzle}	Nozzle diameter (capillary or narrowest section)
$d_{Skimmer}$	Skimmer diameter
d_{Valve}	Valve diameter
d_p	Particle diameter
E	Expansion ratio
E_0	Energy of the ground state
E_1	Energy of an intermediate (excited) state
F_i	Luminescence response induction factor
Flu_{rel}	Relative fluorescence
Flu_0	Fluorescence of the untreated bacterial culture
Flu_i	Fluorescence of the treated bacterial culture
f	Focal length
H	Laser beam height
HAB	Height above burner
h_f	Focused laser beam width
I	Ionization laser power density
K	Coagulation coefficient
K_{Wall}	Wall loss coefficient
L	Sampling line length
Lux_{rel}	Relative luminescence
Lux_0	Peak luminescence of the untreated bacterial culture
Lux_i	Peak luminescence of the treated bacterial culture
M	Mean particle mass in grams
M_{TOC}	Total organic carbon mass "corrected"
m	Mean particle mass in atomic mass units
\dot{m}	Mass flow rate
m_i	Ion mass
N	Particle number concentration

N_{E_1}	Population of an intermediate (excited) state
N_{in}	Particle number concentration of entering particles
N_{out}	Particle number concentration of exiting particles
n	Ionization order
\dot{n}	Molar flow rate
$n_{mode A}$	Ionization order of mode A particles
$n_{mode B}$	Ionization order of mode B particles
P	Penetration
p	Pressure
\bar{p}	Average pressure
p_{Flame}	Flame pressure
p_L	Pressure at the end of the sampling line
p_0	Pressure at the tip of the probe
p_x	Pressure at x
Re	Reynold's number
r	Radius
r_i	Radius of the sampling line
r_v	Virtual radius
S	Signal intensity
S_i	Original cross section of the sampling line
S_{Nozzle}	Nozzle throat area
S_v	Virtual cross section
s	Flight distance
T	Temperature
\bar{T}	Average temperature
∇T	Temperature gradient
T_{Flame}	Flame temperature
T_L	Temperature at the end of the sampling line
T_N	Temperature at normal conditions
T_0	Temperature at the tip of the probe
T_p	Absolute particle temperature
t	Time of flight or residence time
U	Acceleration voltage
\dot{V}	Volumetric flow rate
$V_{Gas\ sample}$	Gas sample volume under normal conditions
V_{th}	Velocity of thermophoresis
x	Axial distance, length or radial distance
x_{th}	Radial distance covered due to thermophoresis
z	Ion charge

Greek Symbols

β	Coagulation correction factor
Φ	Equivalence ratio
λ	Wavelength; also gas mean free path
μ	Deposition parameter

γ	Specific heat ratio
η	Dynamic viscosity
ν	Frequency
ρ	Density
σ	Standard deviation

Abbreviations

ArF	Laser gas mixture of argon and fluorine in neon
AFM	Atomic force microscopy
DMA	Differential mobility analyzer
EEPS	Engine exhaust particle sizer
EI	Electron impact ionization
FWHM	Full width at half maximum
HPLC	High performance liquid chromatography
LII	Laser-induced incandescence
LMMS	Laser microprobe mass spectrometry
MALDI	Matrix-assisted laser desorption/ionization
MCP	Multi-channel plates
MPI	Multiphoton ionization
MS	Mass spectrometer
SWITCH	Salmonella <u>w</u> eighting of <u>i</u> nduced <u>t</u> oxicity (genotoxicity) and <u>c</u> ytotoxicity for <u>h</u> uman health - Test
TEM	Transmission electron microscopy
TOC	Total organic carbon
TOF-MS	Time-of-flight mass spectrometer
PAH	Polycyclic aromatic hydrocarbon
PAK	Polyzyklischer aromatischer Kohlenwasserstoffe (see PAH)
PSDF	Particle size distribution function
SAXS	Small-angle X-ray scattering
SMPS	Scanning mobility particle sizer

Constants

$N_A = 6.02214 \cdot 10^{23} \text{ mol}^{-1}$	Avogadro's constant
$h = 6.62608 \cdot 10^{-34} \text{ J s}$	Planck's constant
$k = 1.38066 \cdot 10^{-23} \text{ JK}^{-1}$	Boltzmann's constant
$R = 8.31451 \text{ JK}^{-1}\text{mol}^{-1}$	Gas constant

Abstract

During the last decades a great progress has been achieved in the understanding of the combustion of hydrocarbons. The gas phase reactions governing the first steps in the combustion process, e.g the formation of small aromatic rings and large polycyclic aromatic hydrocarbons (PAH), are well understood. The existing models describing the growth of soot particles and the formation of soot aggregates from small soot particles of three to five nanometers are widely accepted, as well. However, the so-called inception, i.e. the mechanism leading to the formation of the first solid particles (soot precursor particles) from gas phase molecules, is still a controversial issue. This is mainly due to the lack of adequate experimental techniques capable of detecting particles in the low nanometer range like those created in the nucleation process in flames. At present most of the combustion models stress the importance of PAH formation and growth in the soot formation process. In this context, it is considered that the first solid particles arise as PAH clusters with a layered structure, as described by Dobbins et al. [25, 32, 34]. Other models, however, propose a soot formation mechanism based on the formation of large three dimensional structures without crystallinity. In this case soot precursor particles are described as networks of aromatic-aliphatic-linked structures as postulated by D'Alessio et al. [27, 28, 80].

In the present work, the detection and characterization of soot precursor particles, as transition species between gas phase molecules and solid soot particles in the combustion process, is attempted by means of mass spectrometry. To this end a "custom-built" reflectron time-of-flight mass spectrometer of high sensitivity and with a large mass range up to several hundreds of thousands atomic mass units is used. Measurements are carried out in different premixed ethylene laboratory flames at different pressures and in a wide range of stoichiometries. Additionally, the exhaust of a gasoline and a diesel engine is investigated. These measurements require the development of a sampling technique capable of transporting the sample from atmospheric conditions to the high vacuum of the mass spectrometer. The resulting fast pulsed sampling system minimizes undesirable sampling line effects, such as coagulation, while it enables the generation of an optimized molecular beam. Photo ionization of the sample is provided by an excimer laser operated with a mixture of argon and fluorine in neon which generates a laser wavelength of 193 nanometers. In order to calibrate the time-of-flight mass spectrometer, aqueous solutions of isolated soot precursor particles are collected. The toxicity of these samples is also investigated.

The main findings of this work can be summarized as follows:

1. Different types of soot precursor particles can coexist in the flame.

For the first time two different types of soot precursor particles with diameters ranging from approximately one to five nanometers have been simultaneously detected. Consequently, the observed particle mass distributions of soot precursor particles are under certain conditions bimodal. When considering soot particles, up to three different particle

modes can be distinguished. The different soot precursor particle modes, in the following referred to as mode A and mode B, show different features. Thus, the existence of at least two different types of soot precursor particles is postulated.

Mode A particles are found in a wide range of flame stoichiometries. They are characterized by an ionization order close to two and show a fragmentation threshold of around 0.12 MW/cm^2 . These particles are considered amorphous, more characteristic of low temperature flames and associated to the soot precursor particles described by D'Alessio et al.. Mode B particles are only observed in a limited stoichiometric range associated with rather high flame temperatures. Mode B particles show an ionization order close to one and a relatively high fragmentation threshold close to 2.24 MW/cm^2 . These particles are considered to be similar to the ones described by Dobbins et al., i.e. stacks of planar PAHs.

2. Soot precursor particles, although considered to be very reactive, can survive the flame and be emitted.

Soot precursor particles should be considered as an independent particle class and not only as intermediate species in the combustion process. Since health effects are particularly pronounced in the case of very small particles, the emission of soot precursor particles should be taken into account.

3. Soot precursor particles are found in significant amounts only at flame stoichiometries above the soot threshold.

The lower stoichiometric limit for particle generation is still an issue discussed in the combustion community. All results of this study indicate that the onset of particle formation takes place at flame stoichiometries close to the soot threshold. Consequently, the emission of soot precursor particles seems not to be an outstanding problem in the case of gasoline combustion engines, since the latter work under fairly stoichiometric burning conditions and are characterized by a homogeneous fuel-mixture. This is confirmed by the measurements carried out in the exhaust gas of a gasoline generator. Conventional diesel engines work under globally lean burning conditions but are characterized by a heterogeneous fuel-mixture. Consequently, high particle emissions are expected. The measurements carried out in the exhaust gas of a diesel generator, however, show negligible soot precursor particle emissions. In this case soot precursor particles are oxidized due to the excess of oxygen in the exhaust gas. Soot precursor particle losses due to coagulation with soot particles are also expected.

This work demonstrates the utility of time-of-flight mass spectrometry for the detection and study of soot precursor particles. The experimental data presented in this thesis provide new information about the transition region between gas phase molecules and soot particles in the combustion process. This improves the understanding of the soot formation process and stimulates the revision of current combustion models.

Zusammenfassung

Seit einigen Jahrzehnten wird die Verbrennung von Kohlenwasserstoffe immer besser verstanden. Die den ersten Schritten der Verbrennung zugrundeliegenden Gasreaktionen wie die Bildung kleiner aromatischer Ringe und großer polyzyklischer aromatischer Kohlenwasserstoffe (PAK) sind weitgehend bekannt. Ebenso weithin akzeptiert sind die existierenden Modelle zur Beschreibung des Wachstums von Rußpartikeln und der Bildung von Rußaggregaten aus kleinen Rußpartikeln von drei bis fünf Nanometer. Der Mechanismus, welcher zur Bildung der ersten Feststoffpartikel (Rußvorläuferteilchen) aus gasförmigen Molekülen führt, die sogenannte "inception", ist jedoch immer noch unstritten. Dies ist hauptsächlich dem Fehlen adäquater experimentelle Messtechniken geschuldet, die Partikel im niederen Nanometerbereich nachweisen bzw. deren Entstehungsprozess in der Flamme verfolgen können. Derzeit betonen die meisten Verbrennungsmodelle den Einfluss der PAK-Bildung und des PAK-Wachstums in dem Rußentstehungsprozess. In diesem Zusammenhang wird angenommen, dass die ersten festen Partikel, wie von Dobbins et al. beschrieben [25, 32, 34], in Form von PAK-Clustern mit einer Schichtstruktur auftauchen. Andere Theorien schlagen einen Rußentstehungsprozess vor, der auf der Bildung großer drei-dimensionaler Strukturen ohne Kristallinität beruht. In diesem Fall werden Rußvorläuferteilchen als Netzwerke von aromatisch-aliphatisch-verbundenen Strukturen beschrieben, wie von D'Alessio et al. postuliert [27, 28, 80].

In der vorliegenden Arbeit werden der Nachweis und die Charakterisierung von Rußvorläuferteilchen mit Hilfe der Massenspektroskopie angestrebt. Hierfür wird ein speziell angefertigter hochempfindlicher Reflectron-Flugzeit-Massenspektrometer mit einem breiten Massenbereich bis zu mehreren hunderttausend atomaren Masseneinheiten eingesetzt. Die Messungen werden an verschiedenen vorgemischten Ethylen-Laborflammen bei unterschiedlichen Drücken und in einem weiten stöchiometrischen Bereich durchgeführt. Zusätzlich wird das Abgas eines Otto- und eines Dieselmotors untersucht. Alle diese Messungen setzen die Entwicklung einer Probenahmetechnik voraus, die es ermöglicht, Proben aus atmosphärischen Umgebungsbedingungen ins Hochvakuum des Massenspektrometers zu transportieren. Das verwendete schnell gepulste Probenahmesystem minimiert einerseits unerwünschten Einflüsse wie Koagulation, wohingegen es andererseits die Bildung eines optimierten Molekularstrahls fördert. Zur Ionisation der Probe wird ein Excimer-Laser verwendet, der mit einer Mischung aus Argon und Fluor in Neon betrieben wird. Die Photoionisation erfolgt somit bei einer Wellenlänge von 193 Nanometer. Zur Kalibrierung des Flugzeit-Massenspektrometers werden wässrige Lösungen isolierter Rußvorläuferteilchen gesammelt. Die Giftigkeit dieser Proben ist ebenfalls Gegenstand der Untersuchung.

Die wesentlichen Erkenntnisse dieser Arbeit können wie folgt zusammengefasst werden:

1. In der Flamme treten unterschiedliche Typen von Rußvorläuferteilchen gemeinsam auf.

Erstmalig konnten zwei unterschiedliche Sorten von Rußvorläuferteilchen mit Durchmessern

von ungefähr eins bis fünf Nanometer simultan nachgewiesen werden. Folglich ist die beobachtete Massenverteilung der Rußvorläuferteilchen unter bestimmten experimentellen Bedingungen bimodal. Bei Betrachtung der Rußpartikel können bis zu drei Partikelmodi unterschieden werden. Die unterschiedlichen Modi der Rußvorläuferteilchen (im Folgenden so genannten "Mode A" und "Mode B") zeigen unterschiedliche Eigenschaften. Daher wird die Existenz von mindestens zwei unterschiedlichen Typen von Rußvorläuferteilchen postuliert.

Die "Mode A"-Teilchen finden sich in einem weiten stöchiometrischen Bereich und treten vor allem in Niedertemperaturflammen auf. Sie zeichnen sich durch eine Ionisationsordnung nahe zwei aus und zeigen eine Fragmentierungsschwelle von etwa $0,12 \text{ MW/cm}^2$. Diese Partikel werden als eher amorph betrachtet und mit den von D'Alessio et al. beschriebenen Rußvorläuferteilchen in Verbindung gebracht.

Die "Mode B"-Teilchen hingegen können nur in einem begrenzten stöchiometrischen Bereich in Verbindung mit hohen Flammentemperaturen beobachtet werden. Diese Partikel zeigen eine Ionisationsordnung nahe eins und eine relativ hohe Fragmentierungsschwelle oberhalb $2,24 \text{ MW/cm}^2$. Die "Mode B"-Teilchen werden als den von Dobbins et al. beschriebenen Teilchen ähnlich betrachtet, d.h. als Schichten ebener PAHs.

2. Rußvorläuferteilchen können trotz ihrer Reaktivität auch außerhalb von Flammen existieren und daher emittiert werden.

Rußvorläuferteilchen sollten als eigenständige Partikelklasse betrachtet werden, nicht nur als Übergangsart im Verbrennungsprozess. Da Gesundheitsaspekte im Fall von Feinstaubpartikeln besonders betont werden, sollte die Emission von Rußvorläuferteilchen in Betracht gezogen werden.

3. Rußvorläuferteilchen werden in deutlichen Mengen nur bei Stöchiometrien oberhalb der Rußgrenze gefunden.

Die untere stöchiometrische Grenze für die Partikelentstehung ist immer noch in der Verbrennungs-community umstritten. In dieser Arbeit zeigen alle Ergebnisse, dass Partikel nur bei Flammenstöchiometrien nahe der Rußgrenze entstehen. Da Ottomotoren unter annähernd stöchiometrischen Verbrennungsbedingungen arbeiten und sich durch ein homogenes Kraftstoff-Luft-Gemisch auszeichnen, scheint der Ausstoß von Rußvorläuferteilchen in diesem Fall kein vordringliches Problem zu sein. Dies wird von im Abgas vom Ottomotor durchgeführten Messungen bekräftigt. Dieselmotoren arbeiten unter mageren Verbrennungsbedingungen aber zeichnen sich durch ein heterogenes Kraftstoff-Luft-Gemisch aus, so dass in allgemein höhere Partikelemissionen erwartet werden. Dennoch konnte anhand der durchgeführten Abgasmessungen am Dieselmotor nur ein vernachlässigbarer Ausstoß von Rußvorläuferteilchen festgestellt werden. In diesem Fall werden Rußvorläuferteilchen infolge des Sauerstoffüberschusses im Abgas oxidiert. Verluste von Rußvorläuferteilchen sind auch aufgrund von Koagulation mit Rußpartikeln zu erwarten.

Diese Arbeit zeigt, dass Flugzeit-Massenspektrometrie für den Nachweis und die Untersuchung von Rußvorläuferteilchen prinzipiell geeignet ist. Die hiermit vorgelegten experimentelle Daten enthalten neue Erkenntnisse über die Übergangsregion zwischen Gas-molekülen und Rußpartikeln im Verbrennungsprozess. Dies verbessert das Verständnis des Rußentstehungsprozesses und fördert die Überprüfung bestehender Verbrennungsmodelle.

1. Introduction

1.1. The Role of Combustion in today's society

Fire, and thus combustion, has accompanied the development of the human society since the beginning of time.

According to the U.S. Energy Information Administration, 86% of the world energy demand of 2005 was supplied by fossil fuels (see figure 1.1). This gives a clear idea of the crucial role of combustion in today's society.

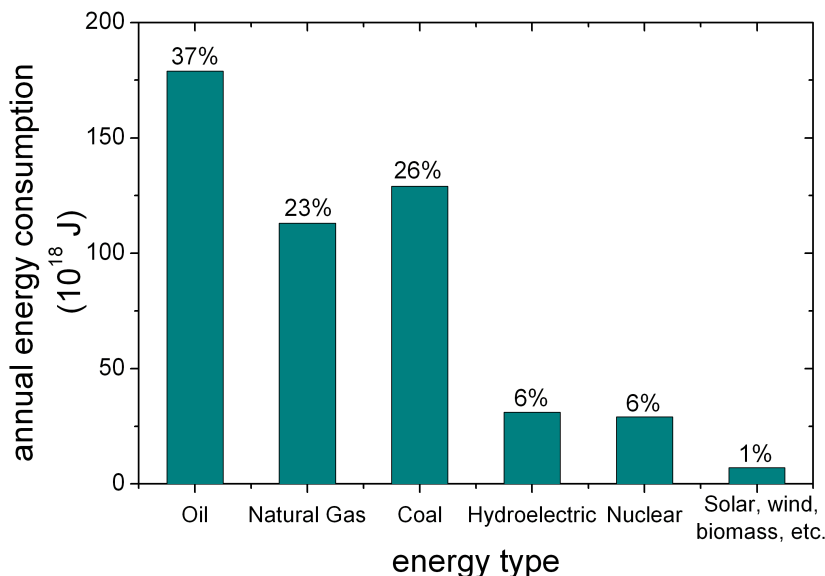


Figure 1.1.: World primary energy consumption of 2005 [3].

Thanks to the rapid progress in prospecting, extraction and refining of hydrocarbons during the twentieth century, oil has become the most important fossil fuel in our days. In contrast, coal's share in the global fuel supply declined in the last decades in spite of huge gains in recovery, productivity and occupational safety. Traditional biomass fuels, mainly wood, although apparently of negligible importance in the global fuel supply, are still a main source of energy in many developing countries [98].

A very strong increase of the global energy demand characterized the last century. This tendency is expected to continue (see figure 1.2). For this reason and due to the announced shortage of fossil fuels and the increasing environmental concern, the substitution of the actual dominant energy systems by sustainable energy sources and by clean energy production technologies is a central challenge of our society.

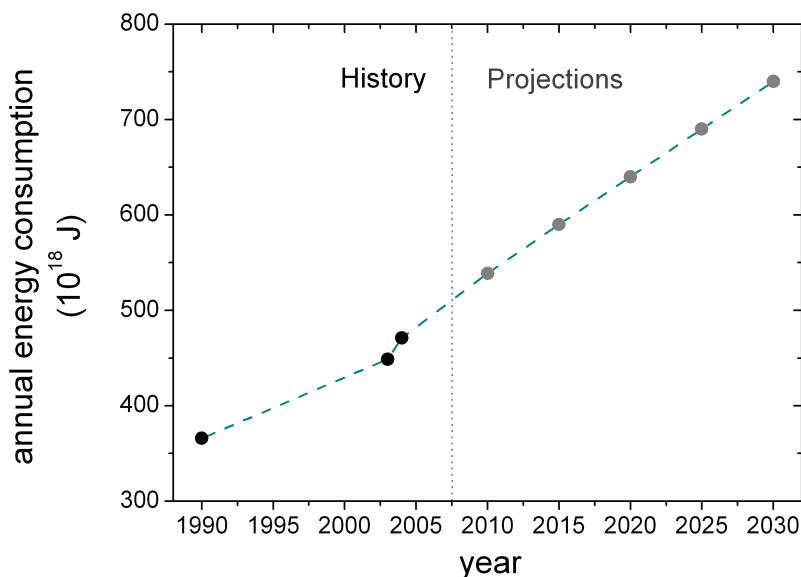


Figure 1.2.: History and projections of the world total primary energy consumption [4].

In the foreseeable future the so-called peak oil will be reached, i.e the maximum attainable global petroleum production. After this point the rate of oil production will enter a terminal decline while oil supply will drop and the prices will rise. The peak oil is expected to be reached around 2012 [5, 64] or even earlier [2, 24].

Before reaching this point, previous to the end of the oil era, an effort is already being done to develop alternative technologies able to cover the energy demand using renewable and sustainable energy sources.

Additionally, public awareness of the environmental consequences of fossil fuel combustion and other technologies, such as nuclear generation of electricity, has grown rapidly in the last years. The necessity of minimizing environmental impacts motivates the development of clean energy production technologies.

In this context and due to the high availability and sustainability of solar energy, its utilization either directly as solar radiation or after its natural conversion to flowing water, wind, waves and biomass will most likely replace fossil fuel combustion. Additionally, electricity is considered to be the energy form of the future [6, 97]. Most of the renewable energy sources primarily produce electricity. This form of energy can be easily distributed and it is characterized by a high efficiency of nearly all final uses, cleanliness and silence at the point of use. A major challenge of this form of energy is, however, its large-scale storage and the need of a fuel with high energy density required for mobile applications. In this context and as summarized by some authors [98, 102], hydrogen (e.g. from electrolysis) may be the most favorable energy carrier in a future non fossil, high-tech civilization, where fuel-cells could represent the most versatile convertors.

Renewable energy technologies are, however, not yet competitive mainly due to their high costs. Consequently, in the following decades the energy demand will be covered by

a variety of primary energy sources, among which fossil and biomass fuels will still play a major role. Therefore the further development of combustion technologies is still a focus and the understanding of the complex processes taking place during combustion remains as a main goal in today's scientific effort.

In this context, the formation and the environmental impact of pollutants such as nitrogen oxides (NO_x), sulfur dioxide (SO_2), carbon dioxide (CO_2), volatile organic compounds (VOC) and soot attracts a great deal of attention.

Combustion of fossil fuels has been the largest source of anthropogenic emissions of SO_2 and NO_x , whose eventual oxidation produces the sulfates and nitrates responsible for regional acid deposition (acid rain). Acid deposition had the greatest impact on ecosystems in Central and Northern Europe, Eastern North America and East Asia. The combination of particulate matter (mainly soot) and SO_2 creates the classic (London-type) smog that was common in Europe and North America until the 1960s.

Gradual replacement of coal by sulfur free hydrocarbons, widespread use of electrostatic precipitators and flue-gas desulfurization of large stationary sources have dramatically lowered soot and SO_2 emissions in most of the affected regions. Thus, the control, or even the elimination, of some of the local and regional effects of combustion related air and water pollution has been achieved.

Unfortunately, other problems have emerged in the last decades:

- Photochemical smog, generated by complex atmospheric reactions of NO_x , CO and VOC that produce ozone, is now a widespread problem seasonally affecting large cities on every continent.
- Emitted CO_2 is the most important anthropogenic greenhouse gas and its rising atmospheric concentrations have already begun to change the global climate.
- Air pollution due to particulate matter emissions is still of the greatest health concern. The role of the very small particles, mainly soot particles from combustion processes in transportation, power generation or household heating systems, is still being investigated.

Airborne particulate matter is a generic term describing a complex mixture of particles suspended in the air. These particles vary in size, composition and origin. In general, several fractions can be distinguished with respect to size. PM_{10} refers to particles smaller than $10\ \mu m$ in aerodynamic diameter while $PM_{2.5}$ (also known as fine particles) is used for particles smaller than $2.5\ \mu m$ in diameter. $PM_{0.1}$, frequently referred to as ultrafine particles or nanoparticles, includes particles in the nanometer range.

The size and composition of airborne particles depends on their origin. It can be distinguished between natural and human sources. Volcanoes, forest fires or sand storms belong to the first group while important human sources of particles are combustion, industrial processes, wear debris from tires, brakes and clutch linings, etc. In this context, combustion processes are considered to be the main source of ultrafine particles in urban areas.

The very small sizes of ultrafine particles impeded their detection and analysis by the instrumentation formerly used to monitor air pollution. The little awareness about their presence and the difficulties associated with epidemiologic and *in vitro* studies have hampered the investigation of their health effects. All this induced a lack of appropriate legal regulations to limit their emission.

The current regulations for particle emissions set particle emission standards based solely on gravimetric measurements, i.e. only total ambient particle mass concentration is taken into account. For example the existing european air quality standard for particulate matter (EU Directive 1999/30/EC) establishes a daily limit of $50 \mu\text{g}/\text{m}^3$ (averaged over 24 hours) and an annual limit of $40 \mu\text{g}/\text{m}^3$ for PM_{10} ¹. The daily limit can be exceeded on up to 35 days a year. Since ultrafine particles, and thus soot and soot precursor particles, are almost negligible in terms of mass compared to other dusts, the former are consequently barely being taken into account. The harmful health effect of airborne particles is, however, directly related to their size.

PM_{10} is usually retained in the bronchi (thoracic particles). $PM_{2.5}$ penetrates deeper in the respiratory system and can even get into the alveolar sacs (respirable particles). The harmful effect of ultrafine particulate matter is expected to be more important than that of larger-sized particles. As summarized by Oberdörster [86], this is directly related to the capacity of ultrafine particles to readily translocate by different mechanisms after being deposited in the different regions of the pulmonary tract. Due to their uptake into the blood circulation system, the lymphatic system or even the nerve system, ultrafine particles can also reach and affect extrapulmonary sites. In addition, since the number concentration of ultrafine particles is generally several orders of magnitude higher than that of larger particles, ultrafine particulate matter offers a much higher total surface area per mass unit. Consequently, these particles are capable of carrying larger concentrations of adsorbed toxic air pollutants.

It has been demonstrated that not only the size and number concentration but also the chemical composition of the particles plays a role in their health impact. For instance, particle emissions from automatic wood-fired private heating systems are similar to diesel engine particle emissions in terms of particle size, particle number and mass concentration [63]. Particle emissions from automatic wood-fired private heating systems are, however, mainly constituted by ash (inorganic compounds such as $CaSO_4$, K_2CO_3 , etc.) while diesel vehicle particle emissions are solely soot (carbonaceous particles). It has been demonstrated that the latter are much more toxic. However, this has also not been considered by the current regulations.

¹In this case PM_{10} exactly refers to the particulate matter which passes through a size-selective inlet with a 50% efficiency cut-off at $10 \mu\text{m}$ aerodynamic diameter

1.2. Motivation and Aim of this Work

In the history of combustion research a great effort has been done to understand the processes leading to soot formation during incomplete combustion of hydrocarbons. The formation of particles from the gas phase and the first stages of the evolution of these nascent particles are, however, still not completely understood.

As shown in figure 1.3, in a sooting hydrocarbon flame fuel is first degraded into small hydrocarbon radicals from which larger hydrocarbons, aromatic rings and finally large polycyclic aromatic hydrocarbons (*PAHs*) are formed. These processes occur in the gas phase, i.e. in the regime of molecule reactions, and are well understood. From this mixture and within milliseconds the so-called particle inception occurs and primary soot particles emerge in the flame. While the processes involved in particle inception are still unclear, the regime of particle growth has been widely investigated by different aerosol measuring techniques, electron microscopy and optical methods. In this regime, surface growth reactions determine the final soot mass concentration while coagulation leads to the well-known chain-like structure of mature soot.

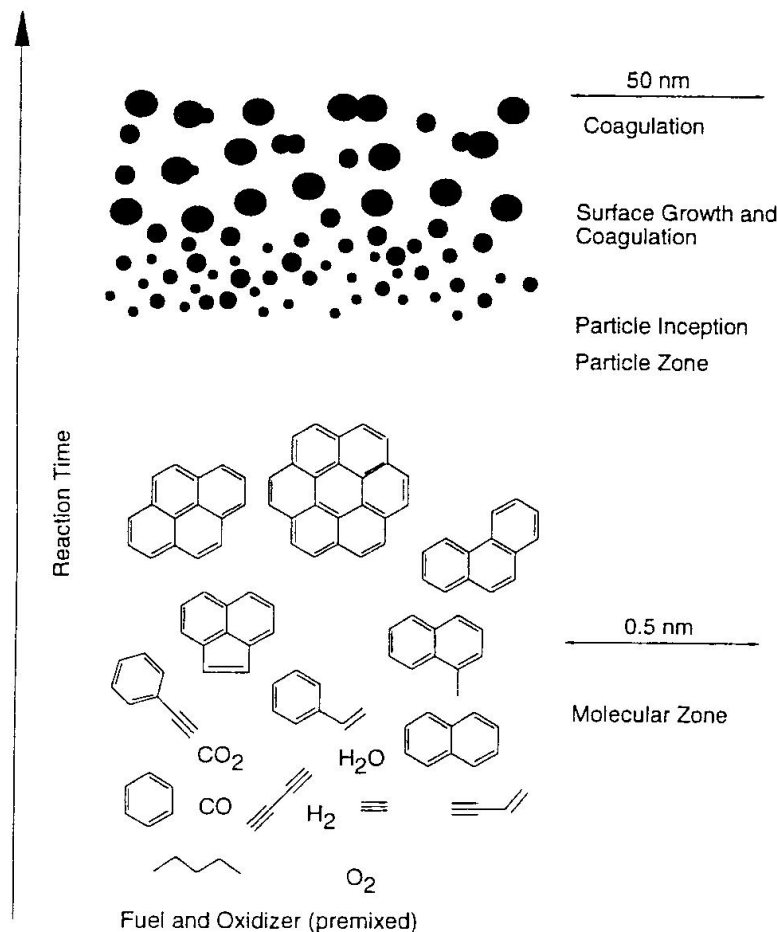


Figure 1.3.: Rough picture for soot formation as published by Bockhorn [16].

As mentioned above, the link between the gas phase regime and the particle growth regime is still missing. The reason for this lack of knowledge is the limited available

experimental information about nascent particles, i.e. about soot precursor particles. Soot precursor particles are characterized by sizes in the range of a few nanometers and by a high reactivity, thus they are still being a challenge for any current measuring technique.

Since the capability to follow the nucleation of particles in flames is necessary to understand the soot formation process, the development of appropriate measuring methods is crucial.

Time of flight mass spectrometry has been broadly applied to the study of incomplete combustion products and combustion kinetics. Both the gas phase and the particle phase (soot and soot precursor particles) have been investigated. To this end several approaches have been considered.

For instance, Dobbins and coworkers [32, 33] combined thermophoretic sampling, laser ablation and mass spectrometry to investigate diffusion flames and, recently, diesel emissions. This method, usually known as laser microprobe mass spectrometry (LMMS), aims at the study of the chemical composition of the soot and soot precursor particles. Unfortunately little information about the original particles (size distribution, structure, etc.) is obtained.

A more direct application of mass spectrometry requires the use of molecular beams as sampling technique. This method allows the transportation of the combustion products into the mass spectrometer and their direct ionization. Due to the difficulties associated with this probing technique, however, most of the previous research has concentrated on the study of low pressure flames.

Some remarkable works based on this technique have been presented by Kohse-Höinghaus et al. [9, 67, 76], who investigated the chemistry of different flames, namely the formation of small hydrocarbons. Homann et al. [54, 65] focused on the study of large gas phase molecules in low pressure flames while Siegmann et al. [52, 96] presented the first measurements of large PAHs in atmospheric flames. Unfortunately, none of these studies report on nascent soot particles. Based on mass spectrometry and molecular beam sampling, Grotheer and coworkers [47, 103] have recently presented results dealing not only with gas phase molecules but also with soot precursor particles in low pressure flames (see chapter 8).

In this context, this thesis studies the range of applicability of mass spectrometry for the detection of soot precursor particles and the investigation of the so-called soot inception. The aim of this work is to gain information about the combustion process through the detection and characterization of soot precursor particles in different combustion systems and in a wide pressure range.

2. Experimental Set-Up

2.1. Time-Of-Flight Mass Spectrometer

2.1.1. Measurement Principle

Ideally in a time-of-flight mass spectrometer (TOF-MS) all ions are formed instantaneously and at a single position. These ions are then accelerated to the same kinetic energy by means of electric fields. After this, the ions enter the field-free drift tube, the mass analyzer of the TOF-MS. Since all ions have the same kinetic energy, ions with different masses will travel along the drift region with different velocities. Consequently lighter ions arrive earlier at the detector than heavier ones. The time of flight along the drift tube is under these conditions proportional to the square root of the mass-to-charge ratio of each ion and given by:

$$t = s \cdot \sqrt{\frac{m_i/z}{2 \cdot U}} \quad (2.1)$$

where t is the time of flight, s the covered distance, m_i the ion mass, z the ion charge and U the acceleration voltage.

Unfortunately, due to many factors, these idealized conditions are not fulfilled in reality. For this reason the resolution, the sensitivity and the resulting detection mass range of a TOF-MS are limited. The resolution is impaired by those effects leading to an energy blurring of the ions, e.g. the spatial width of the region in which ions are generated, the velocity distribution of the ions entering the analyzer, space charge effects or non-uniform electric fields. The sensitivity, on the other hand, is affected by the ionization efficiency, the ion transmission of the system and the detector behavior. Some of these factors, being discussed below, have been successfully studied during the last decades [59, 71]. In particular through the introduction of the reflectron principle [72] a significant progress towards higher resolution could be achieved. Consequently, high resolution and sensitivity are already available in a mass range up to several thousand atomic mass units.

A reflectron TOF-MS (Stefan Kaesdorf GmbH) is used for the present investigations. This device provides a special high acceptance volume, adequate high voltages and a very sensitive detector. This enhances the measuring range to several hundreds of thousand atomic mass units and favors the sensitivity. This "custom-built" unit is adapted in this work to the experimental conditions. To this end, the adjustment and optimization of the sampling system, the laser light source, the TOF-MS itself and the signal processing electronics are necessary.

2.1.2. Arrangement and Function of the Different Electric Fields

A simplified diagram of the apparatus is shown in figure 2.1.

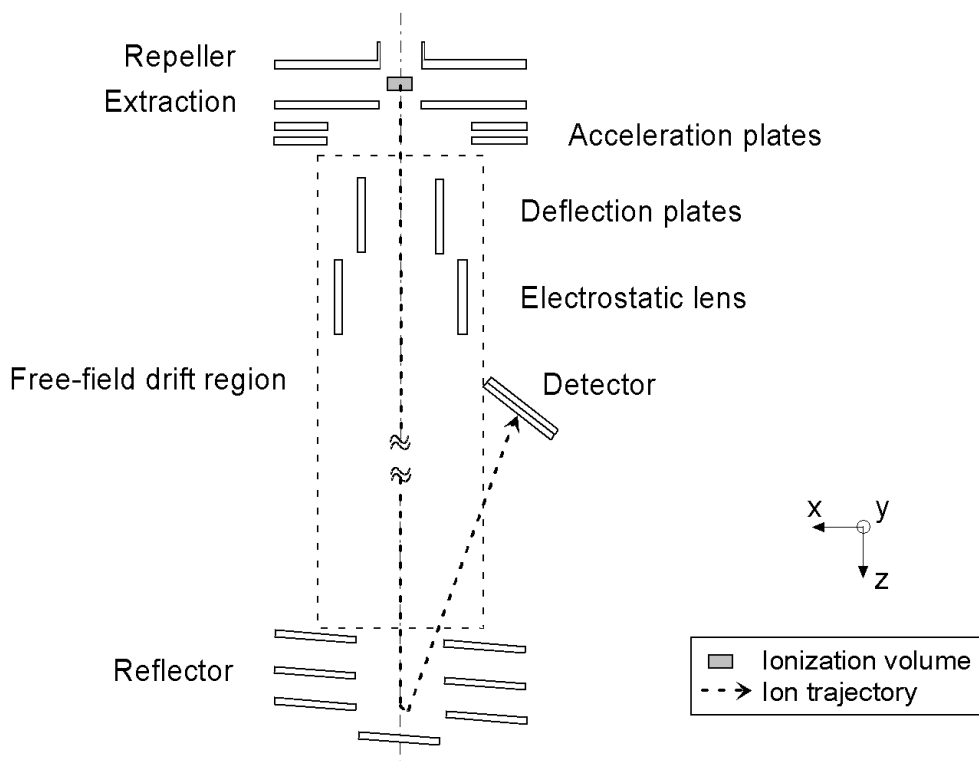


Figure 2.1.: Schematic diagram of the arrangement of the TOF-MS.

The so-called ion source consists of repeller plate, extraction plate and two acceleration plates forming a two-stage extraction. The ions are produced between repeller and extraction plate by means of laser induced photo ionization. The repeller is at a positive high voltage whereas the extraction and the acceleration plates are at negative high voltages. Positive ions, which are the subject of the current study, are forced by this arrangement in the direction of the analyzer.

The laser pulse duration (10 ns) is short in comparison to the typical peak widths (full width at half maximum (FWHM) of approximately 24 ns at 300 u). For this reason no big error is introduced when ions are continuously sampled during the ionization interval. In this case DC voltages supply the repeller, extraction and acceleration plates. In order to achieve a better resolution it is, however, advantageous to use the focusing effect of a time lag between ionization and extraction. This time lag allows ions to move to new positions in the ionization region increasing the resolution as predicted by Wiley and McLaren [112]. In this case a pulsed voltage supplies the repeller and extraction plates. The so-called extraction pulse lasts until all ions have left the ion source. The experimental result of this pulsed extraction is an improvement of the resolution¹ from $\frac{m}{\Delta m} \sim 350$ to 1200 at

¹For a single peak at a mass m the resolution is expressed as $\frac{m}{\Delta m}$, where Δm is the FWHM.

650 u as shown in figure 2.2. It must be noted that this resolution increase is a function of mass [71].

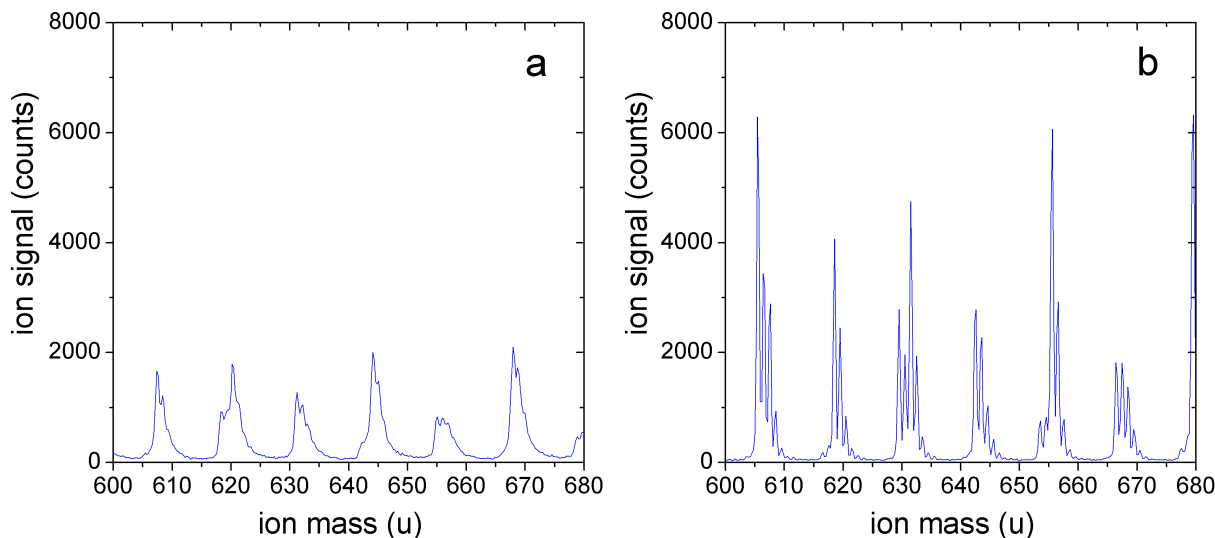


Figure 2.2.: Mass spectra of an ethylene/air flame. a) Continuous extraction. b) Pulsed extraction with time lag focusing. Note: Only narrow portions of the spectra are shown.

Two deflection plates forming a condenser are positioned in the drift tube, so that a deflection of the ion beam in the x - and y - direction is possible. This is necessary especially for cross arrangement of the sampling system (see figure 2.4 on page 29). In such a case the ions leaving the ion source have an impulse in the direction of the molecular beam (x -direction) which has to be compensated for. The voltages of the deflection plates are empirically optimized in order to assure maximal ion transmission. Unfortunately, the gain in ion transmission becomes also mass dependent.

Fragmentation processes subsequent to the ionization or space charge effects due to too high ion densities induce a divergence or energy blurring of the ion beam. These effects can be compensated for by using the electrostatic lens incorporated just after the deflection plates. Once again, a mass dependent focusing effect is introduced.

In a reflectron TOF-MS, the classical mass analyzer of a linear TOF-MS is followed by an electrostatic reflector. This reflector or ion mirror provides, together with the two-stage extraction, the energetic and spatial focusing of the ions. This is needed because, as a result of the spatial width of the region in which ions are generated, ions of the same mass may have different start positions. Since the electrostatic potential between repeller and extraction plates varies linearly, ions formed at different positions will be accelerated to slightly different final kinetic energies [71]. This leads to a spread in ion flight time and consequently causes a decrease in resolution. The different time of flight of ions of same mass but different energy after the acceleration will be leveled at the exit of the reflector. Ions with higher kinetic energy will penetrate deeper in the electric field of the reflector

and cover a longer distance than ions of lower kinetic energy. This energy focusing also helps to reduce the energy blurring due to fragmentation or space charge effects.

After having passed through the whole spectrometer, the ions are detected by a set of two multi-channel plates (Burle Chevron MCP Set, active surface of 40 *mm* diameter). In order to increase the detection efficiency, the incoming ions are subject to a post-acceleration of up to 10 *kV* before reaching the surface of the detector. There, a plume of electrons is emitted upon arrival of an ion and then amplified by cascades in the microchannels. These secondary electrons are then accelerated onto a collector, producing a pulse which is sent to the signal processing electronics.

All operation voltages are roughly adjusted according to some set-up examples of the manufacturer and afterwards empirically optimized.

The whole system works under high vacuum conditions. The pumping system used is described in the next section.

2.2. Sampling Procedure

2.2.1. Sampling and Sample Inlet System

The transportation of the sample from atmospheric conditions to the high vacuum of the ion source chamber of the MS is one of the main difficulties in the application of our method since the original sample composition has to be preserved as completely as possible.

The sampling procedure requires a staged pumping system able to bring the sample to the ionization chamber in the form of a concentrated and well defined molecular beam. In principle this can be done either by a continuous or by a pulsed sample flow. In our case the pulsed sample flow technique is chosen because continuous sampling necessarily involves larger mass flows and hence much larger pumps. Since the TOF-MS and the laser source are also operated in a pulsed mode, synchronization to the pulsed sample beam is required. The maximal repetition rate possible (200 *Hz*) is determined by the laser as well as by the pulse valve.

The pulsed sampling system coupled to the TOF-MS is shown in figure 2.3. The flame or exhaust gases are continuously drawn through the nozzle ($0.6 \leq d_{Nozzle} \leq 1 \text{ mm}$) of a quartz glass probe ($d_i = 6 \text{ mm}$). Downstream of the system a small portion of this flow ($< 0.05\%$ assuming air mass flow under choked conditions) is withdrawn from the main flow. To this end a pulsed T-piece (valve) is used. The pulsed flow is subsequently expanded into a collimator chamber to form a molecular beam. Before entering the high vacuum ionization chamber, the core of this molecular beam is extracted by a skimmer ($d_{Skimmer} \sim 1 \text{ mm}$).

The pulsed T-piece is a modified solenoid valve (Parker, Series 9, $d_{Valve} \sim 1 \text{ mm}$). Lateral bore holes allow the continuous flow above the valve opening with minimal pressure

drop. In order to improve the quality of the seal and the durability of the poppet, the valve seat is machined to a converging nozzle and polished. A small capillary is additionally fixed to the nozzle, as explained in section 2.2.2.

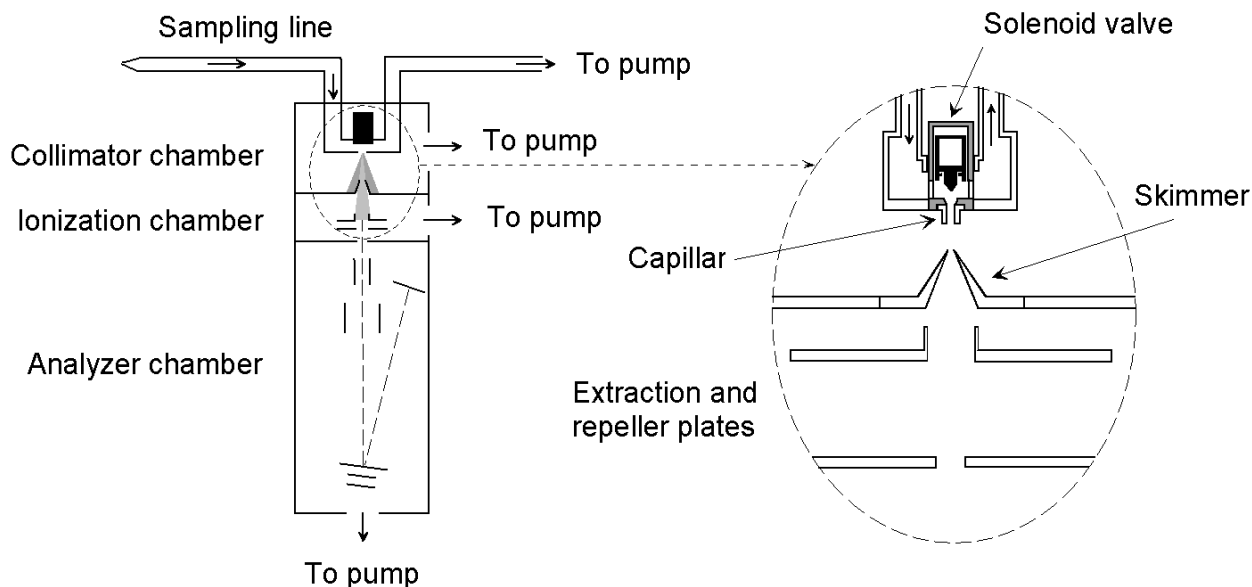


Figure 2.3.: Schematic representation of the pulsed sampling system coupled to the TOF-MS.

The sample is drawn into the probe by a Leybold rotary vane pump (TRIVAC, Model D40B). Both, the collimator and the ionization chamber are evacuated by a pumping set-up consisting of a turbo molecular pump and a backing pump. For the collimator chamber the combination of an Elettrorava turbo molecular pump (Model 160-450) and a Varian dry scroll pump (TriScroll, Model PTS0300) is used. In the case of the ionization chamber a Pfeiffer turbo molecular pump (Model TMH 1001 PC) and a Leybold rotary vane pump (TRIVAC, Model D16B) are employed. The use of turbo pumps ensures that all high vacuum stages are oil-free.

For the pressure measurements two manometers are mounted in the sampling line: one capacitance manometer (MKS Baratron, Type 627B) around 15 *cm* after the tip of the probe and a pressure transducer (MKS Baratron, Type 127A) directly above the nozzle of the pulsed valve. In the case of the collimator and the ionization chamber gauge heads with combined Pirani and cold cathode systems (Pfeiffer Vacuum, Compact Full Range Gauge, PKR 251) are installed.

The pressure in the sampling line at the valve entrance is typically chosen between 12 and 30 *mbar*. During the measurements a pressure below $5 \cdot 10^{-3}$ *mbar* is measured in the collimator chamber. In the ionization chamber the pressure is below $5 \cdot 10^{-6}$ *mbar* during the experiments. It must be taken into account, however, that these pressures are averages. When the sample pulse is on (for about 400 μs) peak pressures are certainly higher than the quoted averages. In addition, the pressure between nozzle and skimmer

is known to be higher than at the measuring location.

The TOF-MS analyzer is evacuated by an Elettrorava turbo molecular pump (Model FTP 8/300). The pressure is measured by another Pfeiffer gauge head (Compact Full Range Gauge, PKR 251) and kept below $5 \cdot 10^{-7}$ mbar during the experiments.

The sampling system described above ensures the necessary operating conditions of the mass spectrometer but demands the investigation of the potential changes of the sample along the sampling line (see section 4).

2.2.2. Molecular Beam Inlet System

Molecular beams are applied in a wide range of experimental studies of physics and chemistry because they provide highly directed systems of molecules and particles which undergo no collisions.

In 1951 Kantrowitz and Grey [61] suggested the replacement of the effusive flow field of conventional oven beams by a supersonic jet. The advantages of supersonic molecular beams, also called nozzle beams, compared to oven beams are mainly:

- The increase of the beam intensity.
- A narrowing of the velocity distributions in the beam due to the decrease in temperature during adiabatic expansion combined with a smaller angle of the beam.
- Cooling of internal degrees of freedom and consequently deceleration or deactivation of reactions.

Supersonic molecular beams are extensively used for molecular detection applications in conjunction with laser mass spectrometry yielding an improvement in sensitivity, selectivity and resolution [71].

In order to achieve the desired high beam intensities the design of nozzle beam system must be optimized. In this context parameters including source pressure, pumping speed and shape, dimensions and position of the defining elements (nozzle and skimmer) are determining. To date, most investigations of nozzle beam development have focused on pure gases and gas mixtures [7, 8, 22, 49]. Research has also been done concerning the characterization of aerosol beams [57, 110, 115]. In these studies parameters like expansion angle, intensity and velocity of the beam have been investigated mostly for aerosols of particles larger than several ten *nm* in diameter. Furthermore elaborate devices for particle focusing have been developed [69, 70]. For particles of just a few *nm* in diameter, which are the subject of the present study, however, these devices suffer from an increased diffusion so that they become much less effective. Consequently, previous studies on molecular beam performance can just be used as reference in experiment design.

Anderson et al. [8] noted that in vacuum systems a simple converging nozzle produces supersonic beams. Additionally, investigations by Campargue [22, 23] indicated that higher beam intensities could be achieved using capillaries with $L \geq 2d_{\text{Nozzle}}$, L being the length

of the capillary and d_{Nozzle} its diameter. Israel and Friedlander [57] studied the generation of beams of particulate matter (latex particles of more than 100 nm). They indicated the advantages of using capillaries for the concentration of aerosol samples. On account of this, first a simple converging nozzle and then a capillary ($L = 5 \text{ mm}$, $d_{Nozzle} = 1 \text{ mm}$) were tested in our system. It was shown that the capillary yields just a slight increase in the beam intensity compared to the simple converging nozzle. Nevertheless since the capillary greatly simplifies the alignment of the nozzle-skimmer system, it is used for the measurements in flames and exhaust gases shown later in this work.

In general, high pressure ratios across the nozzle can yield higher beam intensities because higher Mach numbers are reached. Unfortunately higher pressure ratios across the nozzle can not be applied in our case: An increase of the source pressure (or pressure above the valve) is related with an increase in the residence time of the sample in the sampling line. This increases the reaction time for coagulation, as to be explained in section 4.1. For this reason, in our system the source pressure is always kept as low as possible. On the other hand, the pressure downstream of the nozzle (collimator chamber) is given by the corresponding pumping combination and can not be reduced. Furthermore, the nozzle diameter cannot be made smaller due to mechanical limitations.

Under these conditions the available parameters for the optimization of the beam intensity are essentially the distance between the nozzle and the skimmer (a), the distance between skimmer and the ionization point (b) and the skimmer shape and dimensions.

The optimal distances a and b yielding maximum beam intensities are always linked to the beam structure. In a first region the Mach number increases and the temperature of the beam decreases (isentropic continuum flow). Within a few nozzle diameters, however, the density of the beam usually becomes so low, that a transition to nonisentropic free molecular flow occurs. Downstream of the nozzle the density of the beam decreases inversely with the square of the axial distance. Consequently, too long a distance a or b yields loss in the signal intensities. Too short a distance a , however, hampers the proper expansion of the supersonic beam and also yields a decrease of beam intensity. The distance between nozzle and skimmer (a) and the distance from skimmer to ionization point (b) are empirically optimized. The final configuration is $a = 4 \text{ mm}$ and $b = 30 \text{ mm}$.

The purpose of the skimmer is to extract the particle-enriched core of the beam in order to achieve a better vacuum in the ionization chamber. The expansion of the beam, however, should not be influenced by the skimmer. The latter is machined of hardened aluminum with a cone angle of 50° and a sharp edge aperture of 1 mm diameter. The cone angle is chosen following the recommendations of Anderson et al. [7]. They found that cone angles of 60° or less would ensure the attachment of the shock waves produced by the skimmer at Mach numbers above about 1.5. This allows the efficient supersonic expansion of the beam. Due to limitations of the pumping speed, large skimmer diameters are not applicable.

After some days of operation a well defined, round soot deposit is observable on the

skimmer surface and the extraction plate, which are mounted just below the pulsed nozzle. This confirms the proper alignment and operation of the molecular beam.

2.2.3. Cross and Axial Arrangement

Two different arrangements of the sampling system are possible, as shown in figure 2.4:

- Cross arrangement resulting in a molecular beam orientated at right angles to the axis of the TOF-MS (acceleration direction)
- Axial arrangement resulting in a molecular beam expanding in the direction of the analyzer.

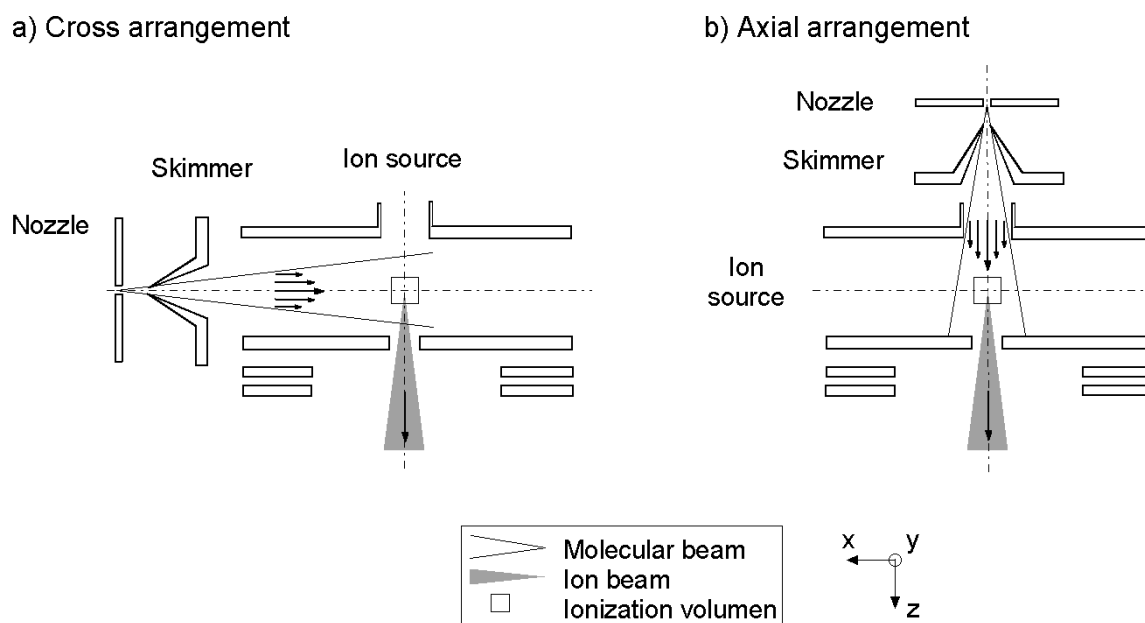


Figure 2.4.: Schematic representation of the two different arrangements of the sampling system. a) Cross arrangement. b) Axial arrangement.

The advantages of the cross arrangement compared to the axial arrangement are the reduced contamination of the analyzer and a gain of resolution, the latter explained as follows:

Particles in the molecular beam are characterized by an initial distribution of velocity components parallel to the direction of the beam as shown in figure 2.4. For axial arrangement, this initial velocity distribution is parallel to the acceleration direction of the ions. Consequently, it contributes directly to the end velocity of the ions after extraction. This leads to an increased spread in ion velocity and provides a reduction of the resolution. For cross arrangement the velocity distribution of the initial neutral particles will not affect the velocity of the ions once accelerated. Therefore it will not affect the resolution of the MS.

A clear disadvantage of the cross arrangement, on the other hand, is the so called cut-corner effect: All ions in the ion source have an impulse in the direction of the molecular

beam. This impulse is proportional to the masses and velocities of the neutral precursors of the ions in the beam. For cross arrangement of the sampling system this impulse is perpendicular to the axis of the TOF-MS. Consequently it has to be overcome by the acceleration voltages so that every ion changes its trajectory and enters the extraction aperture. With increasing ion mass or increasing velocity it becomes more and more difficult to force the ions "around the corner" in order to enter the mass spectrometer. This results in an upper mass detection limit (cutoff) and in a mass dependent sensitivity. Both are determined by the mass and velocity distributions in the molecular beam and by the ion optics of the mass spectrometer.

For cross arrangement high repeller and extraction voltages are applied in order to extend the detection range to larger ion masses. Nevertheless, as shown in the experiment below, there is a clear indication of the cut-corner effect. This effect can be partially compensated for by displacing the ionization volume in the direction of the skimmer. This favors the detection of large ions as a consequence of the increased space available for the 90° turn.

The performance of the molecular beam can be studied with a test consisting in the variation of the pressure at the valve entrance (source pressure for the molecular beam). The results of such a test are shown in figure 2.5 for two different positions of the ionization volume. A McKenna burner under similar conditions as the ones explained in section 3 is used as particle generator. The valve pressure is controlled by throttling the corresponding forepump.

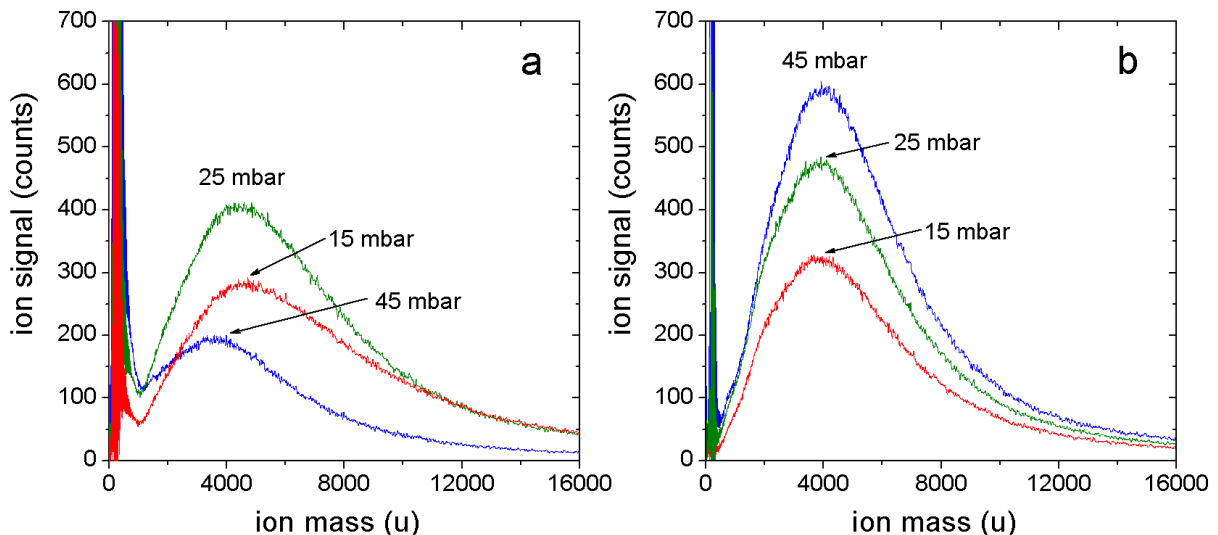


Figure 2.5.: Mass spectra of an ethylene/air flame at different pressures at the valve entrance. a) Ionization volume adjusted to the axis of the ion optics. b) Ionization volume displaced 4 mm in the direction of the molecular beam.

First the ionization volume is adjusted to the axis of the ion optics. For this arrangement, as shown in figure 2.5 a, for lower pressures an increase of the signal intensities is

observed with increasing valve pressure. This is then followed by a strong decay of the signal intensities for pressures above 25 *mbar*. Together with this signal intensity decay, a shift of the mass distribution to lower masses is found.

As the ionization volume is displaced in the direction of the skimmer, it is observed that the evolution of the signal intensities with increasing valve pressure is different (see figure 2.5 b). In the investigated pressure range, the intensities increase roughly proportional to the valve pressure as expected. Additionally no shift of the mass distribution is observed.

The results shown in figure 2.5 a are related with the onset of the cut-corner effect at high valve pressures: Increasing source pressures, directly related with high pressure ratios across the nozzle, yield not only higher beam intensities but also a lower velocity slip² of heavy particles. The latter induces larger impulses of the heavy ions in the direction of the molecular beam and thus shifts the cut-corner effect to lower masses. This explains both the decay of the signal intensities and the altered mass distributions.

This undesired mass dependent detection sensitivity and cutoff is especially unfavorable for large masses and compensated only to some extent by the displacement of the ionization volume. For these reasons the axial alignment is considered favorable and is used for the measurements presented later in this work.

2.3. Laser System

Photo ionization of the sample is provided by an ArF excimer laser (Lambda Physik OpTex) at $\lambda = 193 \text{ nm}$. The laser produced 10 *ns* pulses at repetition rates of up to 200 *Hz*. The nominal pulse energies typically range from 1 to 5 *mJ*. The internal energy measurement of the laser system is frequently calibrated with an external pyroelectric measuring head (Coherent LM-P10i).

The nominal laser beam is characterized by a cross-sectional area of $12 \times 8 \text{ mm}$. The homogeneity of the beam was roughly checked on a test slide (Coherent, black coating test slide). The presence of hot spots could be ruled out and a central section of $5 \times 5 \text{ mm}$ is considered homogeneous. For this reason an aperture ($5 \times 5 \text{ mm}$) is always mounted directly behind the laser beam exit window.

Neutral density filters with optical densities ranging from 0.33 to 0.50 (Edmund Optics) and a cylinder lens (LINOS) are used to vary the laser power density in the ionization region. The cylinder lens is characterized by a nominal focal length of 156 *mm* for $\lambda = 258$. The corresponding focal length at $\lambda = 193 \text{ nm}$, calculated with the software WinLens 4.5 (LINOS), is 139.7 *mm*.

²In a molecular beam of particles, the latter are accelerated within the nozzle by collisions with the fast flowing gas molecules. Assuming rigid sphere collisions, the cross section of a particle increases with the square while its weight increases with the cube of its radius. Consequently, smaller (and lighter) particles are accelerated more quickly and gain a higher velocity than the heavier ones. This decrease in velocity with increasing particle mass is known as velocity slip [115].

The energy of the laser pulses behind the aperture and filters is registered with an external pyroelectric measuring head (Coherent J50LP-4A) under experimental measurement conditions (200 Hz) and used for the calculation of the laser power density.

The laser beam enters the high vacuum ionization chamber through a quartz window (transmission efficiency of 85%). It is adjusted to intersect the desired ionization region between extraction and repeller plates. For axial arrangement of the sampling system the ionization region is displaced 3 mm in the direction of the repeller plate to facilitate the spatial focusing of the mass spectrometer. For cross arrangement the ionization region is displaced another 4 mm in the direction of the molecular beam to compensate for the cut-corner effect.

2.4. Signal Processing

The signal processing is presented schematically in figure 2.6.

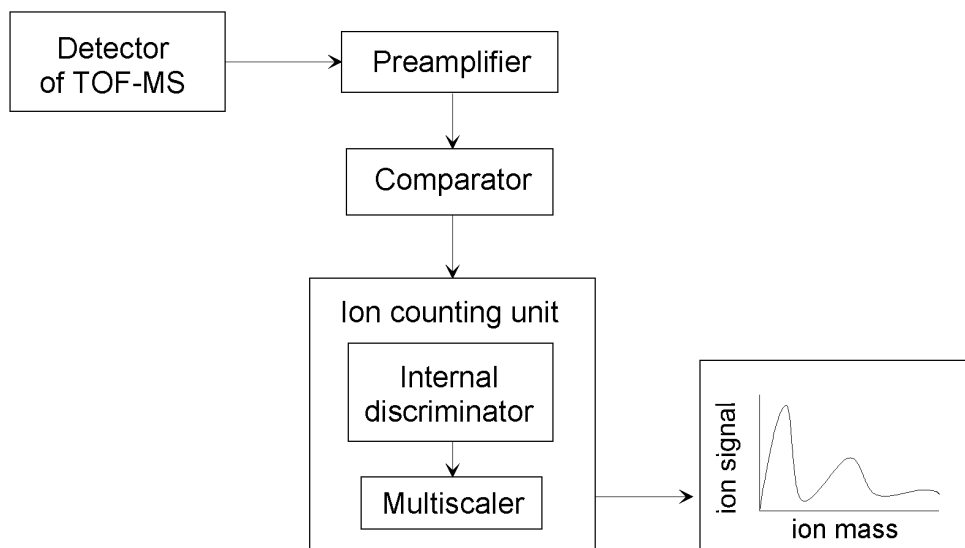


Figure 2.6.: Schematic representation of the signal processing chain.

In order to provide a better signal-to-noise ratio, the method of ion-counting is used. Here the ion signals from the detector are first amplified and then counted as ion signals if they exceed the threshold of a comparator. Both amplifier and comparator are especially designed and adjusted for the dynamic range of the MCP and the different measuring conditions.

Two different amplifiers are available:

- i) A commercial preamplifier (ORTEC, Model VT120) with an amplification factor of 100.
- ii) A "custom-built" amplifier [15] with an amplification factor of just 5, but a higher overdrive threshold and a lower overdrive recovery time than the ORTEC version.

The use of the ORTEC preamplifier is limited due to its low overdrive threshold of just some mV . The latter leads to saturation of the device for ion masses below 1000 u in most tests. To avoid this while applying a high amplification factor for the detection of masses in the range above several tens of thousand atomic units, the low mass portion of the spectrum can be filtered out. To this end one of the deflection plates can be switched to ground potential during the first 0.5 to 1.5 μs of the ion extraction. By so doing the lightest ions, always present in high amounts, do not reach the detector and thus do not produce any malfunction of the amplifier.

The main component of the "custom-built" amplifier is a Texas Instruments operational amplifier (THS3201 with 5200 $V/\mu s$ at $\pm 5 V$ supply voltage). This amplifier is installed in those cases when no extreme sensitivity is required (e.g. at high fuel equivalence ratios) and/or when the recording of the low mass range of the spectra is desired.

The comparator, also "custom-built" [15], consists of a monolithic integrated circuit (Analog Devices, ADCMP580). It provides an adjustable lower threshold and consequently allows filtering of most of the system noise. A so-called clamp diode protects the input of the comparator from too high voltage peaks. This also ensures the protection of the expensive ion counting unit.

As an ion counting unit a multiple event time digitizer (FAST Multiscaler Model 7886, ComJec GmbH) is used. Such systems are specially adequate for the detection of signals with small signal-to-noise ratios. Contrary to the traditionally used analog devices such as oscilloscopes, no information about the height of the signal is recorded. This represents an advantage since the amplitudes of the detector output signals decrease drastically with increasing ion masses (see section 8.3). The FAST Multiscaler has a minimal time resolution of 500 ps and can handle peak count rates of up to 2 GHz . The acquisition time arises from the selected number of time bins and the bin resolution (bin width), which is adapted to the measurement conditions. The dynamic range of the FAST Multiscaler enables the acquisition of a complete mass spectrum with every sweep.

In order to get representative spectra, every single measurement requires the acquisition and addition of several thousand sweeps. The recorded data are then automatically shown in the form of ion counts vs. time of flight spectra.

The time of flight of the ions between the point of ionization and the detector is proportional to the square root of the mass-to-charge ratio. As explained in chapter 5 no evidence of multiple charged ions is found, thus a unique dependency between time of flight and ion mass is assumed. The time of flight of ions of different masses is then determined by the physical parameters of the TOF-MS. This includes strength of the electrical fields, distances between plates and length of the drift tube. Due to the complexity of these dependencies, the corresponding mass values are experimentally fitted using frequent mass calibrations. To this end calibration substances such as benzene (78 u), toluene (92 u), naphthalene (128 u) or diiodobenzene (330 u), are injected into the TOF-MS either via the sampling system or using direct injection of solutions. Moreover, flame measurements

under fragmenting conditions are carried out, whereby ions like atomic oxygen (16 u) or atomic nitrogen (14 u) together with a typical fullerene distribution (e.g. Buckminster fullerene) can be identified. These species are used as reference to convert the recorded time of flight data into mass values using a polynomial fit of third order.

2.5. Synchronization

The data acquisition system is controlled using a software (Kaesdorf, TOF 4.5) provided by the manufacturer of the mass spectrometer. This software allows the setting of the ion count unit (bin width, range and sweeps) and its triggering by means of a pulse generator (Bergmann, Model BME-G03). In addition, it also triggers the laser system and the high voltage switch of the extraction and the deflection plates. Depending on the experimental conditions, pulse duration and delays can be varied. The solenoid valve of the sampling system is controlled by an extra pulse generator (Parker, IOTA ONE). For synchronization of both systems another pulse generator is used (Standford, model DG535). The whole system was operated at 200 Hz .

First of all, the solenoid valve is triggered. Subsequently the laser system is triggered with a delay of 700 μs corresponding to the response time of the valve and the flight time of the molecular beam up to the ionization region. Afterwards both high voltage switches are triggered to allow ion extraction. The extraction is delayed up to 0.5 μs relative to the ionization laser. In a conventional TOF-MS a typical time for the ion extraction pulse is 1 μs . In our case it has to be increased to 10 μs to make extraction of heavy ions possible. The deflection plates are activated 0.5 to 1.5 μs after the extraction.

3. Burners and Measuring Procedure

For the study of particle formation as a function of flame stoichiometry (fuel equivalence ratio, Φ) and height above the burner (HAB) under atmospheric pressure conditions a so-called McKenna burner ("Burner I") is used. This is a water-cooled sintered stainless steel porous plug burner. It consists of an inner cylindrical chamber (60 mm in diameter) and an outer concentric annulus for shroud gas. The burner is operated with a fixed total unburned gas flow of 10 L/min in a wide range of equivalence ratios of ethylene/air mixtures. Typical cold gas flow velocities are approximately 6 cm/s. The unburned gas flows are controlled by Bronkhorst mass flow controllers. These flow controllers are regularly calibrated and are characterized by an accuracy of $\pm 1-2\%$ of full scale. The upper part of the resulting laminar premixed flames is additionally stabilized by a steel plate (thickness of 20 mm and diameter of 60 mm) positioned at $HAB = 21$ mm.

"Burner II" is also an atmospheric McKenna burner operated with a fixed total unburned gas flow of 10 L/min. In this case the porous plug is made of bronze (60 mm in diameter) and the burner assembly is slightly different. The unburned gas flows are controlled by Tylan mass flow controllers (accuracy $\pm 1\%$ of full scale) also regularly calibrated. "Burner II" is used to study effects in the sampling line and for the measurements of particles outside of the flame. In this latter case the stabilization steel plate is dismantled and the flame is shielded from the surrounding atmosphere by means of a 70 L/min shroud of nitrogen. Alternatively, the nitrogen can be replaced by compressed air.

The burners described above are mounted on a movable support which is adjustable in the three orthogonal directions (± 0.5 mm). This allows the rapid and reproducible positioning of the burner. Before each series of measurements the desired flames are allowed to burn at least five minutes to assure steady operation conditions of the burners. Afterwards, and for each single measurement, the burner is positioned and after approximately 1 minute the measurement is carried out. Once the measurement is finished, the burner is separated from the probe. This avoids the clogging of the nozzle, especially at high equivalence ratios, and also an undesired increase of the sampling line temperature (see section 4.2 for temperature effects).

The measurements under low pressure conditions require a different water-cooled sintered bronze porous plug burner (30 mm in diameter) mounted in a suitable housing. Ethylene/oxygen mixtures can be burned in a wide range of equivalence ratios with a fixed total unburned gas flow of 1.25 L/min. Typical cold gas flow velocities are approximately 20 cm/s. The unburned gas flows are controlled by Tylan mass flow controllers.

These flow controllers are regularly calibrated (accuracy of $\pm 1\%$ of full scale). The resulting laminar premixed flame burns head-down. The pressure in the combustion chamber is controlled by throttling a Leybold rotary vane pump (TRIVAC, type S16B). The burner is operated at 160 or 120 *mbar*.

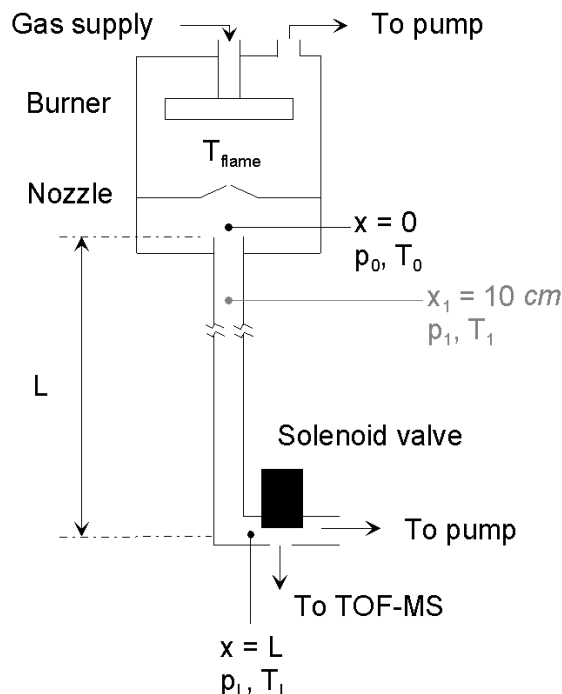


Figure 3.1.: Schematic representation of the low pressure burner coupled to the TOF-MS.

The housing of the burner is equipped with a ceramic nozzle (diameter = 1 *mm*) at its bottom plate. The distance between the ceramic nozzle and the matrix of the burner (*HAB*) can be varied between 17 and 37 *mm*. This ceramic nozzle acts in a similar way as the quartz glass probe described in chapter 2.2.1. However, its large dimensions relative to the actual low pressure burner lead to more pronounced flame distortions. Therefore no *HAB*-profiles of the flame are studied and the nozzle remains fixed at 37 *mm*.

The whole assembly can be coupled to the pulsed sampling system of the MS by means of a steel tube ($d_i = 6 \text{ mm}$) as shown in figure 3.1. The length of this tube is variable (shortest length = 25 *cm*). This allows the study of particle losses and coagulation effects in the sampling line. In order to obtain molecular beam conditions comparable to those of the atmospheric flame measurements, the pressure in the sampling line at the pulsed valve entrance to the MS is set to values between 12 and 30 *mbar*. This low pressure burner can also be coupled to the cold trap system described in appendix A and be used as particle source for the preparation of wet samples for calibration and for toxicological analysis.

Despite of an external water cooling circuit, there is a continuous temperature increase of the vacuum housing. This allows maximum operation times of only 45 minutes to assure

the stability of the O-ring seals. The relatively rapid clogging of the ceramic nozzle at high equivalence ratios requires frequent cleaning of the nozzle by burning lean flames.

4. Sampling Line Effects

Like other techniques used for the detection and characterization of particles in flames such as SMPS or TEM, mass spectrometry is an intrusive method. Consequently it requires a probe and a sampling line. This involves several difficulties:

i) The investigated combustion systems may be perturbed by the introduction of the sampling probe. A flame, for instance, is slightly cooled and a disturbance of the flow field is inevitable. In addition, a quenching of active species may occur.

ii) When dealing with aerosols (particles suspended in a gas), sampling under isokinetic conditions¹ is generally required to obtain a representative particle sample, i.e. a sample with a particle size distribution and concentration equal to the one of the original aerosol. In our case, due to the small size of the particles on study ($\ll 1 \mu m$) and their negligible inertia, no significant error is expected when sampling under non-isokinetic conditions [51, 53].

iii) The extracted sample may undergo undesired reactions in the sampling line resulting in changed compositions or mass distributions. In our case the potential influence of catalytic reactions in the sampling line at high sampling temperatures (e.g. flames) is reduced by the use of quartz glass probes. The expansion of the sample through the nozzle of the probe and its corresponding cooling provides the "freezing" of the kinetic reactions taking place in the flame. Other important processes affecting the aerosol in the sampling line are for instance coagulation, condensation of gaseous compounds and particle losses to the walls. These effects are studied in the following sections.

4.1. Coagulation

The composition of an aerosol can be affected by the recombination of the particles suspended in the gas during their transport along a sampling line. Two different processes can be distinguished: Coagulation and aggregation.

The coagulation is the process by which two particles collide and (like liquids) coalesce to form one larger particle. The result is a continuous decrease in particle number concentration coupled with an increase in particle size and reduction in the total surface area. Aggregation is the process where particles collide and adhere to form aggregates. Particles do not coalesce in this case, i.e. the original particles maintain their original shape and are still distinguishable in the aggregate [39].

¹Sampling is isokinetic when the inlet axis of the probe is aligned parallel to the gas streamlines and the gas velocity entering the probe equals the free-stream velocity approaching the inlet [53].

In combustion the term aggregation is usually reserved for soot particles while coagulation is used when talking about soot precursor particles [33]. As the latter are the subject of this study, coagulation will be considered.

The description of the coagulation process, particularly for polydisperse aerosols which are the subject of the present work, is fairly complicated. For this reason, very simplified theories are quite often applied.

After Smoluchowski [53] the rate of change of the number concentration of an aerosol (dN/dt), assuming a mono dispersed particle distribution and spherical particles, can be expressed as:

$$dN/dt = -KN^2 \quad (4.1)$$

where K is the coagulation coefficient and N the number concentration of particles.

Generally it is assumed that particles adhere with every collision and thus the coagulation coefficient can be expressed as a function of the diffusion coefficient, D , as

$$dN/dt = -4\pi d_p D N^2 \quad \text{for } d_p > 0.1 \mu m \quad (4.2)$$

where d_p is the particle diameter.

Alternatively, the coagulation coefficient can be expressed as a function of the slip correction factor (C_c) as

$$dN/dt = -\frac{4kTC_c}{3\eta} N^2 \quad \text{for } d_p > 0.1 \mu m \quad (4.3)$$

where k is the Boltzmann's constant, T the temperature and η the viscosity.

To apply these expressions to smaller particles ($d_p < 0.1 \mu m$) a correction factor β has to be used [40]. A typical value of β is 0.037 for 4 nm particles in air at standard conditions.

According to equation 4.1, to minimize the coagulation of an aerosol sample prior to its measurement both the concentration and the residence time of the sample in the sampling line must be reduced.

The dilution of the aerosol with inert gas is a widely used method in order to reduce the concentration of the sample. For instance, in the case of SMPS, several authors [73, 114] have demonstrated that particle coagulation can be controlled by systematic variation of the dilution ratio of the sample. The dilution ratio is increased to a critical value above which the particle size distributions become independent of the dilution ratio of the sample. An indispensable requirement of the method is the dilution of the sample as close as possible to the sampling location.

For mass spectrometry, due to its limited sensitivity, the direct dilution of the sample is not recommendable. As an alternative and considering that in any case a large reduction

of the sample pressure is needed, the pressure drop (expansion) across the nozzle of the probe is used to reduce the concentration of the sample in the sampling line.

In order to reduce the residence time of the sample in the sampling line the geometry of the tubing system must be carefully chosen.

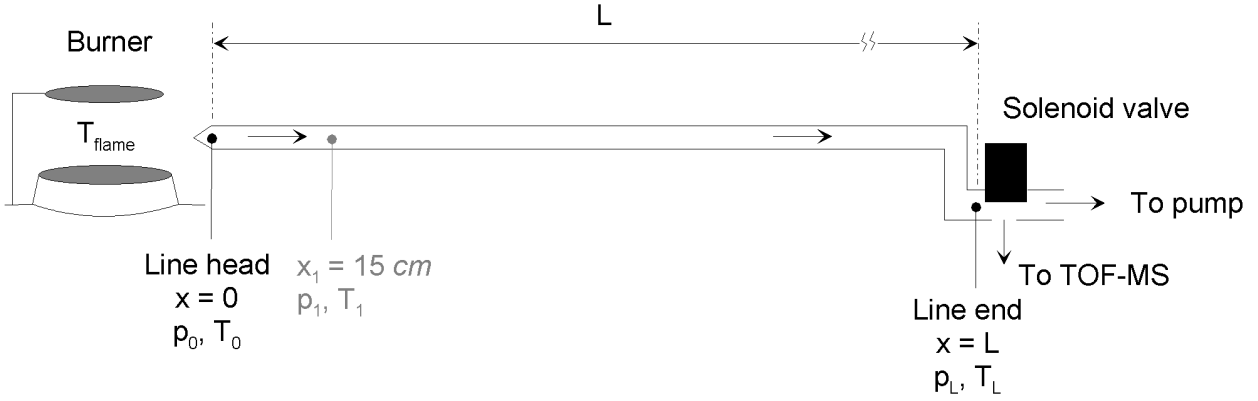


Figure 4.1.: Schematic representation of the sampling line.

For laminar flow and assuming a constant average temperature along the line (\bar{T}), the residence time (t) through a cylindrical tube of radius r and length L is given by:

$$t = \int_0^L \frac{\pi r^2}{R\bar{T}\dot{n}} p_x dx \quad (4.4)$$

where R is the gas constant, \dot{n} the molar flow rate, p the pressure and x the length of the line. The line head is represented by $x = 0$ and the line end by $x = L$, as shown in figure 4.1.

Under the assumption that the temperature in the sampling line can be averaged by \bar{T} , the pressure as a function of the line length can be calculated as follows [107]:

$$p_x = \sqrt{\frac{16\dot{n}R\bar{T}\eta L}{\pi r^4} + p_L^2} \quad (4.5)$$

where η is the dynamic viscosity.

Substituting equation 4.5 for the pressure along the line in equation 4.4 one obtains

$$t = \int_0^L \frac{\pi r^2}{R\bar{T}\dot{n}} \sqrt{\frac{16\dot{n}R\bar{T}\eta L}{\pi r^4} + p_L^2} dx \quad (4.6)$$

And after integration

$$t = \frac{1}{24\pi\eta (R\bar{T}\dot{n})^2} \left[(16\pi\dot{n}R\bar{T}\eta L + \pi^2 r^4 p_L^2)^{3/2} - (\pi^2 r^4 p_L^2)^{3/2} \right] \quad (4.7)$$

Simplifying with equation 4.5 applied at $x = 0$ one obtains

$$t = \frac{1}{24} \left(\frac{\pi r^3}{\dot{n} R \bar{T}} \right)^2 (p_0^3 - p_L^3) \quad (4.8)$$

From this set of expressions it is clear that, for a fixed p_L , large values of the radius r result in an increase of the residence time of the sample in the sampling line due to an increased tubing cross section. On the other hand, small-sized tubing increases viscous effects, resulting in a larger pressure drop along the line ($\Delta p = p_0 - p_L$). This in turn affects the dilution of the sample at the tip of the probe: The expansion ratio decreases and results in an increased coagulation. A compromise between both effects had to be found.

As an example the residence time (t), the pressure at the tip of the probe (p_0) and the resulting expansion ratio ($E = \frac{p_{Flame}}{p_0} \cdot \frac{T_0}{T_{Flame}}$) are calculated for different diameters of the sampling line. The results are presented in figure 4.2. For simplification a flow of pure air along the sampling line is assumed. The molar flow rate (\dot{n}) through the nozzle of the probe can be calculated assuming choked flow (Mach = 1) since the pressure difference across the nozzle of the probe is definitely large enough ($p_{Flame} \gg 2p_0$) [68]. This leads to a maximal mass flow rate. In this case, assuming an ideal compressible gas, the mass flow rate is given by [88]:

$$\dot{m} = \left(\frac{2}{\gamma + 1} \right)^{\frac{1}{\gamma - 1}} S_{Nozzle} \sqrt{\frac{2\gamma}{\gamma + 1} \cdot p_{Flame} \cdot \rho_{Flame}} \quad (4.9)$$

where γ is the specific heat ratio, S_{Nozzle} the flow area through the nozzle and ρ the density. And considering $\rho = \frac{p}{R \cdot T}$:

$$\dot{m} = \frac{S_{Nozzle} \cdot p_{Flame}}{\sqrt{T_{Flame}}} \sqrt{\frac{\gamma}{R}} \left(\frac{\gamma + 1}{2} \right)^{-\frac{\gamma + 1}{2(\gamma - 1)}} \quad (4.10)$$

The flame temperature is assumed to be $T_{Flame} = 1900 \text{ K}$, i.e. adiabatic flame temperature of an ethylene/air flame at $\Phi = 2.00$ calculated using [81]. For a first iteration of the calculations the cooling of the sample due to the expansion through the nozzle of the probe is neglected and $T_0 = T_{Flame}$ is assumed. For subsequent iterations, however, the expansion of the sample is considered to be adiabatic and consequently $pV^\gamma = \text{constant}$ [42]. Using the ideal gas law the temperature at the tip of the probe is given by:

$$T_0 = T_{Flame} \left(\frac{P_{Flame}}{P_0} \right)^{\frac{1 - \gamma}{\gamma}} \quad (4.11)$$

The gases are supposed to cool down to room temperature along the sampling line so that $T_L = 25^\circ\text{C}$. For the calculations the resulting average temperature ($\bar{T} = \frac{T_0 + T_L}{2}$) is used. As pressure at the end of the sampling line a typical value of 15 mbar is considered.

The length of the line is set to 1 m and the diameter of the nozzle to 0.8 mm, also typical values.

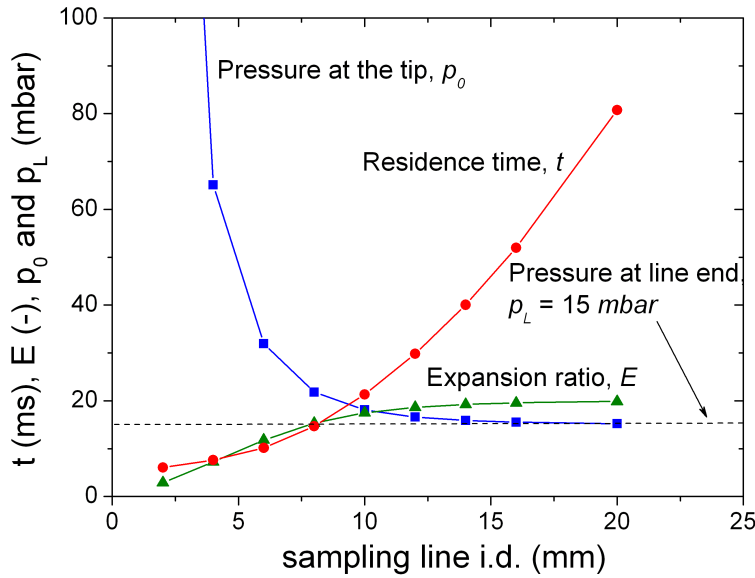


Figure 4.2.: Residence time (t), pressure at the tip of the probe (p_0) and resulting expansion ratio ($E = \frac{p_{Flame}}{p_0} \cdot \frac{T_0}{T_{Flame}}$) calculated for different inner diameters of the sampling line.

In figure 4.2 it is possible to distinguish three different ranges:

For $d_i < 5$ mm, p_0 shows very high values since the viscous pressure drop dominates. This suggests to avoid too small probe inner diameters where the high flow resistance prevents high expansion ratios. Since the initial concentration is the dominating factor in equation 4.3, the high initial concentrations favor coagulation even if the residence time is small. Capillary probes, as used by Hepp [52], represent an extreme case in this regard.

For $d_i > 10$ mm, E reaches a maximal value and stabilizes while t keeps increasing with increasing sampling line inner diameter. This results in increased coagulation. Additionally, higher particle losses are expected with larger diameters due to reduced flow velocities and correspondingly increased wall losses [53].

For diameters ranging between 5 mm and 10 mm optimal conditions for a reduced coagulation are expected.

Using this numerical example as a reference, a tubing of 6 mm inner diameter is chosen to carry out the measurements presented later in this work. The pressure at the tip of the probe is typically approximately 30 mbar ($d_{Nozzle} = 0.8$ mm, $L \sim 1$ m, $P_L = 15$ mbar)(see figure 4.1). Consequently, for atmospheric sample conditions all concentrations are immediately reduced at the sampling location by a factor of approximately $8 \cdot 10^{-2}$ corresponding to an expansion ratio of 12. A residence time of the sample in the sampling line close to 10 ms is expected.

4.2. Temperature Effects

A frequent difficulty when characterizing hot combustion aerosols by means of intrusive techniques is the change of the original sample due to its cooling. The latter may lead to the condensation of low volatile components, mainly large PAHs with low vapor pressure, in the sampling line. In order to avoid this a standard procedure is the heating of the sampling line. This should prevent the formation of droplets of low volatile components and the adsorption of these components on the surface of existing particles or at the walls. Usually, temperatures around 300°C are considered as sufficient to avoid such effects at atmospheric pressure [18].

In our case, the adiabatic expansion and corresponding cooling of the sample through the nozzle of the sampling line could lead in the worst case to a supersaturation of the aerosol. This could then result in droplet formation. These droplets would be a measuring artifact as they are not formed directly by combustion in the flame but by nucleation in the sampling line. This is a well-known effect as explained by Kittelson [62] who found nanoparticles ($d_p < 50 \text{ nm}$) formed by nucleation during dilution and cooling of engine exhaust. Some theoretical considerations based on the Kelvin effect [39, 53], however, suggest that the formation of nano-sized droplets is improbable in our set-up:

The saturation vapor pressure is defined as the equilibrium partial pressure above a given plain liquid surface at a given temperature. In case of small droplets the partial pressure required to maintain mass equilibrium is larger than for a flat surface and consequently exceeds the saturation vapor pressure. For pure liquids, the Kelvin relation describes this effect and predicts that the necessary vapor pressure or saturation ratio for equilibrium increases as particle sizes decrease. Consequently the required saturation ratio to get stable nano-sized droplets of diameters under 10 nm would be so large that its occurrence can be neglected.

In addition, considering the low pressure of just some $m\text{bar}$ governing in the sampling line, temperatures clearly below 300°C (see above and [18]) should be high enough to avoid condensation.

In order to experimentally verify that the measured particle mass distributions associated with particles of diameters from 1 to 6 nm do not arise from coagulation of gaseous compounds in the sampling line the influence of temperature is studied. To this end a thermostated sampling line is used. The temperature of the sample entering the MS is measured using a thermocouple placed just upstream of the solenoid valve. This temperature is varied between 29 and 200°C . No higher temperatures are checked due to the temperature limitation of the solenoid valve at the end of the sampling line. A premixed ethylene/air flame at $\Phi = 1.98$ (Burner II) is used as particle source. The quartz probe is positioned at $HAB = 12 \text{ mm}$ and at the border of the burner surface. The resulting particle mass distributions are shown in figure 4.3.

Figure 4.3 shows a strong signal drop in signal intensity for increasing temperature

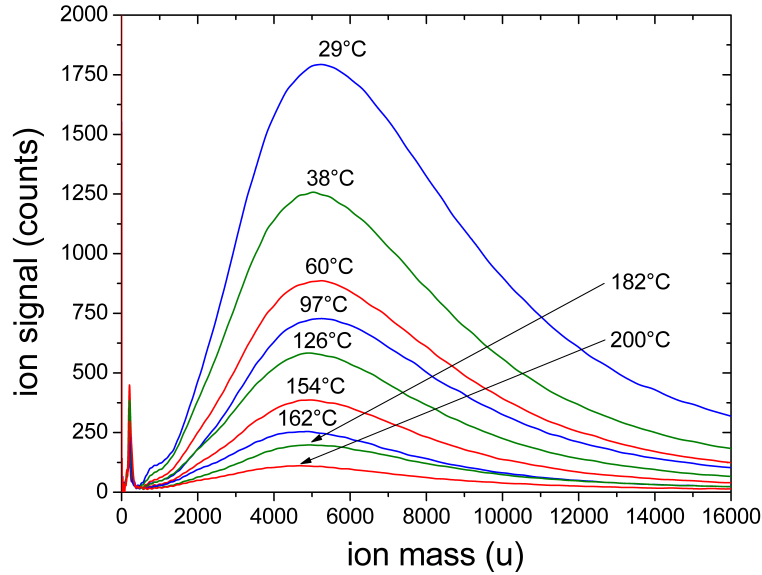


Figure 4.3.: Particle mass distributions as a function of sample temperature. Source is an ethylene/air flame ($\Phi = 1.98$, Burner II) at atmospheric pressure. The original spectra are smoothed for clarity.

of the sample. This signal drop is, however, not accompanied by a change in the mass distribution function: Within the whole investigated temperature range particle mass distributions peaking at approximately $5000 u$ are found. This demonstrates that these spectra do not originate from nano-sized droplets: If the spectrum registered at $29^\circ C$ results from the onset of condensation in form of droplets, these droplets, as explained above, would not be stable at $200^\circ C$ and the corresponding particle mass distributions would disappear. Nevertheless, this is not the case and even at $200^\circ C$ a broad particle mass distribution peaking at approximately $5000 u$ is found.

These mass distributions show almost identical particle mass mean values. Just a little deviation of less than $1000 u$ can be discerned when comparing the extreme cases of the series: $T = 29^\circ C$ peaking out at approximately $5200 u$ and $T = 200^\circ C$ at $4600 u$, respectively. This is probably due to the adsorption of gaseous compounds on the surface of the existing particles at low temperatures. At higher temperatures, these compounds will remain in the gas phase resulting in mass distributions peaking at slightly smaller masses. This effect, as explained below, could also be the reason for the strong reduction of signal intensities that are observed with increasing temperature of the sample.

Several factors may contribute to the observed decrease in signal intensity with increasing temperature:

i) Due to the temperature increase, a decrease in the aerosol concentration of the sample results. Consequently slightly lower signal intensities are expected. As an example, the temperature difference between the extreme cases represented in figure 4.3 implicates a concentration ratio of approximately factor 1.6:

$$\frac{C_{T=29^\circ C}}{C_{T=200^\circ C}} = \frac{473 K}{302 K} \sim 1.6 \quad (4.12)$$

where C is the aerosol concentration and T its temperature.

ii) In addition, the mass flow rate through the valve into the MS is also reduced at increasing temperature. Thus another decrease in the signal intensities is expected. Again, as example, the temperature difference between the "coldest" and the "warmest" cases implicates a mass flow rate difference of factor ~ 1.3 . This can be estimated assuming choked flow through the valve and thus applying eq. 4.10:

$$\frac{\dot{m}_{T=29^{\circ}C}}{\dot{m}_{T=200^{\circ}C}} = \frac{\sqrt{473 K}}{\sqrt{302 K}} \sim 1.3 \quad (4.13)$$

where \dot{m} is the aerosol mass flow rate through the valve.

Obviously these effects can only partly account for the observed temperature dependence as the signal intensity at $T = 29^{\circ}C$ is at least a factor of 15 higher than at $T = 200^{\circ}C$.

A possible explanation may be found in the work of Burtscher and Niessner [20, 21, 83, 84, 85] who proposed the use of photoelectric aerosol sensors for the monitoring of soot and PAH-emissions. In this context they studied the photo-electric charging efficiency of PAH-coated carbon particles. To this end they combined elaborated coating sections and diffusion batteries to produce different PAH surface loads on mono disperse particle distributions. Particles were then exposed to UV radiation, positively charged and finally counted by an aerosol electrometer. From these studies Burtscher and Niessner concluded that even partial layers of PAHs drastically enhance the photo-electric yield of carbon particles.

Extending this conclusion to the current experimental set-up and considering that PAHs are formed during combustion, especially under rich conditions, it is possible that the photo ionization efficiency of the detected particles also depends on their PAH surface loads. In the case of low sample temperatures, the adsorption of PAHs on the surface of the existing particles could favor their ionization and consequently their detection. This enhancement of the ionization efficiency could be explained on the basis of a photoemission process (explained in detail by Burtscher et. al [19]) enhanced by the adsorption of photoemitting material (PAHs).

In order to investigate this effect, a simple coating section added to the sampling line is used. The PAH vapor necessary for coating the aerosol is produced in a heatable container. This container is attached to the sampling line just before the cooled section, where the adsorption of the PAHs onto the particles presumably takes place. The PAH container can be heated up to $300^{\circ}C$, which provides different degrees of PAH saturation in the sampling line. Perylene is chosen as covering material [20].

Under these experimental conditions, particle mass distributions are measured by means of TOF-MS in the already described premixed ethylene/air flames at atmospheric pressure. Due to the limited equipment it is not possible to verify the extend of surface coverage of particles as carried out in the cited experiments [20, 83, 84, 85]. The obtained

spectra, however, do not show any remarkable mass growth or increase in particle diameter so that just sub- to monolayer coverage is expected. Unfortunately, from this set of measurements no increase of the photo ionization efficiency can be asserted and thus no improvement of the sensibility is obtained.

Two possible explanations can be found:

- a) Considering that PAHs are already bound to the particle surface at least in sub-monolayer extent in cooled combustion aerosols, an additional coverage may not substantially increase the photoelectric yield of carbon particles. This is the case of multi-layered coverage as shown by Niessner [83].
- b) The temperature dependent photo ionization may not be related to the PAH enhanced photoemission described by Burtscher and Niessner, since the latter was demonstrated for rather large soot particles which may not be comparable to the soot precursor particles under investigation.

Considering this last possibility, another process can be taken into account, namely a laser-induced chemical ionization, to explain the higher ionization efficiency yields at low temperatures.

Assuming that PAHs are already bound to the particle surface in the combustion generated aerosol, the interaction with the laser beam could lead to the desorption/ionization of these aromatic species. Once formed, these ions could interact with the bulk material of the sample which would lead to its ionization by protonation or charge exchange. At low sample temperatures the extent of PAH adsorption onto the surface of the existing particles increases and thus the enhanced sensibility could be explained by laser-induced chemical ionization.

To study this hypothesis a modification of the whole ionization process is necessary. As shown in figure 4.4, an additional heatable pulsed source is installed. This source is filled with naphthalene, benzene and common MALDI matrix substances (1,8,9-anthracenetriol and 2,5-dihydroxybenzoic acid). The resulting orthogonal pulsed beam (ionizing beam) is ionized by the 193 *nm* laser beam. In this case, the laser beam is slightly displaced relative to the vertical axis (*z*) in order not to irradiate the original sample beam (molecular beam). A few *ns* after the ionization of the new beam (ionizing beam) the sample beam is switched on. This allows the formation of primary ions from the substances described above. Immediately afterwards these ions interact with the sample beam leading to some extent to the ionization of the particles.

Using this arrangement the feasibility of this laser-induced chemical ionization can be demonstrated for naphthalene. In this case it is possible to detect soot precursor particles without irradiating them directly with the laser beam. Consequently, their detection is achieved by means of laser-induced chemical ionization. To this end, however, high laser power densities are necessary. This makes it unlikely that the described increased ionization efficiency at low temperatures is due to such a laser-induced chemical ionization.

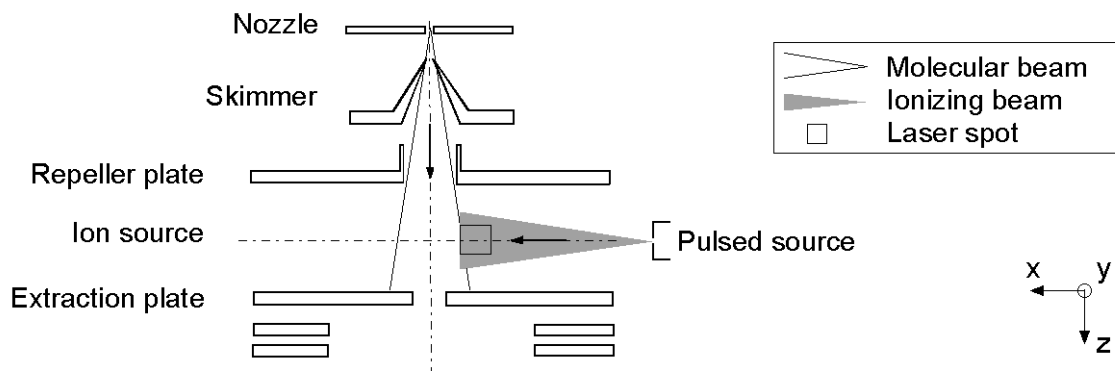


Figure 4.4.: Schematic diagram of the modified ionization chamber.

As described above, this effect is observed at low laser intensities.

These measurements also indicate that not every substance (not even aromatic) leads to laser-induced chemical ionization. The reasons for these different behaviors is unclear. An increase in ionization efficiency compared to the initial photo ionization set-up can unfortunately not be achieved and thus no improvement of the sensitivity is obtained.

Although the observed temperature dependent ionization efficiency is not completely understood, a sample temperature around 30°C is considered favorable to achieve high sensitivities. Hence the wall of the sampling line is always cooled. This in turn improves the reproducibility of the measurements as temperature effects are eliminated or at least reduced. Another effect of the thermostating of the sampling line is an improvement of the operating life time of the solenoid valve between sampling line and MS. The maximum valve operating temperature is specified as 200°C , however, the valve is not suitable for continuous operation at this temperature.

5. Photo Ionization

The ionization of the sample is a crucial step in the whole mass spectrometric procedure.

Compared to other ionization methods, like the more common electron impact ionization (EI), photo ionization can have a higher efficiency under low fragmentation conditions and particularly so when aromatic structures are involved. This increases the sensitivity of the method and augments the usable mass range.

EI results from the interaction between energetic electrons and gas phase molecules. Electrons are obtained from a heated filament, then accelerated by an electric field and directed to the volume containing the sample. The energy of these electrons is a function of the accelerating voltage. The latter usually varies between 5 and 100 V [58]. The degree of ionization depends on the electron energy (see figure 5.1) and the maximum ion yield is obtained at electron energies around 70 eV. Therefore, standard mass spectra are measured at this value. In this range, however, ions are formed with large excess of internal energy and this leads to fragmentation. Fragmentation patterns are useful to study the structure of compounds. In the case of fragile samples, however, the extent of fragmentation is often too large and no useful information is obtained. A decrease in electron energy reduces fragmentation but also the efficiency of the ionization and consequently the sensitivity. Additionally, electron guns are in practice difficult to operate at very low electron energies.

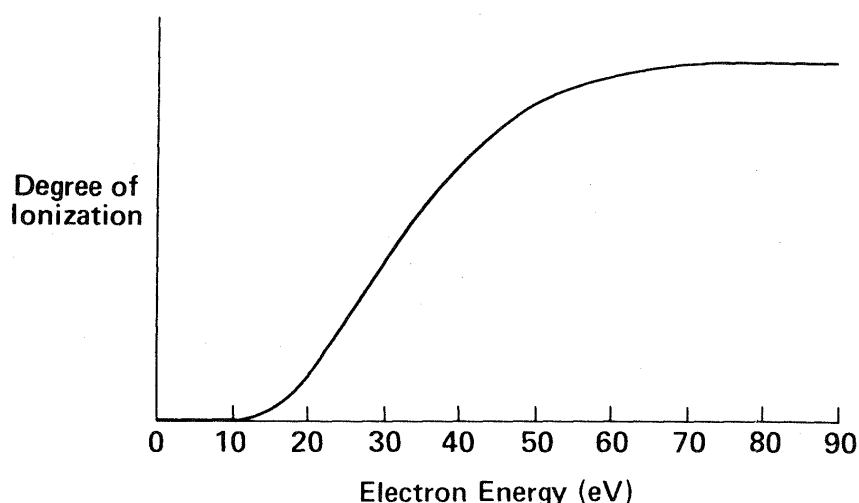


Figure 5.1.: Relationship between electron energy and degree of ionization for a mass spectrometer with an electron impact ion source as published by Middleditch [79].

When applying photo ionization, energy deposition can be controlled more precisely. This results in an effective ionization and large amounts of ions and relatively few frag-

ments can be obtained. The large photon density available in a very short time interval allows additionally multiphoton ionization (MPI) processes. Here, by absorption of several photons, the ionization of compounds with ionization energies higher than the energy of the individual photons is achieved. This increases notably the efficiency of the ionization process for most of the gas phase molecules. If the absorption of a photon leads to the occupation of a real electronically excited state, the life time of the intermediate state is much higher than those of the so-called virtual states. This kind of ionization is called resonance enhanced MPI and achieves very high ion yields.

Moreover, due to the pulsed character of the time-of-flight mass spectrometry, a pulsed ionization method like laser photo ionization is especially convenient.

The choice of the laser wavelength, i.e. the incident photon energy, depends on the sampled gas. In our case, it is attempted to detect combustion generated products, mainly PAHs, soot precursor particles and soot. To this end, the use of an ArF excimer laser ($\lambda = 193 \text{ nm}$ and $h\nu = 6.4 \text{ eV}$) is appropriate. The ionization energies of PAHs are generally higher than 7 eV [1, 35]. These components, however, are usually two-photon resonantly ionized at wavelengths in the low UV range [65]. As explained in section 8, multiphoton ionization processes are not likely in the case of solid particles. Soot particles, however, are characterized by ionization energies close to 5 eV [55] and thus single photon ionization processes are expected. As shown in the following chapters, it has been found that soot precursor particles can also be ionized at 193 nm .

5.1. Fragmentation Threshold

Although photo ionization is generally known to be a soft ionization method, the fluence of the laser beam, i.e. *number of photons/cm² · s*, must be adapted to the analyte under investigation. The goal is to achieve the largest amount of ions possible under the condition of negligible fragmentation.

The fluence of the laser beam can also be expressed as power density in MW/cm^2 . Different laser power densities are achieved by varying the laser pulse energy.

A series of measurements carried out at different laser power densities is presented below. Such an experiment allows the determination of the fragmentation threshold in the mass range of interest. This mass range extends from several thousand atomic mass units (u) up to several hundred thousand u and includes both soot precursor particles and primary soot. In this broad mass range the resolution is too low to allow the identification of the typical fragmentation patterns of individual ions (e.g. ratio of parent ions relative to fragment ions). The evolution of the mass distributions, however, can provide sufficient information to identify conditions in which particles are ionized without being fragmented.

A slightly sooting premixed ethylene/air flame ($\Phi = 2.1$) at atmospheric pressure is used as particle source (Burner I, as described in chapter 3). Particles are measured at

different laser power densities ranging from 0.05 MW/cm^2 to several hundred MW/cm^2 . Some results are shown in figures 5.2, 5.3 and 5.4.

The nominal output of the laser system is varied between 1.5 and 4.5 mJ . Lower laser intensities are accomplished through attenuation of the laser beam by means of one or two neutral density filters. In each case a square aperture ($5 \times 5 \text{ mm}$) is mounted directly behind the laser beam exit window. This ensures a well defined cross-sectional area of the laser beam. The resulting intensities with and without attenuation are measured with a laser power meter inserted just in front of the quartz entrance window of the ionization chamber. With these data the effective laser intensities and corresponding power densities in the ion source can be calculated. The transmission of the quartz window (approximately 85%) is taken into account. Under these conditions power densities from 0.05 to 0.89 MW/cm^2 are obtained.

To achieve higher power densities a cylinder lens is mounted behind the $5 \times 5 \text{ mm}$ aperture. This lens can be moved along an optical rail. Thus unfocused as well as focused conditions are obtained. In this case the shape of the cross-sectional area of the laser is rectangular. The wide side of this area is parallel to the repeller and the extraction plates. The resulting laser power densities are calculated on the basis of well-known optic relations from the laser intensity values reported above.

When the lens is displaced 10 mm relative to the focused position, laser power densities ranging from 0.63 to 11.12 MW/cm^2 are achieved by varying the nominal laser energy. In this arrangement the cross-sectional area of the laser at the ionization point is approximately 0.02 cm^2 . Under focused conditions the resulting beam width (h_f) at the ionization point can be approximated as

$$h_f = \frac{4\lambda f}{\pi H} \quad (5.1)$$

where λ is the laser wavelength, f the focal length and H the height of the laser beam. In this case the cross-sectional area of the laser is drastically reduced to approximately 0.00034 cm^2 . The variation of the nominal output of the laser then leads to laser power densities ranging from approximately 37 to several hundred MW/cm^2 .

In figure 5.2 two different mass ranges of the same spectra are shown. The whole mass range is split in two figures, due to the large mass range of this study and the large difference in signal intensity between the observed particle modes (note the different scales of the y-axis). Figure 5.2 a displays a mass range from 500 to 100000 u . The ion signals detected in this range are interpreted as soot precursor particles, as explained in detail in chapter 8. Figure 5.2 b, on the other hand, displays the mass range above 100000 u . In this case it is considered that these ion signals represent primary soot particles.

In the absence of undesired effects such as fragmentation or double ionization, upon increase of the photon density a proportional signal increase should result without any change of the mass distribution. This type of behavior is observed for primary soot parti-

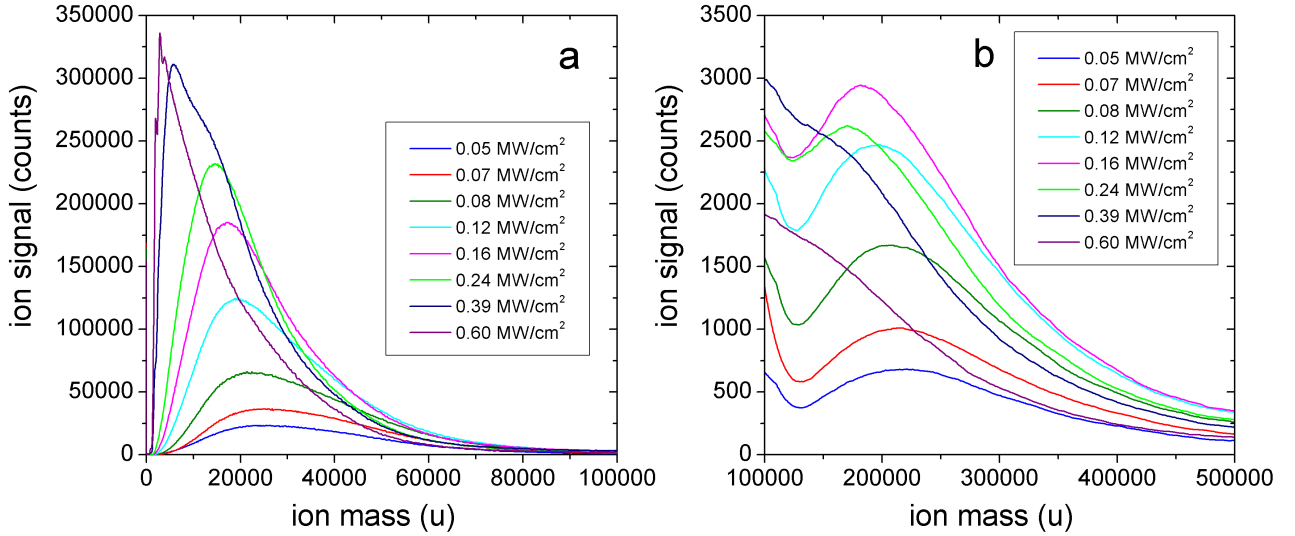


Figure 5.2.: Particle mass spectra from a premixed ethylene/air flame ($\Phi = 2.1$, Burner I) at atmospheric pressure and different laser power densities. a) Low mass range from 500 to 100000 u . b) Upper mass range from 100000 to 500000 u .

cles (figure 5.2 b) at laser power densities between 0.05 and 0.12 MW/cm^2 . In this range the signal intensities increase while the general shape of the mass distribution remains constant. At slightly higher power densities the ionization efficiency keeps increasing but the mass distributions shift clearly towards smaller masses. The latter is interpreted as a moderate fragmentation or surface ablation. Fragmented primary soot particles then appear at smaller masses than the original particles. This slightly alters the form of the mass distributions not only in the upper mass range ($> 100000 u$) but probably also at lower masses (see below). Above 0.16 MW/cm^2 the curves keep shifting to smaller masses but the most characteristic feature is the drop in signal intensity. Here the effect of fragmentation is very obvious and induces the increase of the signal intensities in the lower mass range.

For soot precursor particles fragmentation effects are also very pronounced. For soot precursor particles there is only a very small laser power density range where the mass distributions maintain their shape (see figure 5.2 a). In this range from 0.05 to 0.12 MW/cm^2 fragmentation can be excluded. Above 0.12 MW/cm^2 the mass distributions clearly shift to lower masses. This can be interpreted as the onset of fragmentation processes. The already mentioned fragmentation of larger primary soot particles above 0.12 MW/cm^2 , however, may affect the mass distributions in the range of the smaller soot precursor particles as well. Thus useful information about the ionization behaviour of soot precursor particles can hardly be extracted in this range.

A further influence on the shape of the distribution curves is provided by saturation effects of the detector. Above 0.24 MW/cm^2 the intense fragmentation of primary soot particles causes a strong rise of the number of ions reaching the detector. This leads

to the saturation of the multi channel plates. For this reason the spectra at 0.39 and 0.60 MW/cm^2 show characteristic deviations from the bell-shaped distribution. Such effects indicate that the proper choice of the operation voltage of the MCP is essential in order to avoid measurement artifacts leading to incorrect interpretations. In figure 5.3 the measurement at 0.39 MW/cm^2 shown in figure 5.2 a is compared with a measurement under the same flame and laser conditions but a reduced MCP voltage.

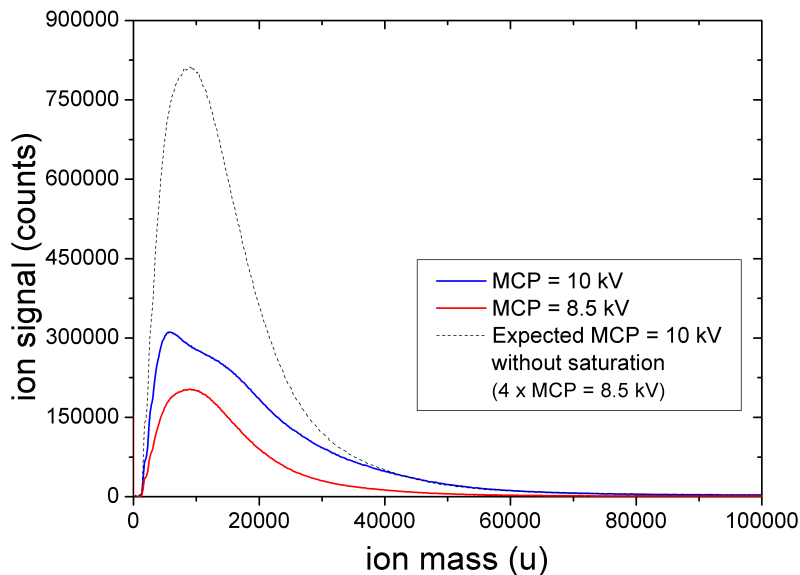


Figure 5.3.: Mass spectra of a premixed ethylene/air flame ($\Phi = 2.1$, Burner I) at atmospheric pressure at different MCP operation voltage. At MCP = 10 kV saturation effects are observed.

Without saturation effects, the mass distribution at MCP = 10 kV is expected to yield higher intensities than the distributions detected at lower MCP voltages, but similar characteristics. The expected mass distribution at MCP = 10 kV can be approximated as a multiple of the distribution found at MCP = 8.5 kV .

The formation of soot agglomerates in flames is well-known [34, 111]. However, the generation of small particles from agglomerated particles by laser fragmentation is excluded at the studied power density range as shown by Stipe et al. [100].

The presence of multiply charged ions is considered negligible. As described by Zimmermann et al. [115], multiply charged ions would lead to an alteration of the mass distributions. For instance, the appearance of an additional hump at half the mass of the main distribution mode would indicate the presence of doubly ionized particles. By increasing the laser power density, this hump would grow in intensity. Such effects are not observed.

The formation of metastable ions is usually indicated by a broadening of the ion signals [58]. In the studied mass range, such an effect would not be distinguishable due to the low resolution. At low laser power densities like the ones applied, however, the

formation of metastable ions is also considered negligible.

From this set of measurements it is clear that only very low laser power densities are suitable to study soot precursor particles. In order to avoid fragmentation, laser power densities below 0.12 MW/cm^2 are routinely applied for the measurements of this study.

5.2. Fullerenes

Fullerenes can result from excessive laser fragmentation. This can be observed in figure 5.4.

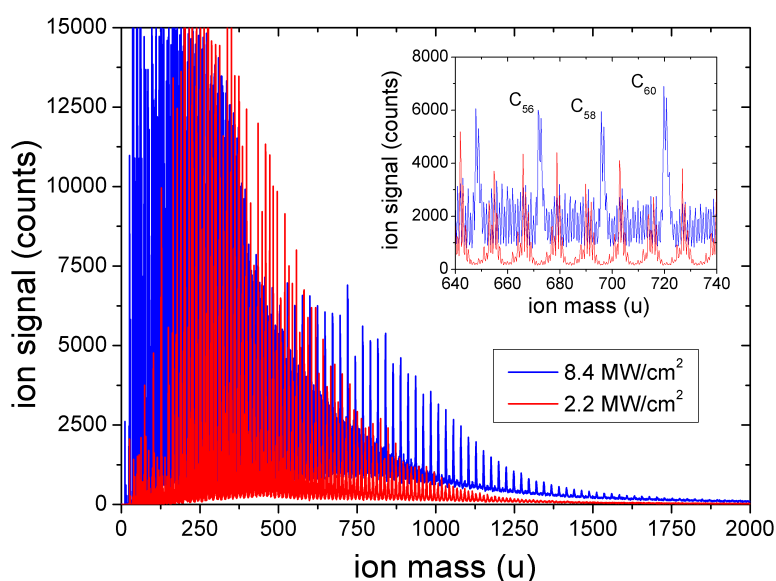


Figure 5.4.: Particle mass spectra of a premixed ethylene/air flame ($\Phi = 2.1$, Burner I) at atmospheric pressure and two different laser power intensities.

As described above, under focused and unfocused conditions high laser power intensities can be achieved. At laser power densities above 4 MW/cm^2 the typical PAH-distribution vanishes and fullerene ion signals are clearly observed from 500 up to 1500 u (see figure 5.4). This fullerene distribution is characterized by a C_{2n} cluster distribution containing well-known structures like the Buckminster fullerene (C_{60}).

Fullerene ions can be found in flames as described by Homann [54]. The formation of soot, however, is favored compared to the formation of fullerenes in rich combustion of non-aromatic fuel under normal pressures and low temperatures. For this reason, fullerenes are not expected to be formed in large amounts in the flames on study.

In our case fullerenes are considered to be laser-induced products rather than flame products. These fullerenes are formed in the ion source by reaction of ion molecule fragments which originate from soot precursor particles and, to some extent, also from soot. This is supported by the fact that fullerenes are only detected under conditions

where soot precursor particles and soot are known to fragment. In addition, in our experimental set-up fullerene signals are strongly affected by the pressure in the ion source, as shown under similar conditions by Schlüter [91]. High ion pressures reduce the mean free path of ions in the ion source. This favors the increase of reactive impacts among ion fragments and leads to higher rates of rearrangement. Consequently, fullerene signals increase.

The described rearrangement of ion fragments leading to the undesired formation of fullerenes may be compared with processes that have been developed for the synthesis of fullerenes. Similar fullerene distributions as the one shown have been found by Fulcheri et al. [41] when treating acetylene black with plasma. In this case, however, the applied energy density, pressure and reaction times are several orders of magnitude larger than in the current experimental conditions.

Fullerenes are three-dimensional closed-cage structures containing five-membered rings. For this reason it is expected that their formation is especially sensitive to the presence of the soot precursor particles detected by D'Alessio et al. (see chapter 8). These soot precursors are described as partially aromatic polymeric structures including five-membered rings [27, 105]. Their fragmentation, rather than the fragmentation of soot particles (mainly benzenoid structures), probably favors the relatively fast formation of fullerenes at the low pressure of the ion source. Fullerene signals may therefore be used as an indication for soot precursor particles.

6. Flame Measurements

The set of measurements presented in the following sections constitutes a detailed study of soot precursor particles in premixed flames and, to my knowledge, one of the first carried out by means of time-of-flight mass spectrometry.

Instead of the more generally used particle size distribution function (PSDF) as obtained by common aerosol measuring techniques such as SMPS, in our case particle mass distributions are measured.

These measurements demonstrate the presence of soot precursor particles in a wide range of rich stoichiometries in premixed ethylene/air and ethylene/oxygen flames at different pressures. The evolution of these particles in and outside the flame as well as their photo ionization behavior is investigated.

6.1. Particle Mass Distributions in Premixed Flames

6.1.1. Premixed Ethylene/Air Flames at Atmospheric Pressure

Variation of the Equivalence Ratio

In this section the influence of flame stoichiometry on the particle formation process is studied for equivalence ratios ranging from $\Phi = 1.59$ to 2.28. The equivalence ratio is varied in fine steps, allowing a monitoring of the evolution of the particle mass distributions. For this series of measurements Burner I is used. The nozzle of the sampling line is positioned in every case at $HAB = 12 \text{ mm}$ and centered in the axis of the burner. Some of the results are shown in figure 6.1.

For each set of operation conditions several repetitions are carried out. The general characteristics of the measured particle mass distributions (number of modes, maxima, etc.) are well reproducible. The intensity of the ion signals, however, shows strong fluctuations, in some cases, up to a factor of 6. The mass distributions presented in figure 6.1 are averages of those repeated measurements.

In general, the measured mass distributions are not unimodal. Rather, as many as three different modes (A, B, C) are observable. These three modes coexist in a very narrow window around $\Phi = 1.9$ and show different kinetic behavior:

- Mode A emerges in the flame at equivalence ratios slightly below the soot threshold¹ and it is observable up to stoichiometries well above it. This mode shifts to larger masses

¹The onset of soot formation in flames is usually roughly experimentally determined from the luminosity of the flame. The soot threshold of premixed ethylene/air flames at atmospheric pressure is considered

and exhibits increasing signal intensities for richer flames. At $\Phi = 1.76$ mode A has maximum values at approximately 1100 u while at $\Phi = 2.3$ this maximum appears at approximately 28000 u.

- Mode B is first observable at $\Phi = 1.76$, appears more pronounced at $1.80 < \Phi \leq 1.89$ and then, for richer conditions, is not any more distinguishable because of mass interference with mode A. In the range between $1.76 < \Phi \leq 1.85$, mode B also shifts to larger masses, with its maximum shifting from 17500 u to 22000 u. In addition, it shows increasing signal intensities with increasing equivalence ratios.

- Mode C appears at $\Phi \geq 1.85$ at mass values peaking around 200000 u (see inserts in figure 6.1). Its intensity increases with increasing equivalence ratios but remains one or two orders of magnitude below the intensity of mode A. This mode shifts also to larger masses as the equivalence ratio increases. At $\Phi = 2.01$ its maximum appears at approximately 175000 u and at $\Phi = 2.28$ at approximately 220000 u.

As explained later in detail, the ion signals corresponding to mode A and mode B are interpreted as soot precursor particles while mode C represents primary soot particles. These measurements demonstrate the existence of soot precursor particles in a wide range of equivalence ratios and show the broad mass detection range of the employed time-of-flight mass spectrometer. The main feature shown by these measurements is the bimodal nature of soot precursor particle distributions.

to be in the vicinity of $\Phi = 1.80$ [50]. In our case, the soot threshold could be visually estimated at $\Phi = 1.76$ based on the yellow coloration of the flame. The first hint of soot precursor particles (mode A) appears already at $\Phi = 1.71$, i.e. at stoichiometries slightly below the soot threshold.

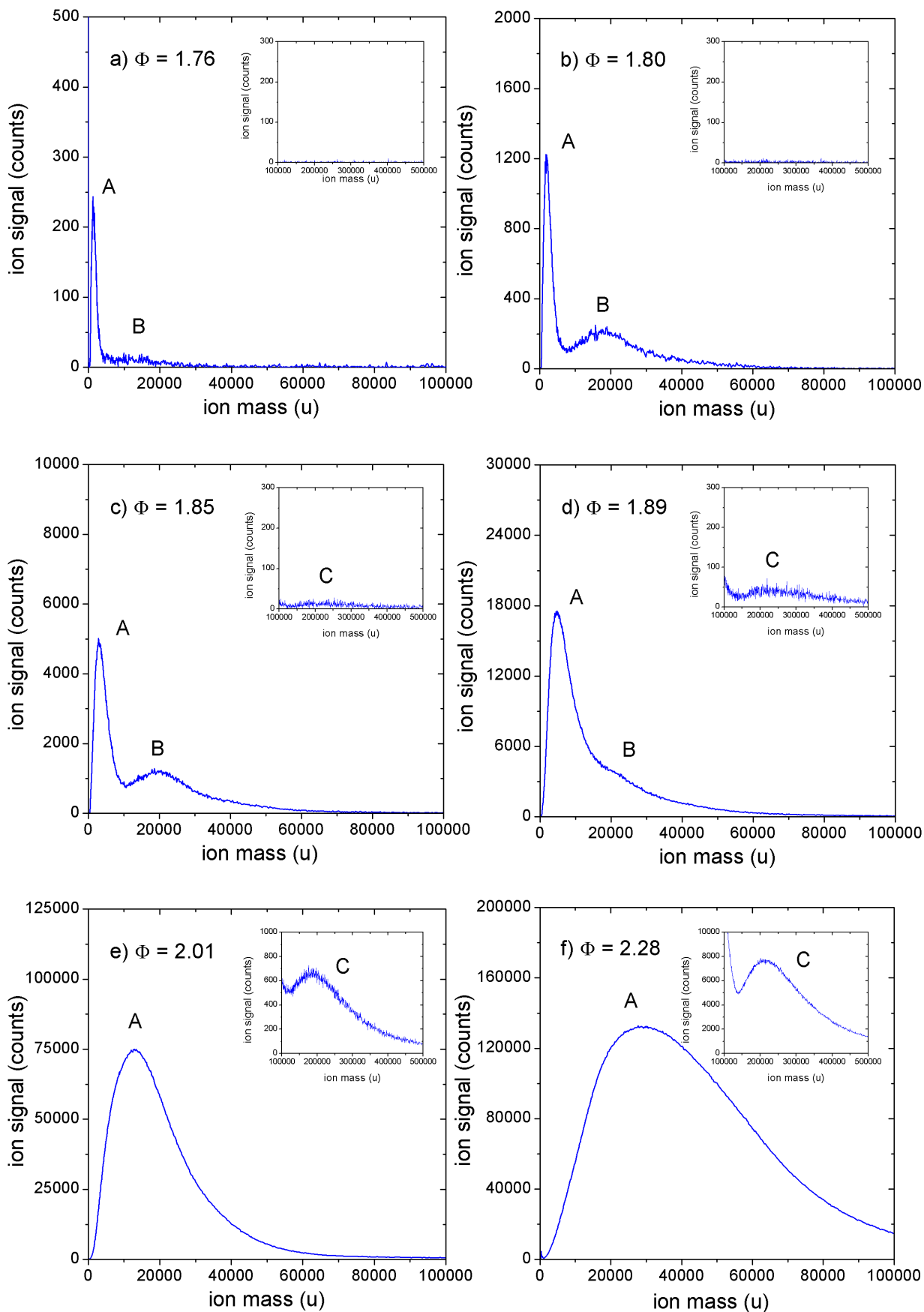


Figure 6.1.: Average particle mass distributions in a premixed flame at atmospheric pressure (Burner I) and different equivalence ratios. a) $\Phi = 1.76$. b) $\Phi = 1.80$. c) $\Phi = 1.85$. d) $\Phi = 1.89$. e) $\Phi = 2.01$. f) $\Phi = 2.28$. Note the different scales of the y axis.

Variation of the Height above the Burner

In order to study the evolution of the particle mass distributions in the flame, a series of measurements along the flame axis is carried out for different equivalence ratios. The position of the sampling line above the burner is varied in 2 mm steps. Because of geometric constraints the studied range extends from $HAB = 6 \text{ mm}$ to $HAB = 16 \text{ mm}$. In this case Burner I is used once again. Some of the results are shown in figures 6.2 and 6.3.

At $\Phi = 1.80$ (see figure 6.2) two different modes are observed: mode A ranging from 500 u up to approximately 5000 u and mode B extending from roughly 7000 u up to 30000 u . For both modes, an increase in the signal intensities for increasing HAB is observed. Furthermore mode A slightly shifts to larger masses with increasing HAB . Its maximum at $HAB = 6 \text{ mm}$ appears at approximately 1600 u while at $HAB = 16 \text{ mm}$ peaks at approximately 2000 u . Mode B, on the contrary, is characterized by a fairly constant maximum at approximately 18000 u .

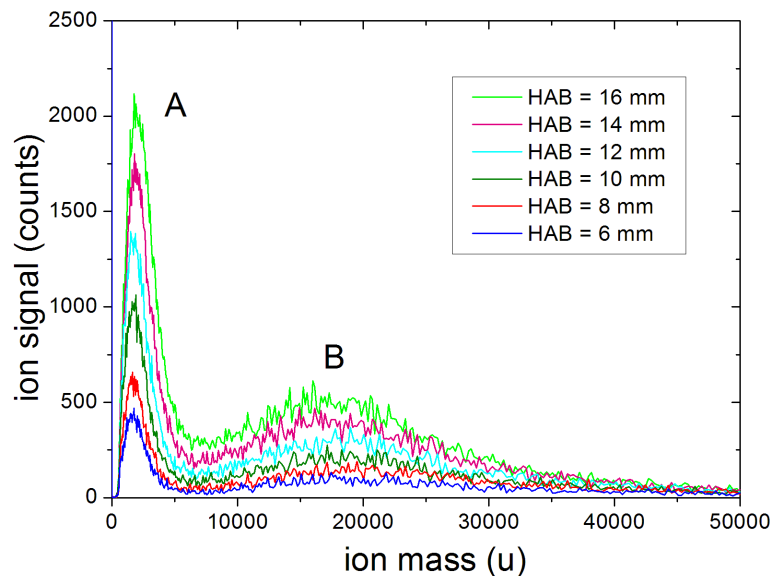


Figure 6.2.: Evolution of the particle mass distributions in a premixed flame at atmospheric pressure ($\Phi = 1.80$, Burner I) for different heights above the burner. Note the different scales of the y axis.

At $\Phi = 2.10$ (see figure 6.3) also two modes are observed with, however, a different meaning. In this case, mode A extends from approximately 500 u up to 100000 u and entirely covers potential contributions of mode B. Mode C (see insert) ranges roughly from 100000 u up to 800000 u . For both modes, again, increasing signal intensities are observed with increasing HAB . This trend, however, is not found for the measurement at $HAB = 16 \text{ mm}$, where a signal decay is observable for both modes A and C. The latter is probably related to the proximity of the stabilization plate, which influences the flow field as well as the temperature in the flame. In the range from $HAB = 6 \text{ mm}$ to

$HAB = 16 \text{ mm}$, mode A shifts by approximately 3000 u to larger masses while mode C peaks at approximately 200000 u throughout the covered HAB range. The signal intensities of mode C are roughly 2 orders of magnitude lower those of mode A.

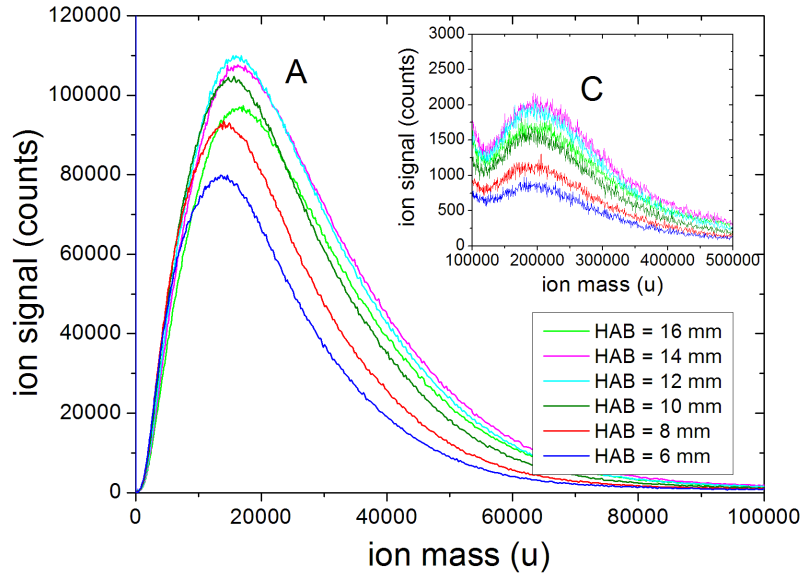


Figure 6.3.: Evolution of the particle mass distributions in a premixed flame at atmospheric pressure ($\Phi = 2.10$, Burner I) for different heights above the burner. Note the different scales of the y axes.

The measurements shown in this section demonstrate that soot precursor particles (mode A and B) are found well above the flame front. In the studied range the evolution of the soot precursor particles is in general characterized by a gain in intensity and by a very weak mass growth with increasing height above the burner. The persistence of soot precursor particles along the flame axis suggests their permanent nucleation as otherwise losses by coagulation with larger particles or oxidation would reduce their signal intensities. In addition, the weak mass growth of soot precursor particles along the flame axis indicates that surface growth in the flame is probably not a dominant effect or is counterbalanced by consumption reactions.

Apparently soot particles (mode C) do not grow with increasing height above the burner. This behavior, as discussed in chapter 8, deviates from well established data found in the literature and probably has to be attributed to limitations of the MS.

Photo Ionization Behavior

The photo ionization behavior of the different characteristic modes (A, B, C) of the mass distributions described above is now investigated. To this end measurements in slightly sooting premixed ethylene/air flames at atmospheric pressure ($\Phi = 1.85$ and 2.1 , Burner I) are carried out.

Considering a multi photon ionization process, the number of parent ions formed during ionization, and thus the corresponding signal intensities, depend on the photon flow density or laser power density in the following way [65, 90]:

$$S \propto I^n \quad (6.1)$$

where S is the signal intensity, I the ionization laser power density and n the ionization order.

In this context, logarithmic plots of the ion signal vs. the ionizing laser power density are very useful. At low laser power densities, $S(I)$ plots are straight lines, their slopes yielding the ionization order. At high laser power densities, however, different fragmentation and/or ionization processes may interfere. This complicates the interpretation of the dependency between ion signal and ionizing laser power density.

At high laser power densities fragmentation of parents ions can cause a decrease of the slope of the logarithmic plot of the ion signal vs. the laser power density [90]: The fragmentation of parents ions leads to the formation of daughter ions. This implies a decrease on signal intensity of the parent ions and thus a reduction of the mentioned slope.

A similar effect would be observed if saturation effects are present [65, 71]. Considering a resonant two photon ionization (see figure 6.4), saturation occurs if the lower energy level (E_0) is significantly depleted. In this case, due to the long lifetimes of the excited resonant levels (E_1), most of the molecules are in an excited state. Saturation can also occur if the excited level population reaches a quasi steady state, i.e. $\frac{dN_{E_1}}{dt} = 0$ where N_{E_1} is the number of molecules in the intermediate state. This happens at high laser power densities when the formation rate of intermediate states is high compared with their ionization rate ($a_1 \gg a_2$) and the stimulated emission (and consequently deactivation) of excited states gains in importance.

Under any of these saturation conditions an increase in laser power density no longer provides the corresponding increase in excited level population. This results in a deviation from the straight line in the logarithmic plot of the ion signal vs. the laser power density. The slope of this plot may decrease from $n = 2$ to $n = 1$.

At high laser power densities and from the $S(I)$ plots alone, the onset of fragmentation can not be easily distinguished from the onset of other effects like saturation. In this range estimations about the ionization order based on $S(I)$ plots are not advisable.

In our case, the onset of fragmentation is determined from the evolution of the particle mass distributions at different ionizing conditions, as already shown in chapter 5. The ionization order of the different characteristic modes (A, B, C) of the mass distributions is then obtained from the slope of the $S(I)$ plots at low ionizing laser power densities. Laser power densities ranging from 0.05 MW/cm^2 (lowest laser power density allowing detectable ionization) to the fragmentation threshold are considered. In this low power

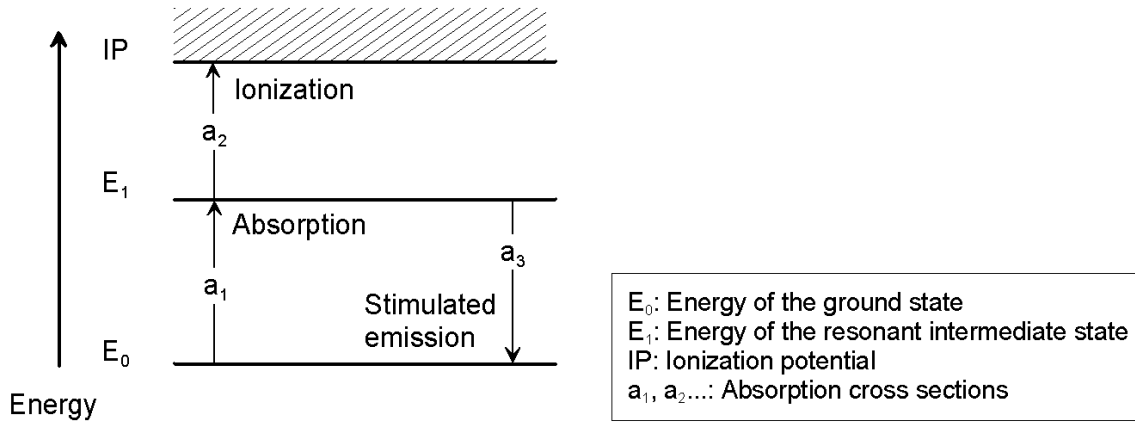


Figure 6.4.: Simplified representation of a resonant two photon ionization. Note that not all possible energy transfer pathways like spontaneous emission (fluorescence), intramolecular internal conversion, etc. have been represented.

density range saturation effects are considered negligible.

In figure 6.5 a the evolution of the particle mass distributions of a premixed flame ($\Phi = 1.85$) at atmospheric pressure for different laser power densities ranging from 0.05 to 0.79 MW/cm^2 is shown. For clarity, the curves are smoothed. Mode B, peaking at approximately 20000 u , is clearly observed. The corresponding logarithmic plot of the ion signal intensity (at 20000 u) vs. the ionizing laser power density is shown in figure 6.5 b. In this case an ionization order of approximately 1 is obtained.

In the same way, yet for laser power densities ranging from 0.67 to 8.40 MW/cm^2 , the evolution of the particle mass distributions (again smoothed) and the corresponding $S(I)$ plot are represented in figure 6.6. In this range the onset of fragmentation is observed. At laser power densities higher than 2.24 MW/cm^2 the mass distributions shift to smaller masses. This coincides with the decay of the slope in the plot of ion signal intensity vs. laser power density.

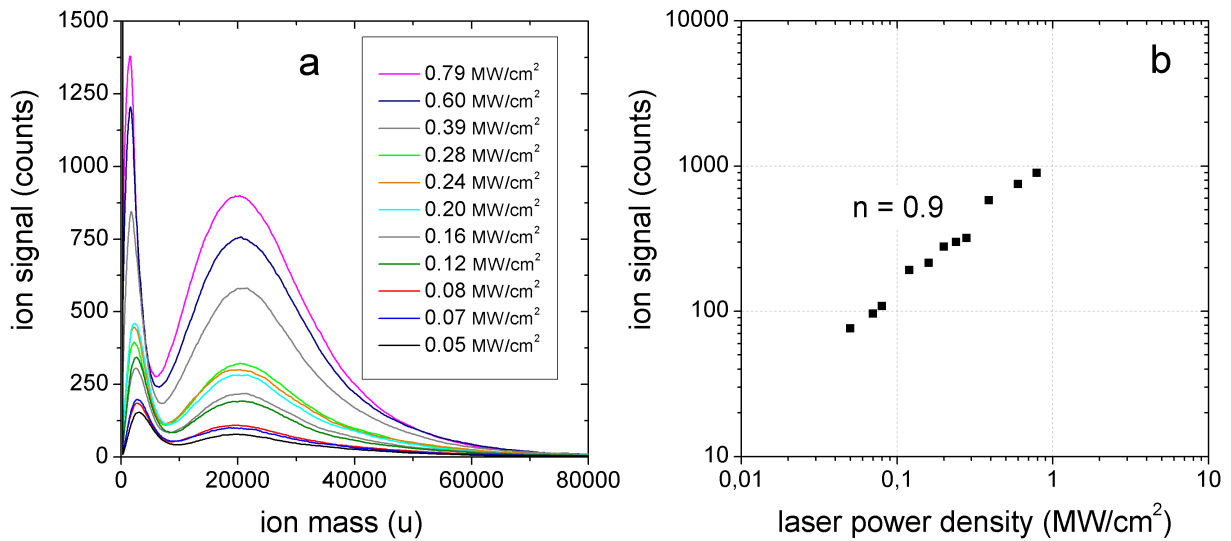


Figure 6.5.: a) Evolution of the particle mass distributions for different laser power densities ranging from 0.05 to 0.79 MW/cm^2 (smoothed). b) Dependence of signal intensities of mode B (peaking at 20000 u) on the laser power density. Source: Premixed ethylene/air flame ($\Phi = 1.85$, Burner I) at atmospheric pressure.

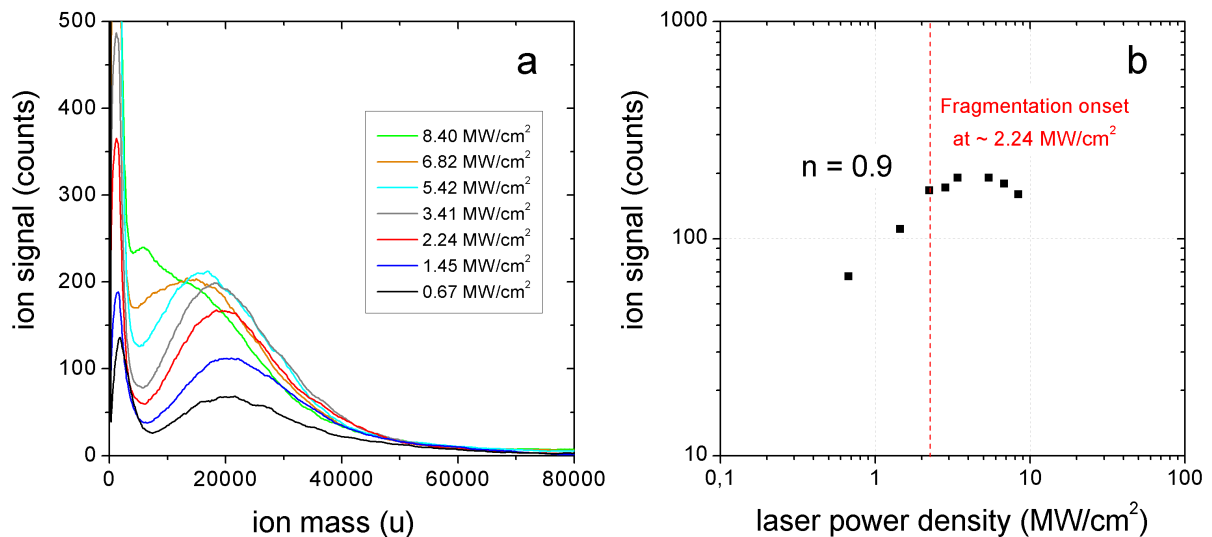


Figure 6.6.: a) Evolution of the particle mass distributions for different laser power densities ranging from 0.67 to 8.40 MW/cm^2 (smoothed). b) Corresponding dependence of signal intensities of mode B (at 20000 u) on the laser power density. Source: Premixed ethylene/air flame ($\Phi = 1.85$, Burner I) at atmospheric pressure.

In order to combine all the information contained in figures 6.5 and 6.6, the ionization volume must be taken into account. In the low laser power density range, as explained in chapter 5, the laser is not focused and its cross-sectional area is approximately 0.25 cm^2 . To achieve higher laser power densities the laser must be slightly focused, yielding a cross-sectional area of approximately 0.02 cm^2 at the ionization point. It is assumed that the ionization volume depends on the cross-sectional area of the ionizing laser alone. Thus the ion signal intensities in figure 6.7 are normalized with respect to this parameter. This plot shows the increasing efficiency of the ionization process with increasing laser power density from the first detectable signals to the onset of fragmentation around 2.24 MW/cm^2 . Above this point the signal intensity of mode B decays. The resulting ionization order is $n_{mode B} = 0.9$.

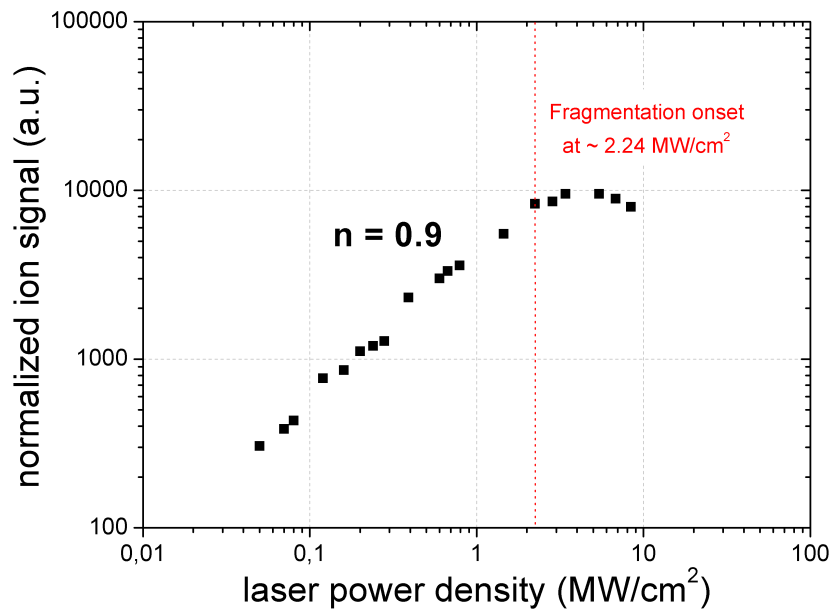


Figure 6.7.: Dependence of normalized signal intensities of mode B (at $20000 u$) on the laser power density. Source: Premixed ethylene/air flame ($\Phi = 1.85$, Burner I) at atmospheric pressure.

The ionization behavior of mode A and C particles can be observed in figure 6.8. These data originate from the mass distributions shown in chapter 5 and correspond to a flame at $\Phi = 2.1$. The signal intensities represented in figure 6.8 a are the corresponding values at $25000 u$, maximum of mode A for the lowest laser power density applied. In figure 6.8 b the signal intensities at $215000 u$ (maximum of mode C again for the lowest laser power density applied) are plotted vs. the corresponding laser power densities. In both cases there is just a short range in the laser energy before the onset of fragmentation is observed at approximately 0.12 MW/cm^2 . Thus the ionization order obtained from this series of measurements may contain a relative large error. Nevertheless, for both modes the ionization order is clearly above 1 ($n_{mode A} = 1.9$, $n_{mode C} = 1.5$).

The measurements presented in this section show that soot precursor particles consti-

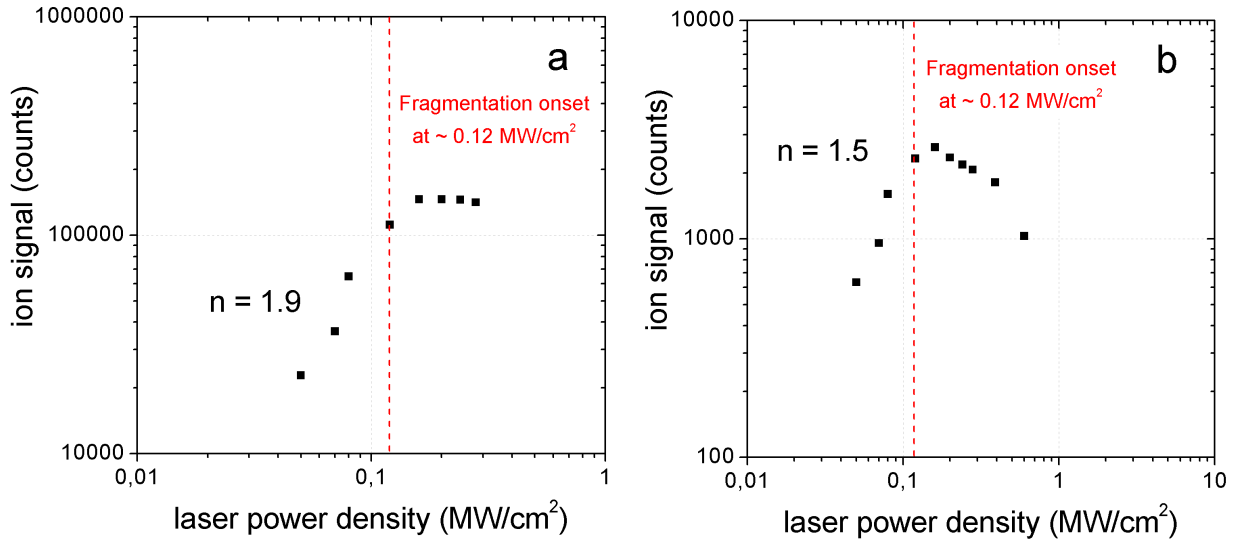


Figure 6.8.: Dependence of signal intensities of a) mode A (25000 u) and b) mode C (215000 u) on the laser power density. Source: Premixed ethylene/air flame ($\Phi = 2.1$, Burner I) at atmospheric pressure.

tuting mode A are clearly different from mode B particles with regard to their photo ionization behavior. The ionization order of mode A particles is $n_{mode\ A} = 1.9$ while mode B particles show an ionization order of $n_{mode\ B} = 0.9$. In addition, the fragmentation threshold for particles constituting mode A ($\sim 0.12\ MW/cm^2$) is significantly lower than that for mode B ($\sim 2.24\ MW/cm^2$).

Particles outside of the Flame

The results presented so far correspond to measurements carried out in flames operated with a stabilization plate. Alternatively, the available burners also allow the use of a co-flow. This method of stabilizing the upper part of the flame, however, is not favorable. The high co-flow rates, needed to keep the flame stable, interact with the quartz probe and alter the flow conditions in the flame. Thus the disturbance of the flame during the measurements, already visible under the reported conditions, is greater than when using the stabilization plate.

Nevertheless, it is interesting to test whether soot precursor particles are able to survive the different flame regions and be emitted. For this reason a co-flow stabilized ethylene/air flame is used to study the evolution of the ion mass distributions at different HAB including positions well above the visible flame. Two different co-flow gases are used: Nitrogen and compressed air. In both cases a flow of approximately 70 L/min is adjusted. The visible flame (luminous cone-shaped zone) stretches in each case approximately 40 mm from the surface of the burner up to the tip of the luminous cone.

Figure 6.9 shows the evolution of the ion mass distributions along the axis of a pre-

mixed ethylene/air flame at $\Phi = 1.80$. For clarity, the mass spectra corresponding to the measurements at $HAB = 60 \text{ mm}$ are again shown in figure 6.10. Here, also a background measurement is included.

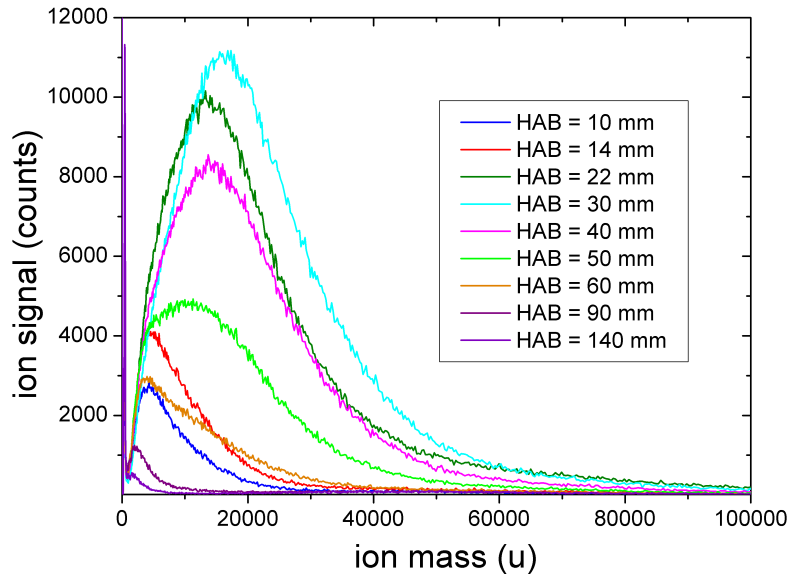


Figure 6.9.: Evolution of the ion mass distributions along the axis of a premixed ethylene/air flame ($\Phi = 1.80$, Burner II). The flame is stabilized by means of a 70 L/min shroud of nitrogen.

Maximal intensities are found at $HAB = 30 \text{ mm}$. This represents also the boundary between two distinguishable ranges of the evolution of the mass distributions. For increasing heights above the burner up to $HAB = 30 \text{ mm}$, the signal intensities grow while the mass distributions shift to larger masses. This indicates an increase in the number of particles along with a size increase. Above $HAB = 30 \text{ mm}$, the evolution of the mass distributions shows a different tendency. In this range a loss of signal intensity is observed with increasing HAB . This corresponds to a loss in particle number attributed mainly to the coagulation of soot precursor particles with larger particles (soot particles). These coagulation losses above $HAB = 30 \text{ mm}$ cannot be balanced by the formation of new particles and consequently the particle number decreases. The size reduction of the particles above the visible flame, indicated by a shift towards smaller masses, is interpreted to result from oxidation processes, as demonstrated below.

When comparing the actual mass distributions to the ones shown in section 6.1.1, the more prominent feature is a marked deviation of the mass spectra below 100000 u for relative low equivalence ratios. As an example, compare figure 6.2 and figure 6.9. Both refer to measurements carried out at the same equivalence ratio ($\Phi = 1.80$), at similar heights above the burner and under similar experimental conditions. Nevertheless, in the first case a bimodal distribution is clearly observed below 100000 u while in the second case just one mode is detected. The signal intensities of both experiments can not be directly compared due to different signal processing chains employed.

The experimental conditions distinguishing both series of measurements are the way of stabilizing the flame and the slightly different burners employed. The influence of each of these parameters is investigated in another series of measurements along the axis of the bronze-burner (Burner II), this time equipped with a stabilization plate and without co-flow. The obtained results are in good agreement with the ones obtained with co-flow in the same burner, as again just one mode below $100000 u$ is detected. This indicates the influence of the burner geometry. It may be concluded that particle size distributions cannot be characterized solely by Φ since other experimental factors can have significant effects.

Nevertheless, when carefully observing the set of measurements shown above and once again in figure 6.10, a bimodal mass distribution appears outside of the flame. A first mode ranging from roughly $500 u$ up to $10000 u$ together with a second broader mode, peaking at approximately $50000 u$, are observed. Above $HAB = 60 mm$ the first mode gradually decreases in intensity and shifts to smaller masses whereas the second mode remains stable. The included background measurement assures that these signals originate from the flame. The first mode is considered analogous to mode A, described in the previous sections. In the same way, the second mode probably corresponds to mode B. Mode B particles seem to be more stable upon oxidation than mode A particles.

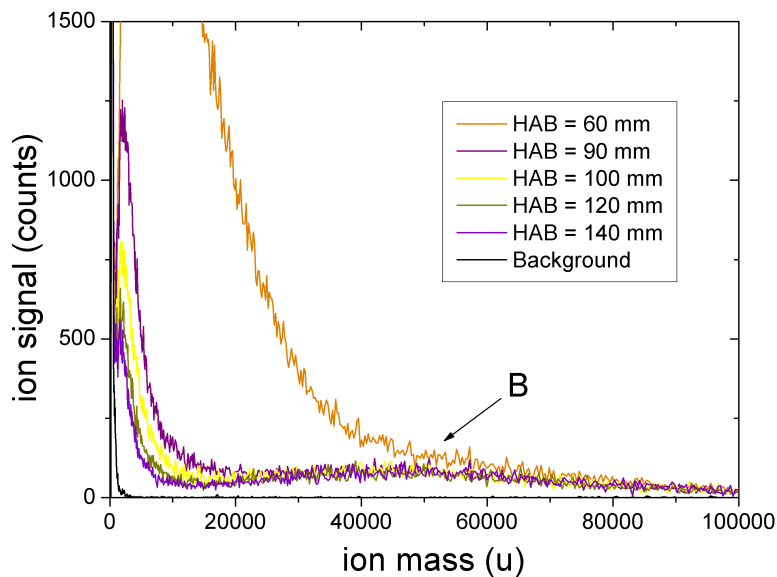


Figure 6.10.: Evolution of the ion mass distributions along the axis of a premixed ethylene/air flame ($\Phi = 1.80$, Burner II). The flame was stabilized by means of a $70 L/min$ shroud of nitrogen. A background measurement is included.

To stimulate possible oxidation processes occurring above $HAB = 30 \text{ mm}$, the shroud of nitrogen is substituted by a compressed air co-flow. The corresponding series of measurements under these conditions is presented in figure 6.11.

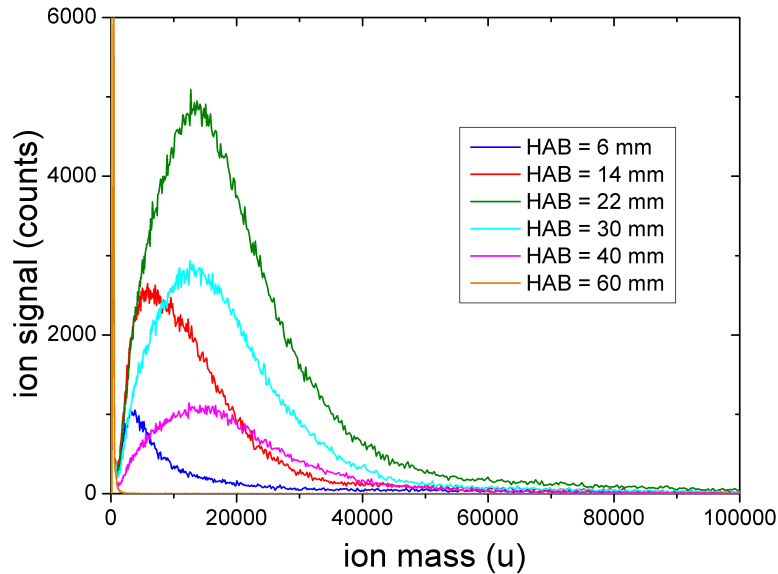


Figure 6.11.: Evolution of the ion mass distributions along the axis of a premixed ethylene/air flame ($\Phi = 1.80$, Burner II). The flame was stabilized by means of a 70 L/min shroud of compressed air.

In this case, the evolution of the mass distributions along the flame axis is qualitatively similar to the one observed when using nitrogen as co-flow, particularly so for low values of HAB . Nevertheless, the signal intensities are definitively smaller at any HAB . Additionally, the intensity maximum is observed to occur earlier in the flame ($HAB = 22 \text{ mm}$) and all signals disappear shortly behind the visible flame. This confirms the role of oxidation reactions in the formation process and especially in the consumption of particles. When supplying more oxygen (compressed air shroud instead of nitrogen shroud), the oxidation rate increases. Under these conditions particles not only reduce their size but even disappear completely already at lower heights above the burner.

For an overview, figure 6.12 shows the mass weighted integrals (from 1000 u up to 200000 u) of the spectra corresponding to the measurements presented above for the different HAB and co-flow settings. The mass weighted integrals represent the total mass associated to soot precursor particles in the indicated range. The concentration of these particles is approximately the same for both nitrogen and air co-flows flames within the first 20 mm above the burner. At higher HAB the nitrogen co-flow flame shows higher concentrations with a maximum around $HAB = 30 \text{ mm}$. In the case of the air co-flow flame, the maximum appears earlier in the flame (approximately at $HAB = 22 \text{ mm}$). In both cases, above this maximum, the concentration of soot precursor particles drops. For the nitrogen co-flow flame soot precursor particles are still detectable well above the visible flame front. Their concentrations remain stable from $HAB = 100 \text{ mm}$ up to

140 mm mainly due to the presence of particle signals around 50000 u (mode B). In the case of the air co-flow flame the concentration drop is significantly stronger, however, soot precursor particles are still detectable above $HAB = 40$ mm, i.e. outside the flame.

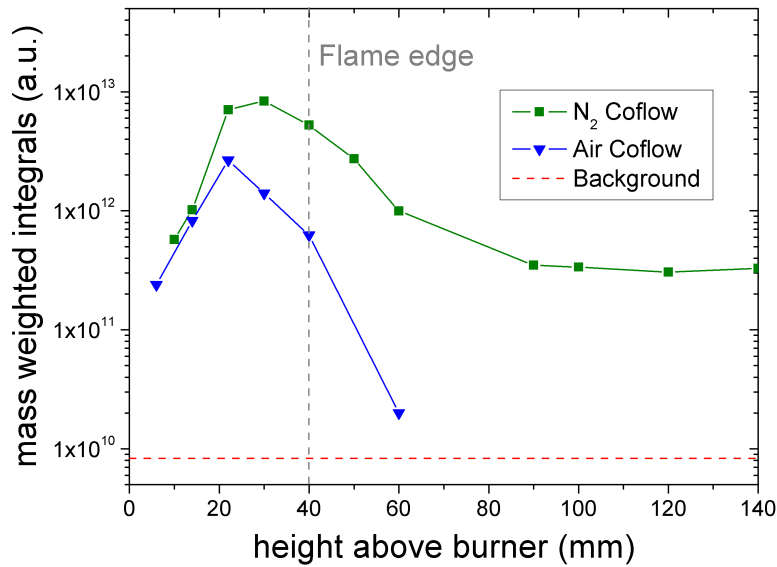


Figure 6.12.: Mass weighted integrals of soot precursor particles along the axis of a co-flow stabilized ethylene/air flame ($\Phi = 1.80$, Burner II). The flame edge at $HAB = 40$ mm is indicated.

6.1.2. Premixed Ethylene/Oxygen Flames at Low Pressure

Variation of the Equivalence Ratio

In this section the influence of the equivalence ratio on the particle mass distributions of an ethylene/oxygen low pressure flame is studied.

To this end the low pressure burner described in chapter 3 is operated at 160 *mbar* and a series of measurements with equivalence ratios ranging from $\Phi = 1.89$ to 3.00 is carried out². Each of the experimental points is measured several times. The features of the particle mass distributions are well reproducible, however, the signal intensities show large fluctuations. The average particle mass distributions are presented in figure 6.13. These results are in good agreement with the results shown in previous sections and verify the existence of soot precursor particles in a large range of experimental conditions.

²For the measurement at $\Phi = 3.00$, the MCP voltage is reduced by 10% to avoid saturation. This complicates the comparison with measurements at other stoichiometries. Nevertheless, for the sake of completeness, this measurement is included in figure 6.13. In addition, at $\Phi > 3.00$, a contraction of the flame shape is observed.

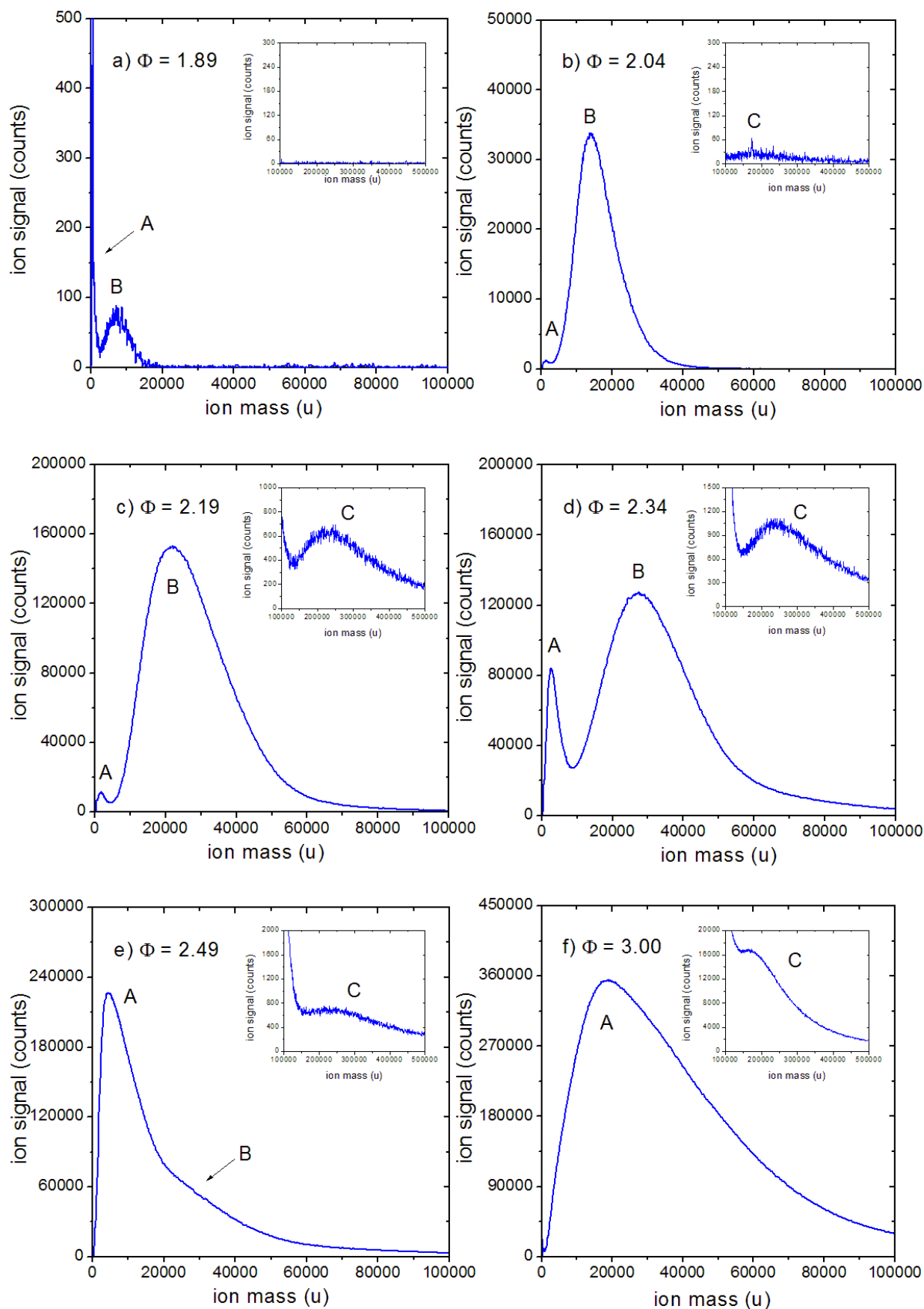


Figure 6.13.: Average particle mass distributions in a premixed ethylene/oxygen flame at 160 *mbar* and different equivalence ratios. a) $\Phi = 1.89$. b) $\Phi = 2.04$. c) $\Phi = 2.19$. d) $\Phi = 2.34$. e) $\Phi = 2.49$. f) $\Phi = 3.00$ and reduced MCP voltage. Note the different scales of the y axes.

In this case, as for the flame at atmospheric pressure, three different modes (A, B and C) are observed. The first particle signals are detected at $\Phi = 1.89$, slightly below the soot threshold³.

A first mode (mode A) is observed in the whole stoichiometric range. This mode shifts to larger masses and exhibits increasing signal intensities for richer flame conditions. At $\Phi = 1.89$ mode A peaks at approximately $800 u$ while at $\Phi = 3.00$ this maximum appears at approximately $19000 u$. At $\Phi \geq 2.49$, mode A dominates the low mass range ($< 100000 u$) of the particle spectra.

A different particle mode (mode B) is formed in the range $\Phi < 2.49$. Mode B also shifts to larger masses for increasing equivalence ratios. The intensity of mode B, already present at $\Phi = 1.89$, experiences a first increase with increasing Φ , followed by a progressive signal intensity decline at $\Phi \geq 2.19$. At $\Phi > 2.49$, mode B is not anymore distinguishable as the particle mass distributions are apparently dominated by an excess of mode A particles.

Above $\Phi = 2.04$, a third particle mode (mode C) appears (see inserts in figure 6.13). This mode peaks around $200000 u$ and shows, in general, also increasing intensities for increasing equivalence ratios together with a slight shift towards larger masses.

In general, all the features described for the atmospheric flame are again found in this low pressure flame but at different (higher) equivalence ratios. This is related to the well known shift of the soot threshold with pressure, as explained by Glassman [44]: A pressure decrease lowers the rates of all the reactions in the nucleation process. Thus, in all types of flames, the lower the pressure the lower the tendency to soot. Accordingly, the soot threshold shifts to richer conditions with decreasing pressure. The formation of soot precursor particles is expected to be affected in the same way.

When comparing the measurements in section 6.1.1 to those of this section, the presence of inert diluent gas (nitrogen) in the ethylene/air atmospheric flame should be taken into account. Inert diluents reduce the partial pressure of precursor reactants [44] and also shift the soot threshold to richer conditions. Thus, the reported shift of the soot threshold in the ethylene/oxygen flame is the consequence of two opposite effects: The expected shift of the soot threshold towards higher equivalence ratios due to the reduction of the pressure is partially compensated by the elimination of the diluent gas. In addition, small variations of the soot threshold are also expected due to the different burner configurations [17].

Variation of the Operation Pressure

In this section the influence of the operation pressure, independently from other parameters like inert diluents or burner configuration, is studied in an ethylene/oxygen low pressure flame. To this end, the series of measurements presented in the previous section are repeated at $120 mbar$ under the same experimental conditions, i.e. identical burner configuration, flame and sampling position. Each of the experimental points is measured

³For this low pressure flame the soot threshold is visually roughly estimated at $\Phi = 1.98$.

several times. The general features of the distributions are once again well reproducible while the signal intensities show fluctuations. The corresponding average particle mass distributions are shown in figure 6.14.

The measurements at 120 *mbar* correspond to a slightly shorter flame reaction time than the measurements at 160 *mbar* since in both cases $HAB = 37 \text{ mm}$. This is due to the different operating pressures and the related flame stretch. These sets of measurements, however, will be considered in the following as comparable. This assumption is based in the measurements shown in section 6.1.1. For this series of measurements the general characteristic of the particle mass distributions remains roughly constant for a large HAB range. Consequently, small changes in the sampling position should not influence our data.

As expected, when comparing both figure 6.13 and figure 6.14, the most prominent features are the different equivalence ratios at which the first particles appear. At 160 *mbar* the first particle mass distributions appear at $\Phi = 1.89$ while at 120 *mbar* a higher equivalence ratio is needed to observe similar particle mass distributions. This is consistent with the reduction of the nucleation rates due to decreased pressure as explained in the previous section. For the flame at 120 *mbar* soot precursor particles are first observed at equivalence ratios slightly above the soot threshold⁴.

⁴For this premixed ethylene/oxygen flame at 120 *mbar* the soot threshold is visually roughly estimated at $\Phi = 2.00$

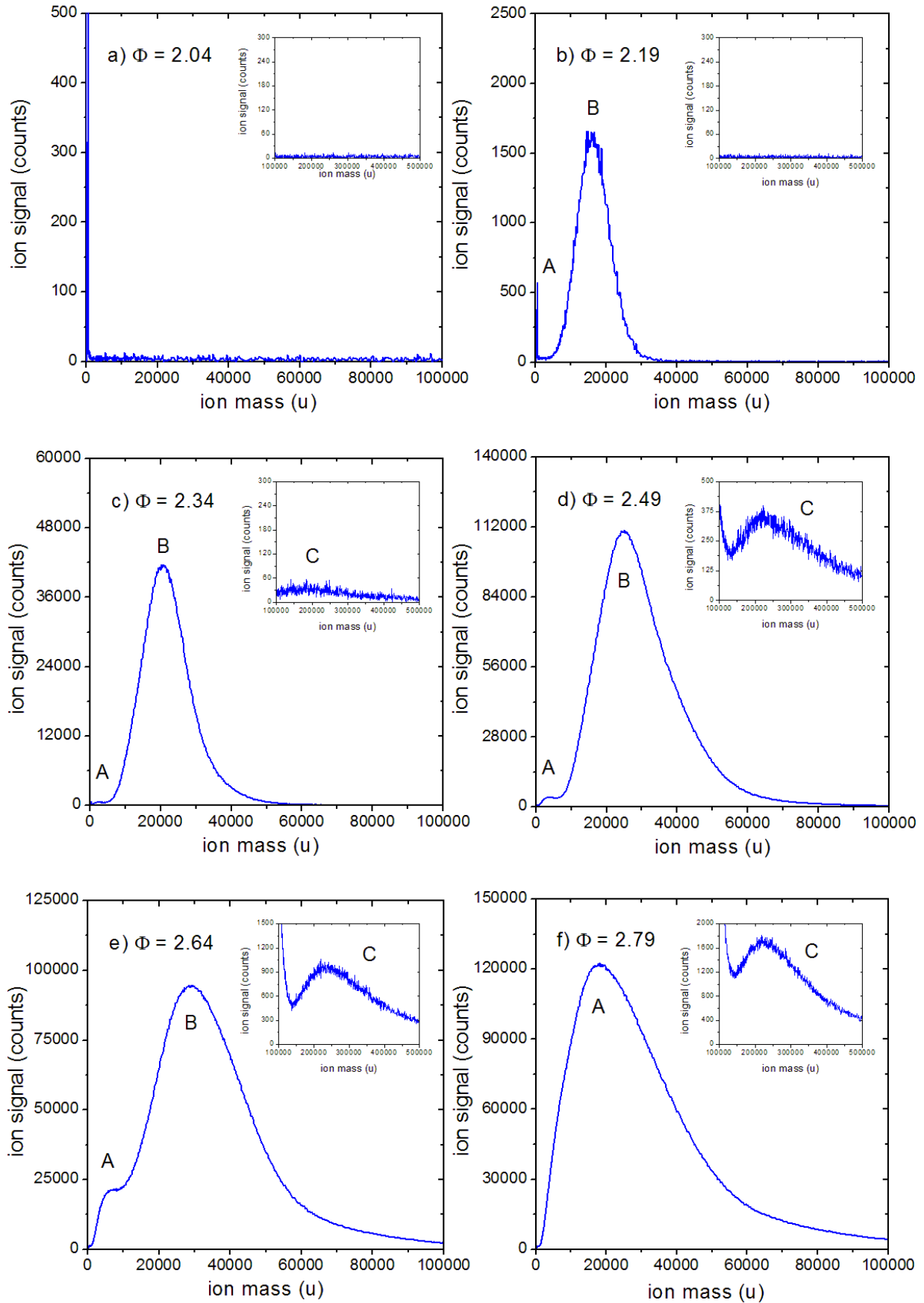


Figure 6.14.: Average particle mass distributions in a premixed ethylene/oxygen flame at 120 mbar and different equivalence ratios. a) $\Phi = 2.04$. b) $\Phi = 2.19$. c) $\Phi = 2.34$. d) $\Phi = 2.49$. e) $\Phi = 2.64$. f) $\Phi = 2.79$. Note the different scales of the y axis.

6.2. Conclusions

The measurements presented in this chapter constitute one of the first studies of flame particles carried out by means of time-of-flight mass spectrometry in a mass range extending up to approximately $1000000 u$. The goal of these measurements is the investigation of soot formation focusing on soot precursor particles. Consequently, the lowest mass range ($< 1000 u$) of the mass spectra (gas phase spectrum) has not been considered.

The main feature shown by these measurements is the fact that soot precursor particle distributions can show a bimodal character. Additionally, particles constituting the different particle modes (modes A and B) show different kinetic and ionization behaviors. As discussed in chapter 8, they probably represent soot precursor particles of different nature.

The signals detected in the mass range up to $100000 u$ are interpreted as soot precursor particles, as discussed in detail in chapter 8. These particles are found in atmospheric premixed ethylene/air flames as well as in premixed ethylene/oxygen flames under low pressure conditions. In general, the particle mass distributions associated with modes A and B exhibit an asymmetric, skewed shape with a long tail at large masses.

Soot precursor particles emerge in the flame at stoichiometries close to the soot threshold. They are found well above the flame front and show a permanent nucleation along the flame axis. In addition, soot precursor particles are characterized by a weak mass growth in the flame.

The soot precursor particles associated with mode A appear in a wide range of stoichiometries and experimental conditions. This mode shows a moderate mass increase with increasing equivalence ratios and increasing height above the burner. In addition, it shows increasing signal intensities with increasing equivalence ratios.

Mode B, on the other hand, shows up just in a narrow stoichiometry window and seems to be strongly affected by experimental conditions (e.g. burner design and configuration). This mode, similar to mode A, shifts to larger masses with increasing equivalence ratios. For increasing height above the burner, however, mode B does not show any appreciable mass growth. Above a certain equivalence ratio, which depends on the unburned flame gases, the operation pressure, etc. mode B seems to be "swallowed" by mode A: Mode B is not anymore distinguishable as the particle mass distributions are apparently dominated by an excess of mode A. Mode B shows significant higher intensities than mode A only in the low pressure ethylene/oxygen flames and at low equivalence ratios. This could indicate a temperature influence in the formation processes of mode A and B particles.

The soot precursor particles associated with mode A and mode B are characterized by different photo ionization behaviors. Mode A shows an ionization order $n_{mode A} \sim 2$ and a relative low fragmentation threshold around $0.12 MW/cm^2$. Mode B, on the other hand, exhibits an ionization order $n_{mode B} \sim 1$ and a fragmentation threshold around

2.24 MW/cm². This indicates that mode A and B represent soot precursor particles of different structure.

It is demonstrated that soot precursor particles are not only intermediate species found in the flame but also that these particles can survive the flame and be emitted. This is very important since the emission of such small particles from practical systems is commonly not considered. Health effects, however, seem particularly pronounced in the case of very small particles [86]. In addition, it is shown that the rate of particle emission depends on the oxidation processes involved. Mode A particles seem to be more affected by oxidation than mode B particles.

The signals referred to as mode C are interpreted as primary soot particles. Since their behavior in the flame deviates from results obtained by other well-known techniques, it is considered that the detection of particles larger than around 6 nm may constitute the main limitation when applying mass spectrometry. This will be discussed in detail in chapter 8.

7. Engine Exhaust Measurements

The results shown in section 6.1.1 demonstrate that soot precursor particles are not only a transient species in the flame. Rather, soot precursor particles can survive the flame and be emitted. This motivates the investigation whether these particles are emitted from practical combustion devices such as engines.

In this chapter measurements of soot precursor particles by means of TOF-MS in the exhaust gas of two different internal combustion engines are presented. In addition, measurements using a so-called engine exhaust particle sizer (EEPS) are reported.

Conventional diesel engines operate under globally lean burning conditions ($\Phi < 1$). The fuel-mixture in the combustion chamber, however, is heterogeneous. This leads to rich burning regions and consequently to high particle emissions. Common gasoline engines (with throttle body systems or port injection systems¹) operate under slightly rich burning conditions ($\Phi \sim 1$). They are characterized by a fairly homogeneous fuel-mixture and thus by reduced particle emissions.

In this context, it is generally assumed that soot particle emissions are predominantly generated by diesel engines. But, does this imply high soot precursor particle emissions as well? By contrast, soot precursor particles could be eliminated in the presence of soot since soot particles can act as sinks for smaller particles.

Gasoline engines are regarded as clean engines since their soot particle emissions are considered negligible [89]. Would this remain valid for soot precursor particles?

Since a chassis dynamometer is currently not available at our institute, tests on standard factory model vehicles under controlled conditions cannot be carried out. Space limitations as well as the lack of an adequate exhaust extraction system also complicates the realization of the tests. For these reasons, as model devices for diesel and gasoline engines power generators are used.

Two different power generators are tested:

- i) A diesel power generator (Berlan BSTE5000DE) equipped with a diesel fuelled one-cylinder four stroke engine. The nominal electric power output of this generator is 4.2 kW.
- ii) A gasoline power generator (Geko 11 hp) equipped with a gasoline fuelled one-cylinder four stroke engine and a maximal electric power output of 5 kW.

¹Throttle body systems, also known as single-point injection systems, are either the suction driven venturi carburetors or the positive pressure injection. Port injection systems are characterized by a multipoint fuel injection at the inlet ports [95].

Both engines are operated under different conditions ranging from idle to 4 – 5 *kW* load.

First, the exhausts of the diesel and gasoline power generators are analyzed by means of a commercial EEPS (TSI, model 3090). This instrument, based on mobility analysis, has been recently developed for particle emission characterization. Its main ability is to measure particles over a wide size range and in real-time. This allows measurement under transient operation conditions yet reduces the available resolution. The detection limit is higher in comparison to similar instruments like SMPS. The measuring range of the EEPS extends from 5.6 up to 500 *nm*.

For these measurements 5 to 6 *L/min* of exhaust are sampled and immediately diluted. The dilution system consists of three diluters (Dekati, model L7) mounted in series. Each diluter is supplied with approximately 50 *L/min* of compressed air, the latter previously filtered (PALL Compressed Air Filter). About 10 *L/min* of diluted sample are finally supplied to the EEPS.

Some of these measurements, carried out in collaboration with Kanjarkar et al. [60], are presented in figures 7.1 and 7.2. Each figure shows the evolution of the particle mass distribution in the exhaust gas during approximately 1 *min*. The first part of each graph (~ 30 *s*) represents idle conditions. Subsequently the generator is measured under load conditions.

For both engines, it is obvious that the soot production increases with increasing load. Under idle conditions the number concentration of soot particles is relatively small compared with load conditions. As expected, the soot production of the diesel generator is definitively larger than in the case of the gasoline generator. Also the size of the soot particles is larger in the case of the diesel exhaust gas. Soot precursor particles (normally ≤ 5 *nm*) are not detectable because of limitations of the instrument.

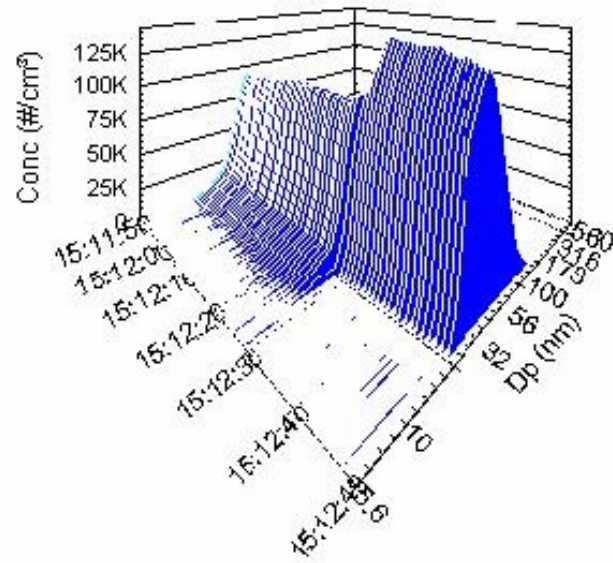


Figure 7.1.: Number concentration and diameter of soot particles measured by EEPS in the exhaust gas of a diesel power generator at idle and 4 kW load operating conditions.

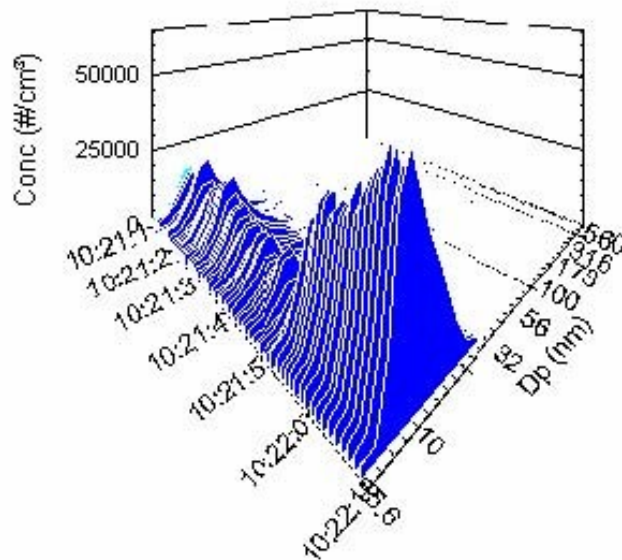


Figure 7.2.: Number concentration and diameter of soot particles measured by EEPS in the exhaust gas of a gasoline power generator at idle and 4 kW load operating conditions.

Both engines are measured by means of time-of-flight mass spectrometry in the same operating range. To this end the sampling system described in previous sections is used. To compensate for the the low sensitivity, slightly higher pressures are allowed in the sampling line ($p_L = 30 \text{ mbar}$). To achieve this the diameter of the nozzle of the probe is increased from 0.8 mm to 1.2 mm . Some of the results are presented below.

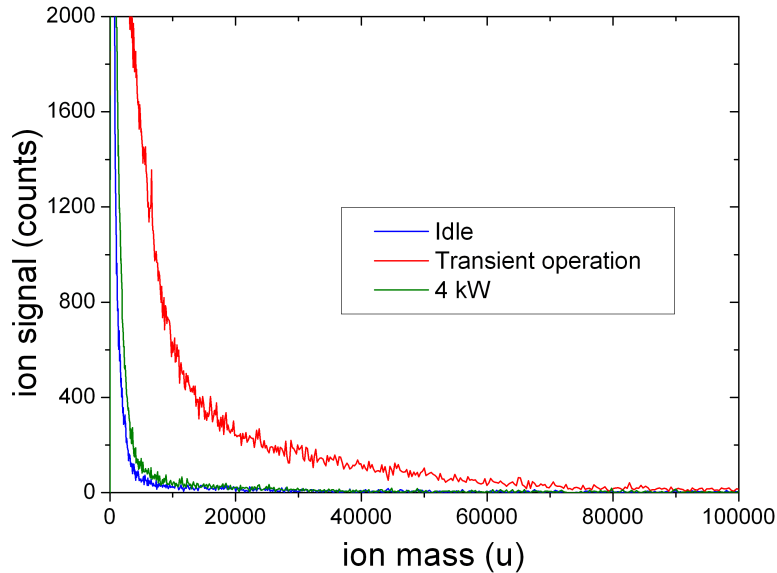


Figure 7.3.: Particle mass spectra of the exhaust gas of a diesel power generator at different operating conditions.

In figure 7.3 the mass spectra measured in the exhaust pipe of the diesel power generator are shown. Under idle and load operation conditions ion signals are detected up to approximately 10000 u . Under transient conditions, i.e. when measuring the transition from idle to load operating conditions, an increase of the signal intensities and masses up to 60000 u are detected. In all cases, very high signal intensities are registered below 500 u . These mass distributions show a steady signal intensity decrease with increasing ion mass while characteristic modes are not observable.

In these measurements soot particles are not observed. From the EEPS measurements it is expected that soot particles are too large ($\sim 32 \text{ nm}$) to be detected by means of TOF-MS.

The exhaust gas of the diesel generator is additionally measured under ionization conditions leading to particle fragmentation. Some of the results are shown in figure 7.4. Fullerene ion signals appear beyond 500 u . This probably indicates indirectly the presence of soot precursor particles as explained in chapter 5. When an engine is started (cold start), higher emissions are expected. This is observed in figure 7.4.

The exhaust gas of the gasoline power generator is also examined under fragmenting and non-fragmentig ionization conditions.

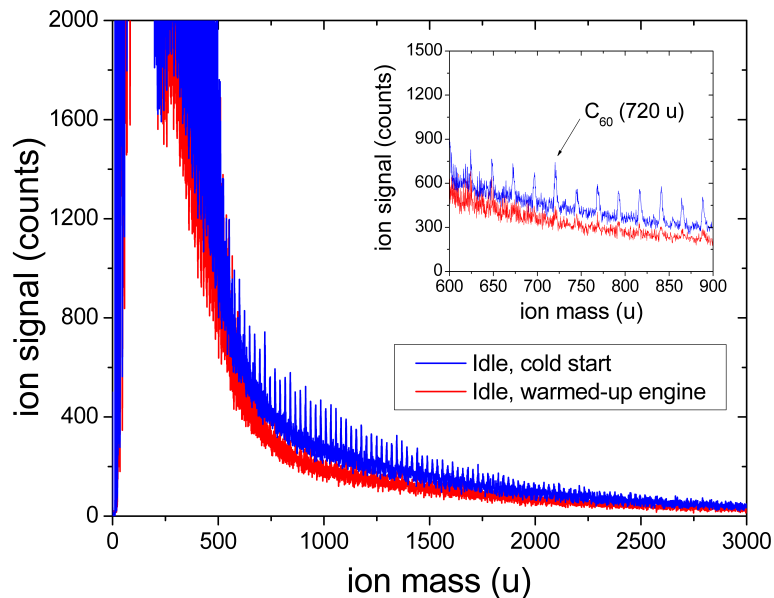


Figure 7.4.: Particle mass spectra of the exhaust gas of a diesel power generator at different operating conditions. Measurements carried out under fragmenting ionization conditions.

The results under non-fragmenting ionization conditions are shown in figure 7.5. At idle operating conditions the mass distribution is characterized by a broad mode ranging from approximately $2000 u$ up to $50000 u$. In terms of particle diameter, it peaks between 3 and $4 nm$ (see section 8.2). When compared to soot precursor particle signals from flames, however, these signals are very low. Under increasing operating load, soot precursor particles signals gradually decrease in the exhaust of the gasoline engine.

The same system is additionally measured under ionization conditions leading to particle fragmentation. These measurements are shown in figure 7.6. Once again fullerene ion signals appear beyond $500 u$. The intensity of these fullerene signals depends on operating load.

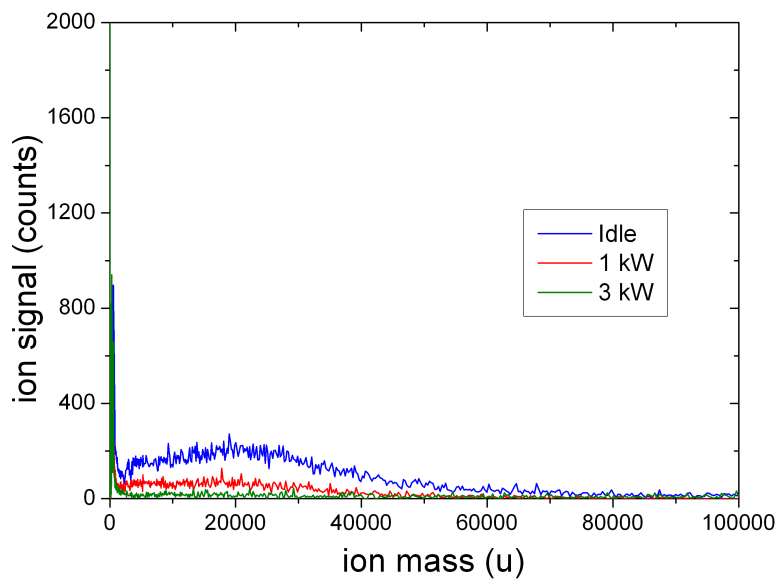


Figure 7.5.: Particle mass spectra of the exhaust gas of a gasoline power generator at different operating conditions.

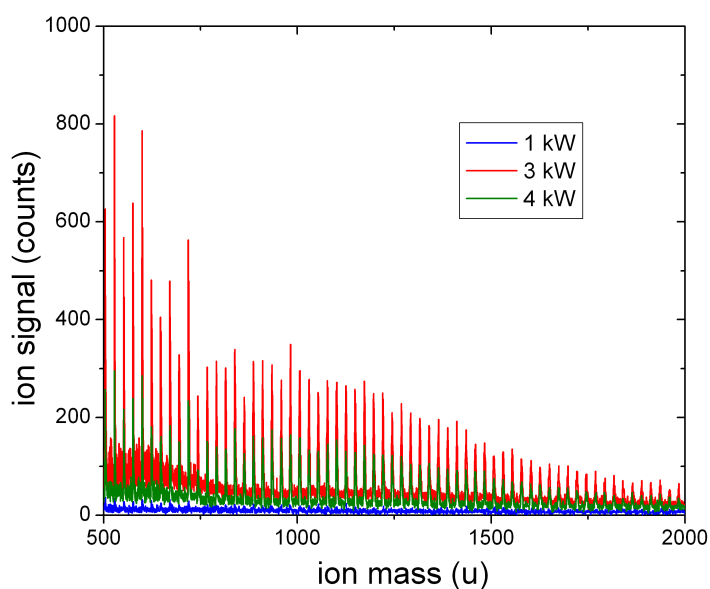


Figure 7.6.: Particle mass spectra of the exhaust gas of a gasoline power generator at different operating conditions. Measurements carried out under fragmenting ionization conditions.

The measurements presented in this chapter represent the first attempt to characterize particulate engine emissions by means of time of flight mass spectrometry. These measurements demonstrate that soot precursor particles smaller than 5 *nm* can be emitted from engines.

In this context, it is obvious that new methods should be applied to evaluate particulate emissions as already suggested by other authors [62]. Not only the total particulate mass but also the number concentration and the particle size should be considered. In addition, not only diesel combustion but also gasoline combustion should be controlled. Parameters like temperature, fuel-mixture homogeneity, fuel composition or operating conditions probably influence the number of soot precursor particles that are formed and emitted.

Due to its high resolution in the low particle size range ($< 5 \text{ nm}$) time of flight mass spectrometry could be advantageous. Higher sensitivities together with measurements under controlled engine operating conditions are necessary to obtain sufficient information concerning the influence of the different parameters on soot precursor particle emissions.

8. Discussion

In the following sections the results obtained via TOF-MS are critically analyzed and compared to published data obtained with other measuring techniques. This demonstrates the advantages and limitations of the use of TOF-MS for the study of soot formation.

Due to the absence of a lower size detection limit and its high resolution, TOF-MS is especially adequate for the detection of soot precursor particles. This allows the monitoring of the soot formation process in its first stages, i.e. when inception occurs and the first particles are formed. Additionally, through the analysis of the photo ionization process, information about the structure of soot precursor particles can be gained. These characteristics, all in one application, makes TOF-MS a very powerful method compared to other techniques that have been traditionally applied to the study of soot formation. The limitations of TOF-MS are mainly its limited sensitivity and an upper size detection limit. As discussed below, a modification of the current experimental set-up, however, could reduce these difficulties.

The measurements presented in this work demonstrate that soot precursor particles can survive the flame and be emitted from laboratory flames and combustion systems. Soot precursor particles are found in significant amounts only at stoichiometries above the soot threshold. Consequently, it is considered that the onset of particle formation takes place at flame stoichiometries close to the soot threshold.

The main message of the present work, however, is that two different types of soot precursor particles can coexist in the flame leading to bimodal soot precursor particle mass distributions. The different particle modes (modes A and B) are characterized by different formation, oxidation, ionization and fragmentation behaviors. One type of soot precursor particles probably consists of PAH stacks while the features of the second type of soot precursor particles indicate a rather amorphous structure. These hypotheses are discussed in detail below.

8.1. Source of Errors of the Mass Spectrometric Measurements

8.1.1. Reproducibility

The reproducibility of the measurements carried out by means of time-of-flight mass spectrometry, as explained in previous chapters, is not always satisfactory.

The general features of the particle mass distributions (number of modes and characteristic maxima) are well reproducible. The fluctuation of the mean particle mass is

below $\pm 10\%$ and thus not very pronounced. Considering $d_p \propto \sqrt[3]{m}$, this relative error of $\pm 10\%$ is reduced to just $\pm 3\%$ in terms of particle diameter.

The overall signal intensity of the mass distributions, however, shows large fluctuations.

Intensity fluctuations are more pronounced in the atmospheric pressure flame than in the low pressure flame: For the atmospheric pressure flame fluctuations up to a factor of 6 are found while for the low pressure flames fluctuations up to a factor 4 are observed. This difference is due to the steep concentration gradients and the higher number of measurement uncertainties that characterizes the atmospheric pressure flame. These measurement uncertainties are caused by slightly different probe positions ($\Delta HAB = \pm 0.5\text{ mm}$) and flame instabilities due to light air drafts. This means that deviations are attributed to an instability of sampling rather than to the MS. In the low pressure flame these effects are reduced since the position of the sampling nozzle is fixed and the flame is enclosed in a housing.

The largest fluctuations (mentioned above) are found at low equivalence ratios, i.e. under measurement conditions close to the detection limit in terms of particle number concentration. This detection limit is a function of the ionization efficiency, the MS transmission (dependent on source geometry and ion optics) and the detection efficiency. Close to this limit, small uncertainties in signal transmission play a major role.

In addition, uncertainties like laser intensity fluctuations (pulse-to-pulse energy stability with $\sigma < 2\%$ [66]) or fluctuations in the unburned gas supply due to the accuracy of the flow controllers certainly contribute to intensity variations.

Other investigated effects are found insignificant:

- i) The progressive internal surface coating of the sampling line leads to a long-term increase of particle wall losses. Consequently, the sampling line is periodically cleaned. For short operating intervals (e.g. a series of measurements) this effect is found to be negligible.
- ii) The influence of temperature fluctuations on the signal processing chain was also investigated. To this end amplifier and comparator were tested at different temperatures. Their function is stable.
- iii) As explained in section 4, the temperature of the sample in the sampling line has an important effect on the signal intensity. Consequently, comparable temperatures between measurements are crucial to assure reproducibility. The arrangement used to cool the sample leads to very similar sample temperatures at the end of the sampling line. For this reason, intensity fluctuations due to temperature fluctuations are considered negligible.

8.1.2. Systematic Errors

The time that ions require from their ionization to their detection is recorded. To this end, the signals coming from the detector during a specified time interval (bin) are recorded and

summed up. These bins are characterized by a constant width that defines the resolution of the measurements.

Using a mass calibration routine, this information is subsequently transformed into ion mass data. The time of flight is proportional to the square root of the mass-to-charge ratio of each ion. Due to this dependency, a systematic error is introduced when transforming the time of flight into ion mass values using a constant bin width.

In the case of low resolution measurements the bin width is fairly wide (e.g. 1024 *ns*). Consequently, a bin comprises several ion masses. The signal intensity per bin results from the addition of all the counts corresponding to all ion masses comprised in the bin. Due to the relation between time of flight and ion mass, for increasing time of flight the number of ion masses per bin will increase. For this reason, given a constant number of counts per ion mass, the apparent signal intensity per bin will increase with increasing time of flight. Since particle mass distributions result from the envelope of the detected mass spectra, this effect leads to a shift of the mean particle mass towards larger masses (see figure 8.1 [46]). Fortunately, when transforming mass distributions into size distribution the same effect concerning the bin widths occurs, yet in the opposite direction. Consequently, relative to time of flight distributions, the systematic error in size distributions is fairly small.

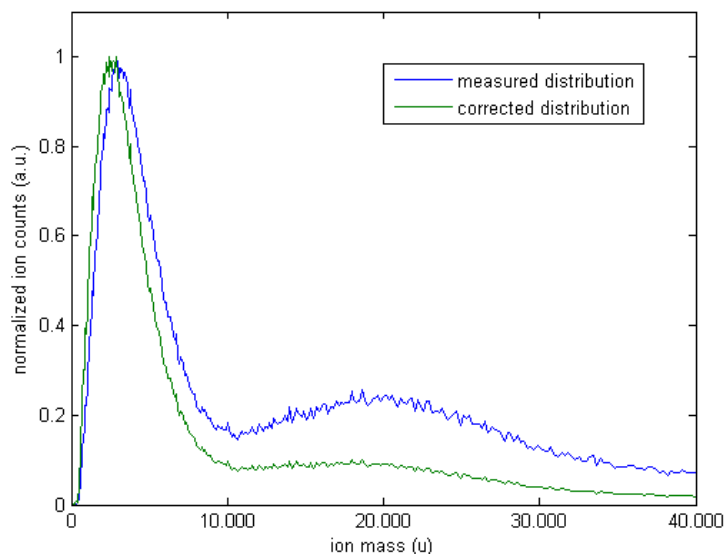


Figure 8.1.: Effect of data recording by means of time bins of constant width on the particle mass distribution. Source of the measured distribution: Premixed ethylene/air flame at atmospheric pressure, $\Phi = 1.85$ and $HAB = 12$ *mm*.

This systematic error leads to an overestimation of the mean particle mass. The extent of this effect depends on the shape of the mass distribution. As displayed in figure 8.1, mode A (narrow distribution) shifts $\sim 30\%$ towards larger masses while mode B (broad distribution) experiences a shift of just $\sim 20\%$. In terms of diameter, as commented above, the relative error is just one third of the relative error in terms of mass. Consequently, the

corresponding relative error in particle diameter is reduced and expected to be $\leq 10\%$. This error is considered small enough to allow the quantitative comparison with other measuring techniques like SMPS, TEM or LII.

Other systematic errors affecting the transformation of mass data into particle diameters are related to uncertainties concerning the density or shape of the particles. In this case, the estimation of this error is complicated since experimental values (and their relative errors) are hardly available.

Another systematic error has to be taken into account when detecting particles larger than approximately 100000 u . This error may lead to an underestimation of the mean particle mass of soot particles as will be explained in section 8.3.

8.2. Particle Size Distributions: Comparison with other Particle Sizing Techniques

The measurements shown previously in section 6.1.1 will now be compared to the results obtained with other measurement techniques, mainly scanning mobility particle sizing (SMPS), transmission electron microscopy (TEM), atomic force microscopy (AFM), small-angle X-ray scattering (SAXS) and laser-induced incandescence (LII). These methods provide information about particle sizes. For this reason, when using TOF-MS an estimation of particle size distributions from the obtained particle mass distributions is required.

An approximation of the particle diameters can be obtained by assuming spherical particles. For this estimation, information about the density of the particles is necessary. According to Dobbins [30], soot precursor particles have a density close to 1.2 g/cm^3 , while carbonaceous soot particles are characterized by a density of 1.8 g/cm^3 . Thus, two different values are used for the calculations: For the low mass range ($< 100000 \text{ u}$), where the ion signals are interpreted as soot precursor particles, $\rho = 1.2 \text{ g/cm}^3$ is used. Above 100000 u $\rho = 1.8 \text{ g/cm}^3$ is considered more adequate.

Using this method the spectra described in section 6.1.1 can be transformed into particle size distributions. From these size distributions, the particle diameters at maximum signal intensity are taken and displayed as mean particle diameters in figure 8.2 for the different particle modes. Due to the low signal intensities of mode C at $\Phi \leq 1.89$ (see figure 6.1) no diameters are given.

In the same way, information about the evolution of the particle diameter along the axis of the flame is obtained from the measurements described in section 6.1.1, as shown in figure 8.3.

Earlier studies on soot formation detected bimodal particle distributions where one mode was associated with soot precursor particles and the second one represented soot

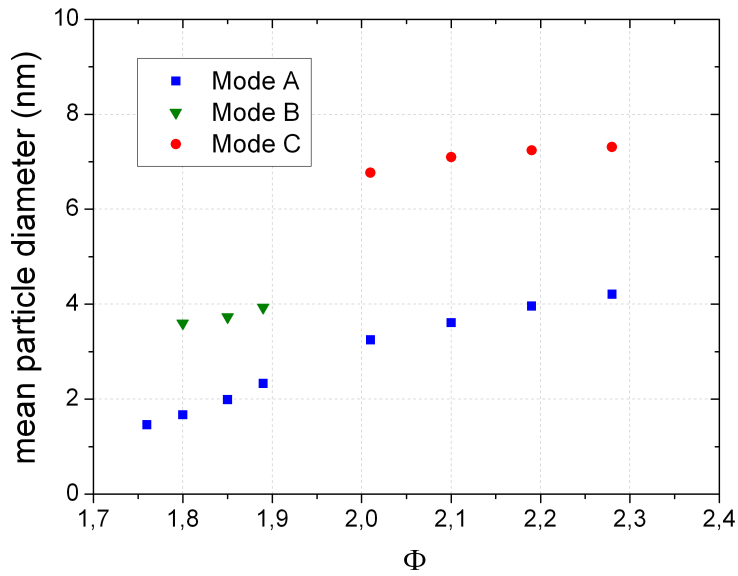


Figure 8.2.: Mean particle diameter at different equivalence ratios in a premixed flame at atmospheric pressure as obtained by means of MS.

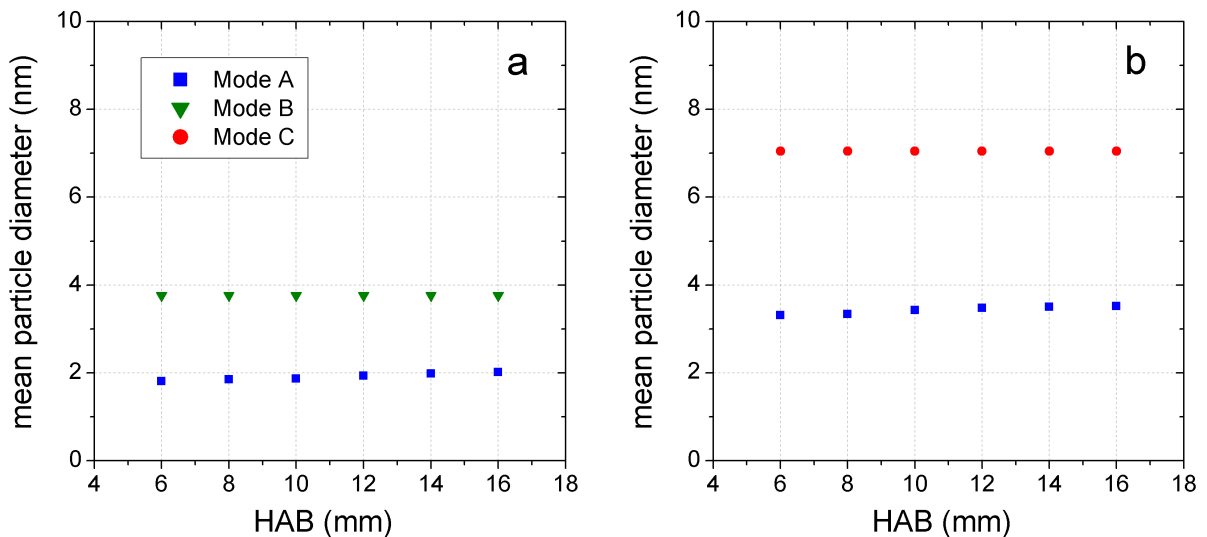


Figure 8.3.: Mean particle diameter at different heights above the burner in a premixed flame at atmospheric pressure as obtained by means of MS. a) $\Phi = 1.85$. b) $\Phi = 2.10$.

particles. In the present study, however, a new feature is found: Soot precursor particles can show a bimodal distribution function.

In figures 8.2 and 8.3 the multi-modal character of the measured mass distributions is clearly shown. Soot precursor particles (modes A and B) exhibit mean diameters ranging from approximately 1 to 5 nm . These particles show a moderate growth with increasing equivalence ratio and a nearly constant size along the flame axis. The primary soot particles associated with mode C are characterized by a diameter of approximately 7 nm which was found to be independent of HAB in the covered range. Similar results for both soot precursor particles and soot particles are obtained for particle size distributions referring to low pressure flames.

Measurements carried out by means of SMPS [74, 93, 113] in comparable flames have shown similar results as the ones described above. In these studies, soot precursor particles, clearly distinguished from soot particles, have been detected. These soot precursor particles show diameters below 5 nm and generally do not grow with height above the burner. Due to the limited measuring range of commercial SMPS (lower detection limit around 3 nm), however, only mono modal soot precursor particle distributions have been detected in most of these studies. Only Sgro et al. [93] measured very recently a structured shape of the nucleation mode by means of a modified SMPS system able to detect particles down to 1 nm .

The presence of soot precursor particles smaller than 5 nm in acetylene/oxygen low pressure flames was already reported in 1973 by Wersborg et al. [111] using TEM. These results have been confirmed in different ethylene flames also by means of TEM [34, 77] as well as AFM [10, 92]. Again in these studies just a mono modal soot precursor particle distribution is described. This could be once again due to the lower detection limit of these methods, around 2 or 3 nm . Additionally, the internal structure of soot precursor particles could make their detection by means of TEM difficult (see section 8.5). Nevertheless, the coexistence of soot precursor particles and soot particles observed by means of mass spectrometry is confirmed by TEM and AFM results.

Recently, SAXS has also been applied to the study of particle formation in premixed ethylene flames [26]. The main advantage of this technique compared with TEM, SMPS or MS is its *in situ* character. This method is characterized by a broad measuring range from 1 to 100 nm . Particle size distributions are obtained by analysis of the measured scattering profiles. This analysis, however, includes several assumptions that may reduce the resolution so that the distinction of different sources for scattering in the lower size range becomes difficult. SAXS measurements found incipient particles along with primary soot particles and aggregates. Once again it is reported that soot precursor particles (~ 1 nm) do not significantly grow with increasing HAB and that they coexist with soot particles.

The main disagreement between the results reported in this work and the SPMS, TEM, AFM and SAXS results is the behavior of soot particles along the flame. According to

figure 8.3 soot particles do apparently not grow with increasing height above the burner. Nevertheless, it is well known that soot particles grow in size along the flame due to coagulation and surface growth as reported in the literature. Additionally, although some recent investigations [26, 74] have demonstrated that primary soot particles can be as small as 5 nm in diameter, larger soot particles are generally detected in the studied stoichiometry range. This discrepancy to the present MS data may arise from

- a) the different experimental conditions that could strongly influence the obtained results or
- b) the limited sensitivity of the applied technique (TOF-MS) at large masses.

In order to exclude the first possibility and to deliver complementary results, measurements under exactly the same experimental conditions as the ones described in section 6.1.1 were carried out in our institute by means of LII. This technique is applied to quantify soot concentrations and soot particle sizes. Its main advantage is that it is a non-intrusive method and consequently does not require a probe or a sampling line. The realization of the measurements as well as the necessary data processing was carried out by Stirn et al. [101]. The calculation of the particle diameters is based on the model put forth by Michelsen [78]. Figure 8.4 shows some of the results.

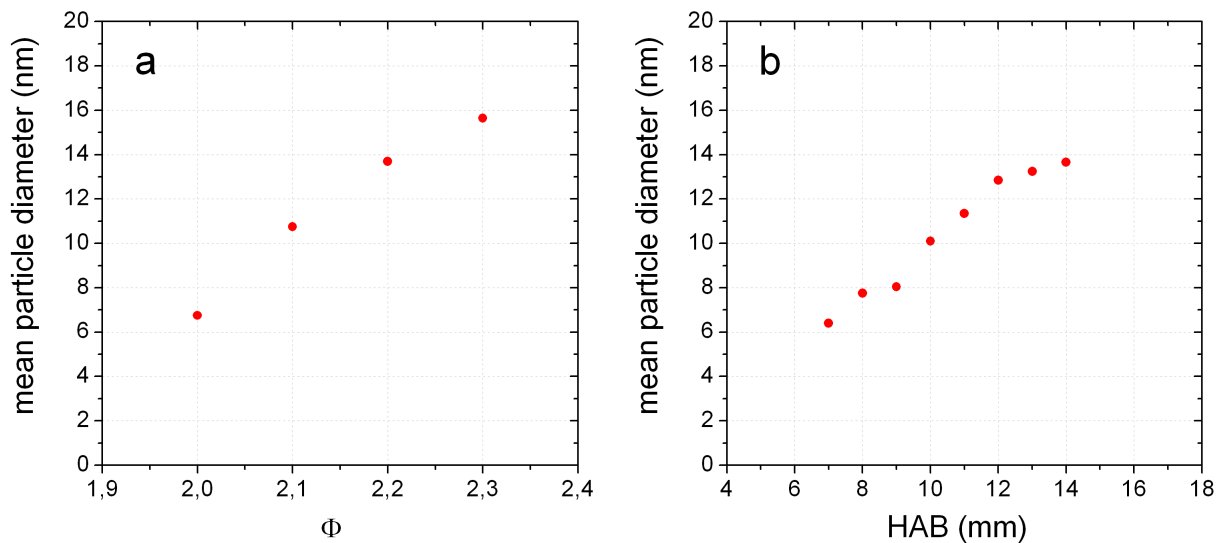


Figure 8.4.: Mean particle diameter data obtained by means of laser induced incandescence in a premixed flame at atmospheric pressure a) at different equivalence ratios and $HAB = 12 \text{ mm}$ and b) at different heights above the burner and $\Phi = 2.10$.

From the analysis of these measurements it is obvious that the discrepancy shown between MS and the other techniques when studying soot particles is not induced by the different experimental conditions. Under similar experimental conditions LII delivers similar results as SMPS, TEM, AFM and SAXS confirming the growth of soot particles with increasing height above the burner and increasing equivalence ratios. Consequently,

soot diameters are underestimated when applying the current TOF-MS set-up. The latter could be related to the decreasing sensitivity that characterizes MCP detectors at increasing ion masses. This problem is treated in detail in the next section.

On the other hand, this last set of measurements shows the advantages of MS compared to LII. In the lower size range (below 5 nm), when the sensitivity of LII tends to be limited, MS delivered reliable data. Additionally, MS is suitable for the monitoring of multi-modal particle distributions. LII signals are always governed by the larger particle mode and consequently the detection of multi-modal particle distributions is not possible.

The agreement of the reported MS measurements with the results obtained by other methods indicates that possible sampling line effects are small enough to allow a good characterization of soot precursor particles in flames by means of time-of-flight mass spectrometry. In addition, the current mass spectrometric set-up provides an especially adequate measuring range for soot precursor particles. The absence of a lower size detection limit is the main advantage of MS.

8.3. Limitation of MS for the Detection of very large Masses

($m > 100000 u$)

In the last section it was demonstrated that the detection of soot particles ($> 100000 u$) by the current set-up is inaccurate. The sensitivity of the whole mass spectrometric method is a function of the ionization efficiency, the MS transmission and the detection efficiency. Ionization of large particles is not considered the limiting effect, since soot particles as large as 250000 u can be ionized. The use of an axial arrangement of the molecular beam inlet system together with optimized operation voltages and pulse lengths should assure a high transmission even for heavy ions. Consequently, the known decreasing detection efficiency of MCP-systems for large ions is probably responsible for the observed upper detection mass limit¹.

The ion detection process by means of microchannel plates (MCPs) includes two important steps [36]:

- The ion-induced electron emission at the detector entrance (primary electron emission)
- The development of amplification cascades along the microchannels of the detector to produce secondary electrons (channel contribution)

The yield of primary electrons by collision of large ions with surfaces has been studied by different authors [14, 43, 75, 115]. The efficiency of this process depends on the impinging ion velocity. Consequently, the detection process becomes more and more difficult with increasing ion mass.

¹In later experiments it was found that a longer acceleration pulse than the one used (10 μs) is more favorable for the extraction of heavy ions [45].

Several authors have reported on a threshold velocity ($\sim 10^4 m/s$) below which the emission of primary electrons drops to zero and consequently no detection is possible [14]. Other authors [43, 115], however, support that the detectability of large clusters is a function of energy per atom and not only a function of the total energy or velocity of the cluster. In this case large ions are still detectable at low velocities.

Since a sharp signal decay by a determined ion mass is not observed in our measurements such a threshold velocity for the emission of secondary electrons is not expected. Rather a loss of detection efficiency following a smooth function is expected above $100000 u$. In addition, considering a threshold velocity around $10^4 m/s$, particles above approximately $20000 u$ would not be detectable at the existing $10 kV$ at the surface of the MCP and this is clearly not the case.

Similar results have been reported by Martin et al. [75] who observed weak signal intensities beyond $100000 u$ for pure $(C_{60})_n$ clusters. In addition, Zimmermann et al. [115] studied the probability of detection of sodium, cesium and lithium clusters as a function of the number of atoms in the cluster for different post-acceleration voltages. A decrease in sensitivity with cluster size was found for all materials. This loss of sensitivity started in the range between 5000 and 8000 atoms and was characterized by an exponential function. Extrapolating to our system by considering carbon atoms, such a drop of the probability of detection could be expected above $\sim 100000 u$. This value and the one above (Martin et al.) are roughly comparable to the observed values. A good estimation of the detection efficiency decrease for soot particles based on such studies is, however, difficult since the yield of primary electrons also depends on parameters like the type of bonding within the ion or the surface target [14, 115].

In this range (large ions and low impinging ion velocities) the detection probability is very sensitive to the energy of the incoming ions. Consequently, increased post-acceleration voltages achieve higher detection efficiencies as shown in the literature. In the current set-up, however, the maximal post-acceleration voltage is limited to approximately $-10 kV$ since it cannot be varied independently from the voltage across the channel plates. Thus the detection efficiency for very large particles could not be improved. In order to achieve higher post-acceleration voltages a different design of the detection system is required. For the detection of large particles the latter should include an extra post-acceleration element (not coupled to the MCP supply) allowing acceleration voltages up to at least $20 kV$.

From the studies above, it is expected that for ion masses below $< 100000 u$ the detection efficiency is nearly independent of the ion mass, i.e. all ions will have enough energy to produce primary electrons. Consequently, the measured particle mass distributions in this mass range are considered real representations of the particles contained in the sample.

8.4. Improvement of the Detection of Soot Precursor Particles

($m < 100000 u$)

The sensitivity of the MS is sufficient to monitor soot precursor particles in and even outside of flames at stoichiometries above the soot threshold. Higher sensitivities, however, would allow an improved investigation of non sooting flames and of real systems such as internal combustion engines. In this context an improved ionization efficiency may be the key to achieve a better sensitivity.

Several modifications of the current set-up were considered to achieve an increase of the ionization efficiency. To this end, alternative ionization methods like PAH enhanced laser ionization or laser-induced chemical ionization were tested (see section 4). An improvement of the sensitivity was not obtained, however, the suitability of photo ionization relative to other methods was confirmed.

Alternative photo ionization methods yielding higher number of photons and consequently an increase of the number of ions available for detection were also considered. The current ionization set-up allows an increase of the photon density in the ion source. However, as shown in section 5, the fragmentation of soot precursor particles requires the laser energy density to be less than $\sim 0.12 MW/cm^2$. The increased number of photons should therefore be realized while increasing the ionization volume or using longer pulse durations, both possibilities not directly available with the current ArF Excimer laser.

An increase of the ionization volume can be accomplished by using an adequate lens. The maximal ionization volume, however, is limited by the dimensions of the ionization source of the MS (i.e. space available between repeller and extraction plates) and the resulting loss of resolution with increasing ionization volume.

The use of an optical pulse stretcher would allow the extension of the laser pulse duration. This method is based upon providing an optical delay circuit comprising a series of beam splitters, beam recombiners and optical reflectors. Along this delay circuit the pulse is divided into several portions which vary in their travel time through the circuit. This possibility, however, is very complicated to accomplish due to geometric constrictions and a very demanding adjustment. Additionally, by no means it is compatible with the requirement of a mobile apparatus. Long laser pulse durations are possible by means of a chopped continuous-wave laser but unfortunately at the expense of photon densities and rather expensive.

In the current work, soot precursor particles are photo ionized by means of an ArF laser at $193 nm$. As explained in section 8.5, first order together with second order ionization processes are observed. The use of an ionizing laser at a shorter wavelength (higher photon energies) could achieve single photon ionization of the particles that require a two step ionization at $193 nm$. This could notably increase their ionization efficiency and consequently the sensitivity of the method. The study of soot precursor particles at different wavelengths would also provide more information about their properties.

For these reasons, the use of a new laser system at a shorter wavelength is considered the most convenient way of improving the method for the detection of soot precursor particles.

8.5. Identification of Modes A and B: Chemical and Physical Composition

The main finding of the present work is the coexistence of different soot precursor particles in flames. For the first time two different types of soot precursor particles have been simultaneously detected in several premixed flames by means of TOF-MS.

In the last decades a great experimental and theoretical progress has been achieved in the understanding of the soot formation processes. The mechanisms leading to soot formation, however, are still discussed in the combustion community. In particular, soot precursor particles, as intermediate species between gas phase species and solid soot particles, are still a controversial issue.

Since the early nineties Dobbins et al. [25, 32, 34] have published abundant experimental studies focused on soot precursor particles. The soot formation process in flames was investigated by means of different transmission electron microscopy techniques. These methods, sensitive to the Bragg diffraction produced by multilayer atomic structures, provide information about the morphology and crystallinity of particles. Soot precursor particles were found to be small polydisperse singlet particles, more transparent to the electron beam than soot particles. Since a coagulative² growth within this class of particles was observed, the term liquid-like material is frequently used to describe these structures. Additionally, it was found that the crystallinity of these liquid-like precursor particles increases through carbonization in high temperature regions. At the same time their growth through aggregation begins. This leads to the well-known soot particle aggregates. Based on complementary laser microprobe mass spectrometric (LMMS) measurements, the crystallinity of these particles was associated with some internal layered arrangement of planar PAHs. Dobbins et al. proposed the thermodynamically favored stabilomer PAHs, as worked out by Stein and Fahr [99], or their isomers as universal path for the formation of soot in flames.

Alternatively D'Alessio et al. [27, 28, 80] studied the soot formation process in flames by means of optical measurements. They carried out light absorption, laser-induced fluorescence and laser light scattering measurements both in the ultraviolet and in the visible. Soot precursor particles were found to be transparent to the visible radiation but absorb in the ultraviolet. The presence of this new class of flame species different from well-known gas-phase components, PAHs and soot particles was confirmed by an absorption

²Coagulation is the process by which particles collide and (like liquids) coalesce, i.e. the original particles are not any more distinguishable and the spherical shape remains. Aggregation is the process by which particles collide but do not coalesce, i.e. particles stick together maintaining their original shape and agglomerates or chains are formed.

and scattering excess in the ultraviolet in different flames. Additionally, soot precursor particles showed a characteristic broadband fluorescence (excited in the ultraviolet) with a maximum around 330 *nm*. These characteristics were found to be compatible with 2-, 3-ring aromatic structures and showed average particle sizes of a few nanometers. These structures are clearly different from the ones described by Dobbins et al. since fully condensed large PAHs (Dobbins particles) are supposed to absorb in the visible. Additionally, D’Alessio et al. found the described soot precursor particles even at stoichiometries below the soot threshold while Dobbins et al. measured soot precursor particles only in rich sooting flames. The formation of soot precursor particles was described by D’Alessio et al. as a fast polymerization process of structural units with no more than 2 or 3 aromatic rings connected by aliphatic and/or oxygen bonds. In this picture soot particles originate from a progressive internal rearrangement of these partially aromatic polymeric structures.

The apparently contradictory experimental evidences about the nature of soot precursor particles are summarized in table 8.1.

Soot precursor particles as described by:	D’Alessio et al.	Dobbins et al.
Detection method	UV-VIS spectrometry (absorption, fluorescence and scattering)	Transmission electron microscopy (Bragg reflections)
Occurrence	In moderately rich flames (below soot threshold) and in rich flames	Only in rich flames above the soot threshold
Features	<ul style="list-style-type: none"> - Transparent in the visible - Strong UV absorption - Water soluble - 2 – 3 <i>nm</i> in diameter - Low coagulation rate 	<ul style="list-style-type: none"> - Transparent to the electron beam - Internal multilayer atomic structure or crystallinity - Diameter < 10<i>nm</i>
Proposed composition and structure	2-, 3-ring aromatic structural units connected by aliphatic bonds without crystallinity	Layers of stabilomer PAHs or their isomers

Table 8.1.: Experimental results on the nature of soot precursor particles as reported by D’Alessio et al. and Dobbins et al.

In this context it must be noted that the layered soot precursor particles described by Dobbins et al. certainly absorb in the visible. Unfortunately, due to the interference caused by soot, these particles are not detectable through the optical methods applied by D’Alessio et al. The soot precursor particles described by D’Alessio et al. are considered amorphous solids and their interaction with the electron beam is expected to be weak. Consequently, the method used by Dobbins et al. (TEM) is probably not sensitive enough to these particles. The size resolution limit of TEM (around 2 or 3 *nm*) could also impede the detection of the small soot precursor particles described by the D’Alessio et al.. For these reasons it seems appropriate to talk about the existence of two different types of soot precursor particles. This assumption is new.

Based on the different experimental evidences about the nature of soot precursor particles, different combustion models have been developed. Most of the soot formation models stress the importance of PAH formation and growth. For instance, Frenklach [37, 38] proposed a high-temperature combustion soot formation model where stable PAH molecules form bound clusters (PAH-dimers, trimers, etc. with layered structure) through sufficiently strong van der Waals forces. Other theories support the formation of networks of aromatic-aliphatic-linked structures [82]. Based on the results obtained by D'Alessio et al., Violi et al. [105, 106] proposed a soot formation mechanism based on the formation of large three dimensional structures without crystallinity. A model combining both approaches, i.e. considering two types of soot precursor particles, is still not available.

Ishiguro et al. [56] presented high-resolution transmission electron microscopy measurements of soot particles. These particles show two structurally different regimes: an amorphous core and an outer shell made of graphitic crystallites. However, it has been suggested only recently that this might be caused by soot precursor particles of different structures: In the studies of Happold et al. [47, 48] carried out by means of TOF-MS in premixed low pressure flames the formation of soot precursor particles by stacking of PAHs has been for the first time measured. The resulting soot precursor particles show a layered PAH structure. These particles, however, are observable just for certain stoichiometries and flame temperatures. When using other flame parameters this type of precursors disappears although soot formation persists. Consequently at least one more soot formation mechanism (and other soot precursor particles) are expected.

In the present work the particle mass distributions detected in the mass range up to 100000 u are interpreted as soot precursor particles with sizes ranging from 1 to 5 nm . The ion signals in this mass range are neither large PAH, nor nano-sized droplets of condensed species. The largest PAHs found in ethylene flames are around 800 u [48] and consequently clearly smaller than the detected soot precursor particles. Nano-sized droplets, as reported in chapter 4.2, would not be stable under the described experimental conditions. The detected signals (modes A and B) show different properties and are considered different types of soot precursor particles. This assumption is noteworthy since, as mentioned above, no other current experimental method has achieved the simultaneous detection and identification of both types of soot precursor particles.

In the measured premixed ethylene/air flames at atmospheric pressure, mode A particles seem to be the dominant species. These particles are found for all the investigated stoichiometries above the soot threshold. For reasons that are not yet clear, mode B particles are only observed in a limited stoichiometric range. In the premixed ethylene/oxygen low pressure flames the role of mode B particles becomes more important. Mode B is in this case dominant in a large stoichiometric range above the soot threshold. Only above a certain equivalence ratio, the nucleation of mode B particles decreases and the particle mass distributions are again apparently dominated by mode A. This reveals that the formation of the particles in each mode is favored under different conditions. The

temperature of the flame, affected by the unburned gas mixture and by the stoichiometry, seems to play an important role. Considering the adiabatic flame temperature as a first approximation of the flame temperature, the temperature of the ethylene/air flame is for the same stoichiometry approximately 1000 K lower than for the ethylene/oxygen flame (see below). In addition, the adiabatic flame temperature decreases with increasing equivalence ratio. Consequently, the formation of mode A particles seem to be favored in low temperature flames while mode B particles dominate in hotter flames. This indicates that mode A and B particles are characterized by different structures.

	Ethylene/Air Flame	Ethylene/Oxygen Flame
$\Phi = 2.0$	1900 K	3000 K
$\Phi = 2.5$	1600 K	2700 K
$\Phi = 3.0$	1400 K	2330 K

Table 8.2.: Calculated adiabatic flame temperatures for different flames [81].

Another important feature distinguishing mode A and B particles is their different ionization orders and fragmentation thresholds. This also leads to the assumption, that mode A and B represent soot precursor particles of different structure.

With increasing solid state character, nonradiative transitions between electronic states increase because of increasing coupling between the states. This leads to a rapid internal dissipation of energy deposited through multiphoton absorption [108]. Consequently, it is expected that the probability of multiphoton ionization processes decreases with increasing internal arrangement such as crystallinity.

For this reason, it is likely that the multiphoton ionization process observed for mode A ($n_{mode\ A} \sim 2$) indicates an amorphous structure (reduced molecular interaction) rather than a highly organized structure. In the same way, it is probable that mode B ($n_{mode\ B} \sim 1$) shows a higher internal arrangement. This arrangement, as explained below, could be based on a layered PAH structure.

Since $n_{mode\ B} \sim 1$, mode B particles are characterized by an ionization energy lower than the energy of an 193 nm photon, i.e. 6.4 eV . This value is lower than the ionization energy of PAHs³. Assuming a layered PAH structure, the ionization energy of the resulting crystallites is expected to be lower than that of the original PAHs due to the interaction between the adjacent molecules [47]. Consequently, it is probable that mode B particles exhibit some internal PAH layered arrangement or crystallinity leading to a decrease of the ionization energy compared to PAHs. This implies a great similarity with the particles described by Dobbins et al.. The higher internal coupling due to crystallinity, leading to a rapid internal dissipation of energy, would explain the relatively high fragmentation threshold of mode B compared to mode A.

These results illustrate that different soot precursor particles are involved in the combustion process. Mode B particles, with their layered PAH structure and favored at

³The ionization energies of PAHs are generally higher than 7 eV [1, 35].

relatively high temperatures, are close to the particles found by Dobbins et al.. Mode A particles, rather amorphous, are the dominant species in low temperature flames and could represent the particles detected by D'Alessio et al..

The features of the detected soot precursor particles are summarized in table 8.3.

	Mode A particles	Mode B particles
Occurrence	Rich sooting flames, predominantly at low temperatures	Rich sooting flames, predominantly at high temperatures
Ionization order	$n_{mode\ A} \sim 2$	$n_{mode\ B} \sim 1$
Fragmentation threshold	$0.12\ MW/cm^2$	$2.24\ MW/cm^2$
Proposed structure	Amorphous structure without crystallinity similar to reported by D'Alessio et al.	Internal PAH layered arrangement similar to proposed by Dobbins et al.

Table 8.3.: Main characteristics of the different soot precursor particles detected in the current work.

The results concerning mode B particles are in good agreement with the measurements reported by Happold [47]. In this work the formation of soot precursor particles by stacking of PAHs is reported for rich low pressure flames in a certain flame temperature range above 2000 K, i.e. at relatively high flame temperatures. For other flame conditions these layered soot precursor particles are not observed although soot is formed. This supports the idea that different soot formation mechanisms, and thus different soot precursor particles, are possible.

D'Alessio et al. reported low coagulation rates of soot precursor particles compared with soot particles in flames. The coagulation rate of soot precursor particles could not be determined in the current work due to the interference of other processes, mainly particle losses in the sampling line due to wall effects and coagulation with soot particles. Although measurements outside flames and in engine exhaust confirm the capacity of soot precursor to survive the flame and be emitted, their coagulation rate was found to be high [87].

Time-of-flight mass spectrometry is a powerful measuring technique for the study of soot formation. The main advantages of this method are its high resolution and the absence of a lower detection limit in terms of particle mass (or size). This is partly offset by the limited sensitivity of the method. The current work experimentally verifies the coexistence of different soot precursor particles in flames for the first time. This should reduce the discrepancies found in the literature and enable a combination of the different models on soot formation. In addition, it has been demonstrated that soot precursor particles are not only intermediate species in a flame. Rather, they can survive the flame and be emitted from combustion systems. Consequently the efforts to avoid the emission of these particles should be continued.

8.6. Lower Φ Limit for Particle Generation

The behavior of soot precursor particles at stoichiometries below the soot threshold is still a disputed issue in the combustion community.

D'Alessio et al. reported number concentrations of soot precursor particles as high as $10^{13} \text{ particle/cm}^3$ in non sooting flames at stoichiometries as "lean" as $\Phi = 1.2$ [27, 28, 80]. No other current experimental method, however, has confirmed the presence of soot precursor particles in non sooting flames at stoichiometries so close to the stoichiometric limit ($\Phi = 1.0$) as reported by D'Alessio et al.. Some authors [104] even discredit this theory. Only very recent DMA measurements [93] detected soot precursor particles in non sooting flames, however, at stoichiometries just below the soot threshold, i.e. under much richer conditions than in the earlier measurements [27, 28, 80].

In the current study all results indicate that the onset of particle formation takes place at flame stoichiometries much closer to the soot threshold (slightly below or even above it) than suggested by D'Alessio et al.. For an overview, figures 8.5 and 8.6 show the mass weighted integrals of the spectra corresponding to the measurements presented in previous chapters for different flames and flame stoichiometries. Since mode A and B particles show different ionization behaviors, different mass spectrometric detection sensitivities are expected. Consequently, the mass weighted integrals corresponding to each particle mode should not be directly compared.

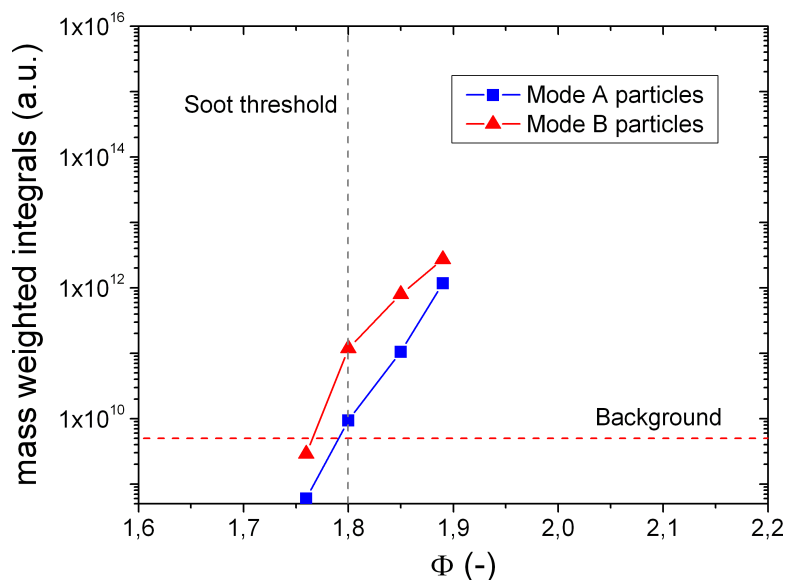


Figure 8.5.: Mass weighted integrals of soot precursor particles for different stoichiometries. Source: Premixed ethylene/air flame at atmospheric pressure.

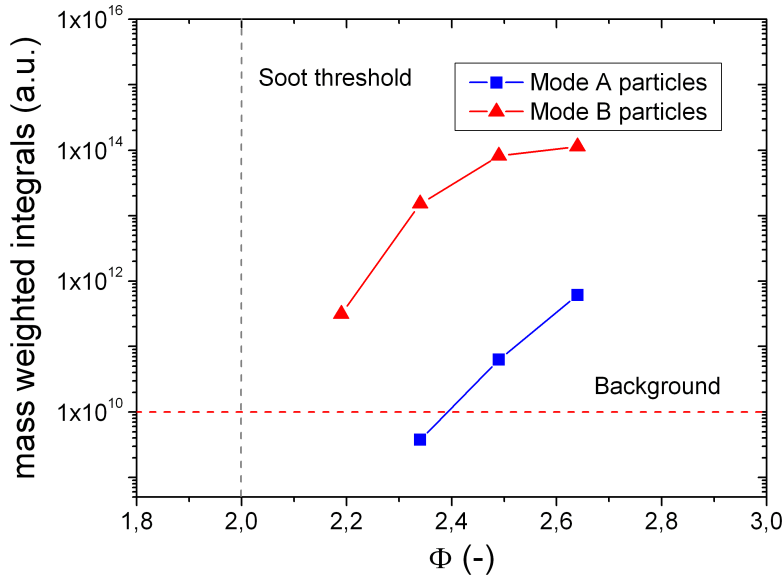


Figure 8.6.: Mass weighted integrals of soot precursor particles for different stoichiometries. Source: Premixed ethylene/oxygen flame at 120 *mbar*.

The evolution of the mass weighted integrals with increasing flame stoichiometry indicates that the onset of particle formation takes place close to the soot threshold. For richer stoichiometries the mass weighted integrals of both mode A and B particle signals show a strong increase by several orders of magnitude. It can be affirmed that significant amounts of soot precursor particles are only formed at stoichiometries above the soot threshold.

D'Alessio et al. also reported rather high concentrations (10^{12} *particle/cm*³) of soot precursor particles in diesel and gasoline engines [92]. In the case of gasoline engine combustion, due to the rather stoichiometric burning conditions ($\Phi \sim 1$) and the homogeneous fuel-mixture, D'Alessio particles are expected to be predominantly or even exclusively formed. The latter not applies in the case of diesel engines. These operate under globally lean burning conditions ($\Phi < 1$), however, due to their heterogeneous fuel-mixture, rich burning regions are also present.

The TOF-MS measurements carried out in the exhaust of both a diesel and a gasoline engine show almost negligible soot precursor particle signals. Only the presence of fullerene signals could indicate the presence of soot precursor particles in the exhaust of both engines under most of the operating conditions. These measurements under ionization conditions leading to particle fragmentation, however, must be carefully interpreted. As explained in chapter 5, fullerenes are probably formed by rearrangement of ion fragments which can originate from mode A soot precursor particles (D'Alessio particles). Consequently, the detection of fullerenes is associated with the presence of these soot precursor particles in the exhaust gas of the investigated engines. Fragmentation due to

excessive laser irradiation, however, can affect both isolated soot precursor particles as well as soot precursor particles adsorbed (coagulated) onto soot particles. Consequently, the emission of soot precursor particles as independent particle class is not satisfactorily demonstrated. Additionally, the formation of fullerenes by, for example, excessive laser irradiation of species arising from unburnt fuel is not excluded.

The detection of soot precursor particles in the exhaust gas of engines by means of TOF-MS could be affected by different factors such as oxidation and coagulation.

As shown in section 6.1.1, mode A particles are easily oxidized. This would influence in particular the emissions from diesel engines due to their operation under an excess of oxygen. Oxidation reduces particle concentration and consequently particle emission in the engine exhaust measurements. Additionally, it affects the size of the surviving particles. For these reasons only ion signals in the range of a few thousand u are expected to be related to oxidized mode A particles. In this mass range ion signals are detected in the case of the diesel engine especially under transient operating conditions.

The ion signals above approximately 10000 u are presumably related to the second type of soot precursor particles (mode B particles) found in flames. These particles are formed under rich sooting conditions. As shown in laboratory flames, mode B particles are apparently more stable against oxidation than mode A particles. Ion signals above 10000 u are observed in the case of the diesel engine only under transient operation. In the case of the gasoline engine a broad particle mass distribution peaking at approximately 20000 u is observed mainly under idling conditions. The mass range of these ion signals overlaps the mass range where mode B particles are found in flames and, after oxidation, outside flames.

The number concentration of soot precursor particles is expected to be affected by their loss due to coagulation with larger particles, i.e. due to coagulation with soot particles. This would influence in particular the emission of soot precursor particles from diesel engines, since the latter are characterized by considerably higher soot particle emissions than gasoline engines.

The non finding of type A particles behind engines by means of TOF-MS could additionally be caused by the observed multiphoton ionization of mode A particles at 193 nm . This probably leads to a low detection efficiency compared to single photon ionization processes. The use of an ionizing laser of a shorter wavelength could achieve a single photon ionization and an increased detection efficiency.

The failure of detection of soot precursor particles in sufficient quantities in gasoline engine exhaust, however, may be explained by the fact that below the soot threshold soot precursor particles are not formed in sufficient quantities or even not formed at all. This interpretation is suggested by the results summarized in figures 8.5 and 8.6. In the case of diesel engines and due to their heterogeneous fuel-mixture, high particle emissions are expected. However, as mentioned above, also negligible soot precursor particle emissions

are detected. This is considered to be related with a decrease in number concentration of soot precursor particles due to oxidation and coagulation with soot.

Appendices

A. Wet Samples of Soot Precursor Particles

When applying mass spectrometry, relative results are obtained because the relationship of the detected ion signal intensity to the particle number concentration in the sample is not known. To achieve quantitative results an external calibration is needed.

Soot precursor particles, such as the polymer-like particles described by D'Alessio et al., were found to be water soluble. Based on this characteristic a method to isolate them was developed by Sgro et al. (see [94] and citations therein). Thierley [103] proposed some modifications of this method and obtained first aqueous solutions of soot precursor particles generated in low pressure premixed flames. These samples were used to calibrate a similar mass spectrometer as the one described in the current work. In addition, the toxicity of these isolated soot precursor particles was investigated.

In the current study the method proposed by Thierley is systematically further developed and used to obtain quantitative information from the mass spectrometric measurements. The applicability of the method is studied using atmospheric pressure premixed flames, low pressure premixed flames and in the exhaust gas of engines (see chapter A.2). The toxicological potential of the obtained aqueous solutions of soot precursor particles is also investigated (see chapter A.3).

A.1. Preparation of Wet Samples for Calibration and Toxicological Analysis

A.1.1. Experimental Set-Up

Soot precursor particles can be isolated by means of a cold trap system (see figure A.1). The latter consists of several impingers connected in series and cooled by means of liquid nitrogen. The impingers are mounted in a "reversed" geometry, i.e. the sample flows in the wash bottles through the short tube and leaves through the long one. This prevents ice formation in the line [103]. The impingers are connected by short silicon tubes.

The sample is drawn from the atmospheric pressure flames and the engine exhaust pipes through the nozzle of a quartz glass probe. To this end a DESAGA pump (GS312) is used. This unit allows the automatic adjustment of the flow using pumping speeds ranging from 0.2 to 12 *L/min*. It records sample volume and sampling duration. The average flow rate during the measurements is calculated from these parameters with an accuracy of $\pm 2\%$.

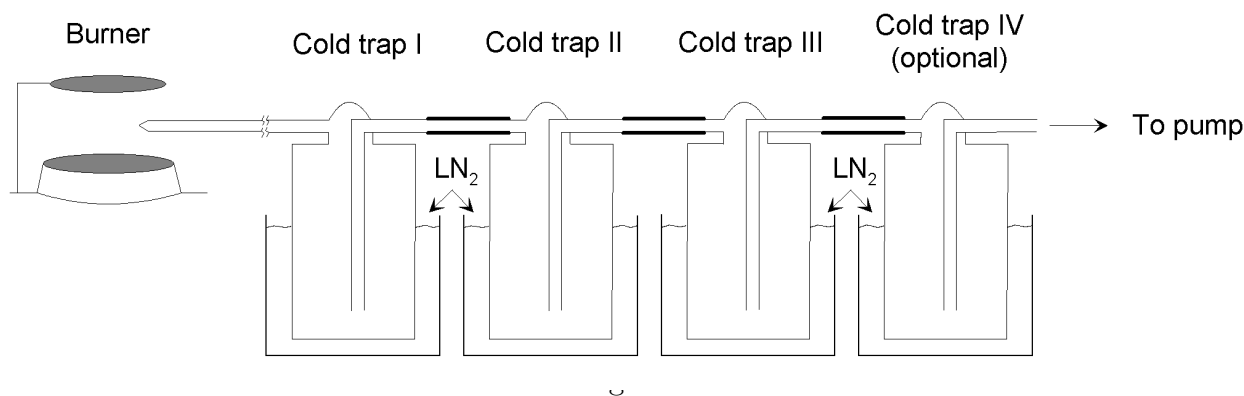


Figure A.1.: Cold trap set-up.

In the case of the low pressure flames, the cold trap system is coupled to the burner by means of a steel tube placed just below the skimmer integrated in the housing of the burner (see page 36). The DESAGA pump is not appropriate to sample under low pressure conditions. For this reason, in this case the gas sample is drawn by means of a Pfeiffer rotary vane pump (type DUO 1.5 A). The flow rate and sample volume are measured with a gas meter (J. Braun & Co. GmbH) and an accuracy of $\pm 0.5\%$. The flow rate can be roughly controlled by manually throttling the pump. This method, however, is very imprecise and thus the adjustment of the flow was not attempted during the measurements. Prior to each series of measurements, a flow rate is selected and the pump adequately throttled. This configuration is then maintained for the whole set of measurements. The stability of the flow is checked with the gas meter at the beginning and at the end of each measurement. Increasing combustion chamber pressures indicate the clogging of the nozzle and consequently the reduction of the sample flow. In such cases the sampling procedure is immediately stopped. This results in slightly reduced gas sample volumes but constant sample flow rates. As explained in the next section, constant gas flow rates are needed to assure comparable collection efficiencies.

After dewing the aerosol sample, a few *mL* of aqueous solution are found in each wash bottle. This liquid sample is then recovered, diluted and filtered. To this end two different paper filters were used:

- i) Roth paper filter (Rotilabo circular filter, type 115A, diameter = 70 mm) with a pore size of $2.5\mu\text{m}$ and made of 100% cellulose. This filter is characterized by a very low filtration rate.
- ii) Macherey-Nagel filter (type MN 85/70, diameter = 70 mm) with a retention down to $0.6\mu\text{m}$ and made of borosilicate glass fibers and organic binder. It allows a high filtration rate.

The amount of total organic carbon (TOC) in the filtered aqueous solutions is determined by means of a Rosemount high temperature TOC analyzer (DC-190). The measuring range of this analyzer extends from 1 to 2000 *ppm C*. The correct operation of the apparatus was checked through frequent calibrations.

A.1.2. Detailed Sampling Procedure and Parametric Study

The sampling procedure consists of several steps:

a) Cleaning of impingers and silicone tubes

A careful cleaning and drying procedure assures a reasonable reproducibility of the measurements since outliers are eliminated and background interference is reduced.

To this end each impinger is first washed with a detergent (scrubbing powder) and abundantly rinsed with water. After several wash-ups with acetone, the impingers are finally dried with compressed air. The silicone tubes are only treated with compressed air.

b) Gas sample drawing

Two parameters define the sample drawing conditions: Gas flow rate and gas sample volume.

The efficiency of the cold trap system depends on the gas flow rate as shown below. For this reason, a standard flow rate is necessary to obtain comparable samples from different flames.

The gas sample volume can also be varied. High sample volumes accumulate high amounts of soot precursor particles. This reduces relative errors due to, for example, contamination in the impingers. However, it also increases the sampling duration. Under rich flame conditions the sampling duration is limited due to the clogging of the nozzle of the probe for both the atmospheric and the low pressure flame. For these reasons an optimal gas sample volume for the flame stoichiometries under study had to be found. The resulting value ranges from 8 to 10 *L*.

c) Recovery of the aqueous solution

Once the sample drawing is finished, a frozen residue (combustion water) is observed in each of the wash bottles. Since particles are expected to stick to the wall of the cold trap, the latter is carefully washed-up with a few *mL* distilled water. Each of the resulting aqueous solutions (one per impinger) is then poured in a 5 *mL* measuring beaker.

d) Dilution of the liquid sample

To simplify calculations and to avoid the need of measuring each recovered volume, the obtained aqueous solutions are slightly diluted to achieve a total volume of 5 *mL*. This also makes the effect of the filtration step comparable, as explained below.

e) Filtration and TOC analysis

In most the cases soot particles are observable in the first impinger. This leads to turbid aqueous solutions. To avoid the alteration of the TOC results by the presence of soot particles, the solutions are routinely filtered. After filtration the turbidity of the solutions disappears and thus the presence of soot particles is considered negligible.

The used filters contain organic components especially in the binders. The influence of these organic components on the obtained TOC values is studied by means of regularly blank sample tests: After analyzing each of the aqueous solutions (one per impinger) obtained in a sampling procedure, a blank sample (5 mL of distilled water) is analyzed. This blank sample is then filtered and analyzed once again. Distilled water shows negligible TOC concentrations. After filtration, however, the TOC content clearly increases. When using the Roth filter $11 \mu\text{g/mL C} \pm 23 \%$ are found on average in the filtered water. In the case of the Macherey-Nagel filter $30 \mu\text{g/mL C} \pm 12 \%$ are detected.

For calibration purposes the filter interference is taken into account. This effect is of little importance when sampling under very rich conditions since the amount of soot precursor particles is very high in comparison to the filter interference. In the case of low soot precursor particle concentrations (e.g. close to the soot threshold), however, the filter interference can lead to an erroneous interpretation of the results. For this reason, the TOC results must be corrected. To this end the average filter contribution is subtracted from the TOC values found in each cold trap. When this filter interference is considered, the TOC values are labeled as "corrected".

The filter interference is also taken into account when studying the toxicological potential of the aqueous solutions. To this end blank samples of filtered distilled water were additionally analyzed.

As commented above, after filtration each sample is analyzed by means of the TOC analyzer. The TOC values shown in the next sections are in each case the averages of two consecutive analyses of the same wet sample. These analyses are characterized by an excellent reproducibility.

The whole sampling procedure and analysis lasts approximately 3 hours.

The influence of the gas flow rate on the efficiency of the method is studied. To this end several samples are drawn from two premixed ethylene/air flames ($\Phi = 1.9$ and 2.2 , $HAB = 12\text{mm}$, Burner II) at flow rates ranging from 0.4 to 2.0 L/min . In every case 4 cold traps are connected in series and the gas sample volume is 9 L . For $\Phi = 2.2$, sampling at flow rates above 1.3 L/min is not possible due to the increasing pressure drop along the sampling line and due to the partial clogging of the nozzle of the probe. Sampling flow rates below 0.4 L/min are also not available due the operating range of the pump. For the filtration step the Roth paper filter is used. In order to study the reproducibility of the results, the whole sampling procedure is repeated twice for some of the sampling conditions.

The mass concentration of organic carbon found in each of the resulting wet samples is shown in table A.1 and table A.2 . The highest TOC concentration values are found in the wet samples collected in the first cold trap. Furthermore, the concentrations found in the cold traps III and IV are very close to the TOC values caused by filter interference

($\sim 11 \mu\text{g}/\text{mL C}$). The latter is taken into account when calculating the total "corrected" TOC mass. This parameter represents the total amount of organic carbon trapped in a sampling procedure. It results from the addition of the organic carbon mass found in each of the final aqueous solutions. This is calculated from the concentration values associated to each wet sample and the corresponding wet sample volume (5 mL). Additionally, the filter interference is considered, i.e. the average filter contribution is subtracted.

Average flow rate (L/min)	Cold trap I TOC ($\mu\text{g}/\text{mL}$)	Cold trap II TOC ($\mu\text{g}/\text{mL}$)	Cold trap III TOC ($\mu\text{g}/\text{mL}$)	Cold trap IV TOC ($\mu\text{g}/\text{mL}$)	Total "corrected" TOC mass (μg)
0.5	75	21	18	19	442
0.5	72	18	18	15	398
1.2	44	28	14	15	288
1.9	41	17	11	10	181
2.0	39	20	13	13	207

Table A.1.: Results of TOC analysis for different sampling flow rates. Source: Ethylene/air premixed flame at $\Phi = 1.9$ (Burner II). Filter interference $\sim 11 \mu\text{g}/\text{mL C}$

Average flow rate (L/min)	Cold trap I TOC ($\mu\text{g}/\text{mL}$)	Cold trap II TOC ($\mu\text{g}/\text{mL}$)	Cold trap III TOC ($\mu\text{g}/\text{mL}$)	Cold trap IV TOC ($\mu\text{g}/\text{mL}$)	Total "corrected" TOC (μg)
0.4	132	32	17	11	741
0.4	107	19	18	19	598
0.8	122	19	17	13	643
1.3	107	30	17	15	632
1.3	65	26	16	21	421

Table A.2.: Results of TOC analysis for different sampling flow rates. Source: Ethylene/air premixed flame at $\Phi = 2.2$ (Burner II). Filter interference $\sim 11 \mu\text{g}/\text{mL C}$

Figure A.2 reports the total "corrected" TOC mass as a function of the sampling flow rate for both flames. The efficiency of the system clearly decreases with increasing sampling flow rate. These results suggest three conclusions:

- Similar sampling flow rates are a prerequisite to obtain comparable efficiencies and thus comparable measurements.
- Low sampling flow rates assure the highest efficiency of the concentration method.
- The reproducibility of the results is reasonably good.

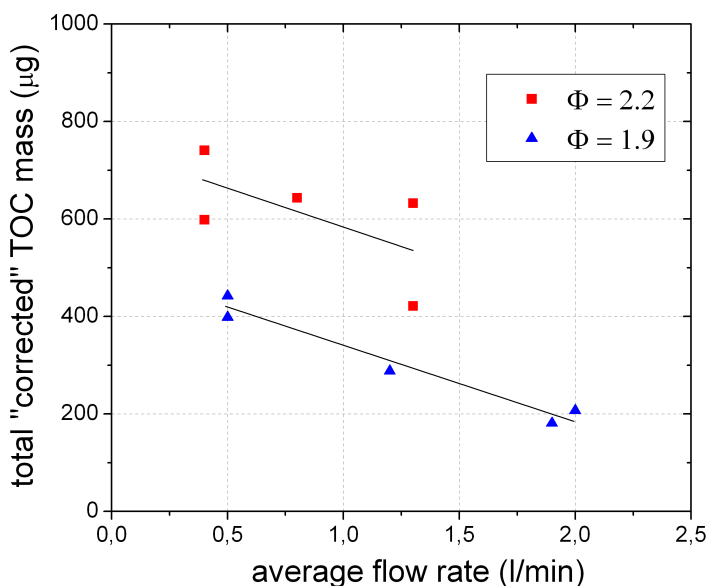


Figure A.2.: Collecting efficiency of the cold trap system as a function of the sampling flow rate. Source: Ethylene/air premixed flame (Burner II).

A.2. Calibration

A.2.1. Method

A calibration method based on the TOC analysis of wet samples is employed to attempt the quantification of the soot precursor particles detected by means of TOF-MS.

The aqueous solutions obtained from laboratory flames and engine exhaust as described in chapter A.1 are considered concentrated samples of soot precursor particles. Since other flame species like PAHs are characterized by low water solubilities, their presence in these aqueous solutions is expected to be minor. Aldehydes, also found in flames, are soluble in water. These species, however, are formed in relative low concentrations in the flame and thus they are not expected to contribute significantly to the collected wet samples. These hypotheses are confirmed by complementary high performance liquid chromatography (HPLC) measurements. These analyses detect traces of PAHs (mainly naphthalene and

phenol) and aldehydes (mainly benzaldehyd). The concentration of these species, however, is very low and thus negligible.

For calibration purposes, the collecting efficiency of the cold trap system must be high. To this end low sampling flow rates together with a cold trap system consisting of at least 3 impingers connected in series are necessary. In such a case it is assumed that nearly all soot precursor particles are trapped in the system. By flushing the impingers with water, the water soluble polymer-like particles described by D'Alessio and associated to the detected mode A particles are considered to be efficiently isolated [94].

Under these conditions the mass concentration of soot precursor particles (C) in the flame is given by

$$C = \frac{M_{TOC} \cdot T_N}{V_{Sample\ gas} \cdot T_{Flame}} \quad (A.1)$$

where M_{TOC} is the total "corrected" TOC mass, $V_{Gas\ sample}$ the gas sample volume under normal conditions, T_N the temperature at normal conditions and T_{Flame} the flame temperature.

The number concentration of soot precursor particles (N) in the flame can be approximated by

$$N = \frac{M_{TOC} \cdot T_N}{V_{Gas\ sample} \cdot T_{Flame} \cdot M} \quad (A.2)$$

where M is the mean soot precursor particle mass. The latter is obtained from the corresponding mass spectrometric measurements. M is calculated from the mean particle mass of the soot precursor particle distribution in atomic units (m) by means of the Avogadro's constant. Consequently

$$N = \frac{M_{TOC} \cdot T_N \cdot N_A}{V_{Gas\ sample} \cdot T_{Flame} \cdot m} \quad (A.3)$$

A.2.2. Results

In this section the applicability of the method described above is studied for different flames and also for the case of engine exhaust gas.

Since this calibration method is based on the water solubility of the so-called D'Alessio particles, the proposed method is especially adequate for those flames where the latter are the dominant species. This applies in the case of the investigated premixed flames at atmospheric pressure.

An estimation of the number concentration of soot precursor particles for two different ethylene/air flames at atmospheric pressure is presented in table A.3. The total "corrected" TOC mass is the average of the measurements reported in chapter A.1 (page 106) for the lowest sampling flow rates. The mean particle mass of the soot precursor particle

distribution is obtained from the corresponding mass spectra shown in figures B.2 and B.1 (shortest sampling line). The adiabatic flame temperature, calculated using [81], is used to approximate the flame temperature.

Φ (-)	Gas sample volume (L)	Total "corrected" TOC mass (μg)	Particle atomic mass (u)	Adiabatic flame temperature (K)	Particle number concentration ($particle/cm^3$)
1.9	9	420	5800	1960	$6.4 \cdot 10^{11}$
2.2	9	670	21000	1800	$3.1 \cdot 10^{11}$

Table A.3.: Number concentration of soot precursor particles in two different ethylene/air flames at atmospheric pressure ($HAB = 12\text{ mm}$, Burner II).

Minutolo et al. [80] applied optical methods to detect soot precursor particles in similar flames. They predicted number concentrations as high as $10^{13}\text{ particle}/\text{cm}^3$ in flame regions where soot had not yet been formed, i.e. low in the flame. The number concentration of soot precursor particles decreases strongly after the onset of soot formation and it is expected to get closer to the values presented above. Maricq [74] measured soot precursor particle number concentrations close to $10^{10}\text{ particles}/\text{cm}^3$ over most of the height range of similar flames using a differential mobility analyzer (DMA). The discrepancies between the different experimental techniques demonstrate the complexity of the monitoring of the inception process. As discussed in chapter 8, the optical methods applied by D'Alessio et al. (including Minutolo et al.) seem to overestimate the amount of soot precursor particles at stoichiometries below the soot threshold. Consequently also an overestimation is expected at higher stoichiometries and low in the flame, when soot is still not present. After the onset of soot formation, this method is no longer applicable. On the other hand, measurements carried out by means of DMA may underestimate the concentration of soot precursor particles due to its lower size detection limit. The number concentration of soot precursor particles is considered in any case one or two orders of magnitude higher than the soot particle number concentration.

The estimation of the number concentration of soot precursor particles, however, is not always possible with the method described above. As shown in previous chapters, most of the investigated laboratory flames are characterized by a bimodal distribution of soot precursor particles. This is associated with the existence of two different types of soot precursor particles: Mode A and B particles. In such a case, the total particle mass associated to each mode must be determined and then related to the corresponding mean particle mass of each soot precursor particle mode (m). As explained above, the calibration method is based on the water solubility of mode A particles and thus not adequate for the isolation of mode B particles. The latter, associated with the more aromatic particles described by Dobbins et al., are considered not soluble in water.

Additionally, since mode A and B particles show different ionization behaviors, different mass spectrometric detection sensitivities are expected. Consequently, the quantitative information obtained for mode A particles can not be easily extrapolated to determine the mass or number concentration of the detected mode B particles.

An estimation of the mass concentration of mode A soot precursor particles for an ethylene/oxygen flame at 120 *mbar* and different stoichiometries is presented in table A.5.

To this end wet samples of soot precursor particles are collected as described in chapter A.1. The results of the corresponding TOC analysis are shown in table A.4. In this case the collecting system consists of 3 cold traps mounted in series. For all flame stoichiometries the sampling gas flow rate is kept low, i.e. at 0.4 *L/min*. This assured a comparable sampling efficiency. At $\Phi = 2.79$ and due to the clogging of the skimmer, the sampling procedure is interrupted prematurely. This results in a reduced sampled gas volume. In this series of measurements the Macherey-Nagel filter was used. The corresponding particle mass spectra (bimodal) obtained by means of TOF-MS are represented in figure 6.14, page 73.

Φ (-)	Sampled gas volume (<i>L</i>)	Cold trap I TOC ($\mu\text{g}/\text{mL}$)	Cold trap II TOC ($\mu\text{g}/\text{mL}$)	Cold trap III TOC ($\mu\text{g}/\text{mL}$)	Total "corrected" TOC mass (μg)
1.65	10	35	58	46	251
1.89	10	164	69	40	920
2.04	10	144	55	65	875
2.19	10	214	105	41	1355
2.34	10	273	98	80	1813
2.49	10	376	122	56	2321
2.64	10	465	167	70	3067
2.79	8	799	187	100	4985

Table A.4.: Results of TOC analysis for different Φ . Source: Ethylene/oxygen premixed flame at 120 *mbar*. Filter interference $\sim 30 \mu\text{g}/\text{mL}$.

The estimated soot precursor particle mass concentration is represented in figure A.3 as a function of the flame stoichiometry. The evolution of the mass concentrations seems to confirm the presence of soot precursor particles slightly below the soot threshold, as reported by Alessio et al. (see chapter 8). However, when estimating soot precursor particles mass concentrations from wet samples, the related signal to noise ratio decreases for decreasing stoichiometries. Consequently, in the low stoichiometric range the associated measuring error can be high. For this flame and by means of TOF-MS, soot precursor particles could only be detected above the soot threshold (see page 73). For flame stoichiometries above the soot threshold, increasing particle mass concentrations are observed. This increase, however, is not so pronounced as expected from the corresponding mass spectrometric measurements (see section 8.6). This indicates a possible limitation of the calibration method, since the concentration of soot precursor particles seems to be

Φ (-)	Adiabatic flame temperature (K)	Particle mass concentration ($\mu\text{g}/\text{cm}^3$)
1.65	3165	2.2
1.89	3072	8.2
2.04	2998	8.0
2.19	2912	12.3
2.34	2818	17.6
2.49	2718	23.3
2.64	2610	32.1
2.79	2497	68.1

Table A.5.: Mass concentration of soot precursor particles in an ethylene/oxygen flame at 120 mbar as a function of Φ . Filter interference $\sim 30 \mu\text{g}/\text{mL}$.

underestimated for very rich conditions.

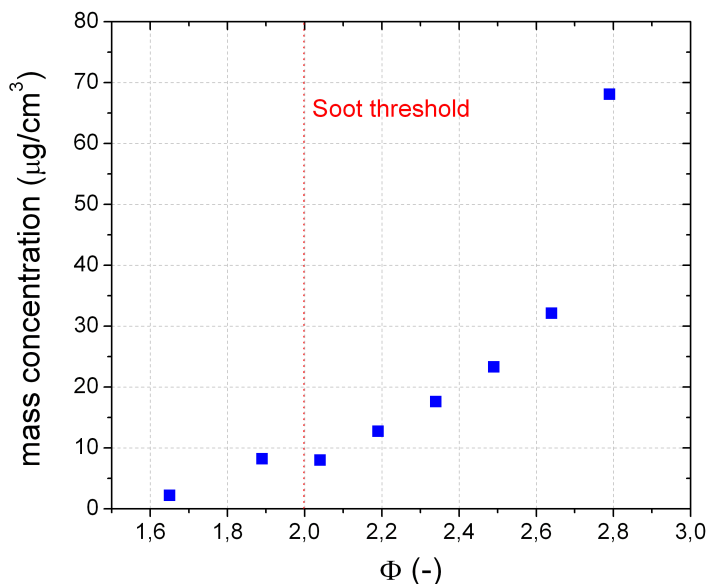


Figure A.3.: Estimated soot precursor particle mass concentration as a function of the flame stoichiometry. Source: Ethylene/oxygen flame at 120 mbar.

The estimation of the number concentration of soot precursor particles in engine exhaust is also attempted. The applicability of the method, however, is questionable.

Wet samples of soot precursor particles are obtained for diesel and gasoline exhaust. The collecting system consists on 3 cold traps mounted in series. The sampling gas flow rate is kept at $0.4 \text{ L}/\text{min}$. In the case of the diesel engine the Macherey-Nagel filter is used for the filtration step. The Roth paper filter is used in the case of the gasoline exhaust. Some of the results are shown in tables A.6 and A.7.

Especially for the diesel engine, high amounts of organic carbon are found. In addition, the corresponding HPLC analysis shows negligible contents of known PAHs and aldehydes.

Operating conditions	Sampled gas volume	Average flow rate	Cold trap I TOC	Cold trap II TOC	Cold trap III TOC	Total "corrected" TOC mass
(-)	(L)	(L/min)	($\mu\text{g/mL}$)	($\mu\text{g/mL}$)	($\mu\text{g/mL}$)	(μg)
Idle	10	0.4	1175	88	37	6059
Load (4 kW)	10	0.4	451	69	33	2324

Table A.6.: Results of TOC analysis for different operating conditions of the diesel engine. Filter interference $\sim 30 \mu\text{g/mL}$.

Operating conditions	Sampled gas volume	Average flow rate	Cold trap I TOC	Cold trap II TOC	Cold trap III TOC	Total "corrected" TOC mass
(-)	(L)	(L/min)	($\mu\text{g/mL}$)	($\mu\text{g/mL}$)	($\mu\text{g/mL}$)	(μg)
Idle	9	0.4	139	17	27	762
Load (4 kW)	9	0.4	194	21	28	1053

Table A.7.: Results of TOC analysis for different operating conditions of the gasoline engine. Filter interference $\sim 11 \mu\text{g/mL}$

For these reasons, high concentrations of soot precursor particles are expected. However, as shown in chapter 7, only in the case of the gasoline engine under idle conditions a well defined soot precursor particle distribution is observed. This indicates a lack of correlation between observed soot precursor particle distributions and obtained TOC values.

A major difference in the diesel and gasoline combustion relative to laboratory flames is the complex composition of the fuel. In addition, a well-known problem of engine combustion is the incomplete combustion of fuel components. For this reason both pyrogenic and perogenic (i.e. arising from unburnt fuel) species are found in engine exhaust [31]. Some of these species may be water soluble organic compounds or simply interfering low volatiles. This may explain the high concentration of organic carbon found in the wet samples, apparently not correlated to the amount of soot precursor particles in the exhaust. The measurements carried out by means of TOF-MS (see chapter 7) also confirms the presence of high amounts of low mass components ($< 500 u$) in the engine exhaust. This background hampers the estimation of the number (or mass) concentration of precursor particles by means of TOC analysis in the case of engine exhaust samples.

A.3. Toxicological Analysis

A.3.1. Method

The toxicological potential of combustion generated soot precursor particles was evaluated by means of biological methods. To this end the bacterial SWITCH test, developed by Baumstark-Khan et al. [11, 13], was applied. This test is a combination of two bioassays that simultaneously measure the genotoxicity (SOS-Lux test) and the cytotoxicity (LAC-

Fluoro test). This combined method is fast, sensitive and reproducible, showing a broad band of applications in environmental research.

In the SOS-Lux test the genotoxic potential of the sample is quantified by an increased bioluminescence in the genetically modified bacteria *Salmonella typhimurium*. These bacteria contain a series of associated genes, which depend on the DNA repair system. The so-called reporter gen, originally isolated from the *Photobacterium leiognathi*, leads to enhanced light production in the presence of DNA damaging agents. The emitted bioluminescence indicates the activation of the DNA repair system and it is proportional to the activity of the genotoxic agent. In addition, this bioluminescence reporter system monitors the kinetics of the DNA repair process: During incubation in the presence of a genotoxic agent and after a delay phase, bioluminescence increases indicating the damaging of the DNA in the bacteria and the activation of the repair system. If the cells succeed in repairing the altered DNA the light production decreases to the normal value again. A decrease of bioluminescence during incubation, however, can also be a result of cell decease due to, for instance, cytotoxic substances. For this reason, a complementary toxicological test must be carried out.

The cytotoxic potential of the sample is quantified by a decreased fluorescence in the LAC-Fluoro test. Since a gen for the expression of green fluorescent protein, originally isolated from the jellyfish *Aequoria victoria*, is included in the original bacteria, the latter are fluorescent under normal conditions. If the cellular metabolism of the bacteria is disturbed by the action of cytotoxic components, the protein synthesis is altered and the fluorescence decreases.

The described recombinant *Salmonella typhimurium* cells are incubated under controlled conditions. The resulting bacterial culture is added to each well of a microplate already containing diluted wet samples of the combustion generated soot precursor particles on study. This microplate is immediately placed into a reader (EG&G Wallac Multilabel Counter, type 1420 Victor2) under controlled temperature conditions. After excitation at 405 nm luminescence and fluorescence at 510 nm are periodically measured during approximately 8 hours of incubation. The absorbance of the bacterial suspension at 490 nm is additionally measured. This parameter reflects the bacterial cell mass production. Consequently, it can also be a measure of the cytotoxic potential of a test substance. For each sample concentration at least three replicate measurements and one background measurement are carried out. Additionally, control samples of untreated bacterial cultures are measured. This is necessary since the number of cells may vary during incubation and hence the related luminescence, fluorescence and absorbance. A more detailed description of the performance of the SWITCH test can be found in the literature mentioned above.

The genotoxic potential of each sample is evaluated by means of the relative luminescence (Lux_{rel}). The latter is calculated according to equation A.4 on the basis of background-corrected data for peak luminescence outputs of the cultures treated with the

test samples (Lux_i) and the untreated bacterial cultures (Lux_0).

$$Lux_{rel} = \frac{Lux_i}{Lux_0} \quad (\text{A.4})$$

In the same way, the relative fluorescence (Flu_{rel}) and the relative absorbance (Abs_{rel}) are calculated as a measure of the cytotoxic potential. Flu_{rel} is given by equation A.5 and considers background-corrected fluorescence data of the the cultures treated with the samples (Flu_i) and untreated cultures (Flu_0) measured after 6 hours of incubation.

$$Flu_{rel} = \frac{Flu_i}{Flu_0} \quad (\text{A.5})$$

Abs_{rel} is calculated according to equation A.6. Analogously, it considers background-corrected fluorescence data of the cultures treated with the samples (Abs_i) and the untreated cultures (Abs_0) measured after 6 hours of incubation.

$$Abs_{rel} = \frac{Abs_i}{Abs_0} \quad (\text{A.6})$$

The luminescence response induction factor F_i is given by equation A.7. This factor corrects the light emission data for cell concentration effects considering relative absorbance data. This correction for concentration is necessary because cytotoxic substances may delay or impair cell growth and consequently influence the total light emission of the culture.

$$F_i = \frac{Lux_{rel}}{Abs_{rel}} \quad (\text{A.7})$$

A substance is considered to be genotoxic, if F_i reaches a value of 2 or more. Additionally, a relative fluorescence of less than 0.5 is considered the threshold for a sample to be cytotoxic. It indicates that half of the bacteria have died.

A.3.2. Results

The bacterial SWITCH test is used for the biological assessment of the geno- and cytotoxicity of concentrated wet samples of combustion generated soot precursor particles. These wet samples are obtained as described in chapter A.1 from different flames and also from engine exhaust gases. The results of these biological tests, carried out by Baumstark-Khan et al. [12], are presented below.

Figure A.4 shows the dose-response curves of the bacterial SWITCH test for the wet samples obtained from an ethylene/oxygen premixed flame at 120 *mbar* and stoichiometries ranging from $\Phi = 1.65$ to $\Phi = 2.79$. The experimental conditions for the collection of these wet samples and the results of the corresponding TOC analyses are summarized in chapter A.2. The wet samples collected in the first cold trap are used for the biological

test. From each wet sample of soot precursor particles a series with different degrees of dilution is prepared. The genetically modified bacteria are exposed to these diluted samples allowing the detection of the concentration range in which the original samples are toxic. The concentrations given in figure A.4 are final concentrations in the SWITCH test. They result from the multiplication of the original TOC values found in the samples and the applied dilution ratios¹. For all flame stoichiometries the evolution of the dose-response curves is quite similar. For clarity, just a few examples are shown.

In figure A.4 a the relative luminescence of the sample is shown. This parameter is a measure of the genotoxicity of the sample. For low concentrations, the bioluminescence of the bacterial culture treated with the different samples is similar to that of the untreated culture. Consequently, the calculated relative luminescence is close to 1 and genotoxicity is not observed. For concentrations above $\sim 10 \mu\text{g}/\text{mL}$ a steep increase of the relative luminescence is observed. This indicates that deleterious changes in the genetic material of the treated bacteria have activated their repair system. Consequently, their luminescence is stronger than the luminescence of the untreated culture. The greatest genotoxicity is observed in the concentration range between 20 and 50 $\mu\text{g}/\text{mL}$. For concentrations above these values, a strong cytotoxic reaction leads to a steep decrease of the relative luminescence for increasing concentrations. Due to the break down of the cellular metabolism, the DNA repair system fails and the luminescence decreases. The cytotoxic reaction even induces cell death. The latter leads to relative bioluminescence values below 1.

The cytotoxicity of the different samples is assessed from both the relative fluorescence and the relative absorbance. The evolution of these parameters for increasing sample concentrations is represented in figure A.4 b and figure A.4 c, respectively. For low concentrations, both the relative fluorescence and the relative absorbance are close to 1. This indicates that the samples are not cytotoxic within the given concentration range. Above $\sim 10 \mu\text{g}/\text{mL}$, however, both dose-response curves suffer a steep decrease. The fluorescence and the absorbance of the bacterial culture treated with the test samples is clearly lower than those of the untreated culture. This is due to the altered metabolic activity of the bacteria and the decreasing bacterial growth caused by a strong cytotoxic reaction. Relative fluorescence values close to zero indicate that the bacteria are dead.

As commented in chapter A.1, the filters used during the preparation of the concentrated wet samples of soot precursor particles contain water soluble organic components. These are responsible for the so-called filter interference. In order to avoid an erroneous interpretation of the toxicological analyses, the geno- and cytotoxicity of these components was also studied. To this end the SWITCH test was also applied to blank samples of filtered distilled water. The results are included in figure A.4. For all concentrations the relative luminescence, the relative fluorescence and the relative absorbance remain roughly constant and close to 1. Consequently, it can be concluded that these components are neither genotoxic nor cytotoxic in the given concentration range.

¹The dilution ratio is equal to the initial volume of the solution divided by the final volume.

In the obtained wet samples, small amounts of PAHs and aldehydes were detected by means of HPLC (see chapter A.2). These substances are potentially toxic. In the detected concentrations, however, neither geno- nor cytotoxic effects are observed.

The results presented below indicate that for all studied flame stoichiometries the resulting wet samples induce both genotoxic and cytotoxic reactions. For this series of measurements the thresholds for genotoxicity and cytotoxicity are reached in any case and for similar final concentrations in the SWITCH test. $F_i > 2$ is obtained for concentrations close to $30 \mu\text{g}/\text{mL}$ while $Flu_{rel} < 0.5$ is reached for concentrations close to $50 \mu\text{g}/\text{mL}$.

Considering the original TOC values found in the samples and the different degrees of dilution applied during the SWITCH test, an increasing toxic potential is observed for increasing original TOC values and thus increasing soot precursor particle concentrations.

However, since even the wet sample corresponding to a flame stoichiometry of $\Phi = 1.65$, clearly under the soot threshold where soot precursor particles are not formed in significant amounts, induces toxic reactions, soot precursor particles may not be the only toxic substance in the samples.

The different fractions constituting these wet samples, i.e. aldehydes, PAHs, soot precursor particles, etc., could probably be isolated by means of size exclusion chromatography. Such a pre-separation would then allow a better investigation of the toxic potential of each fraction.

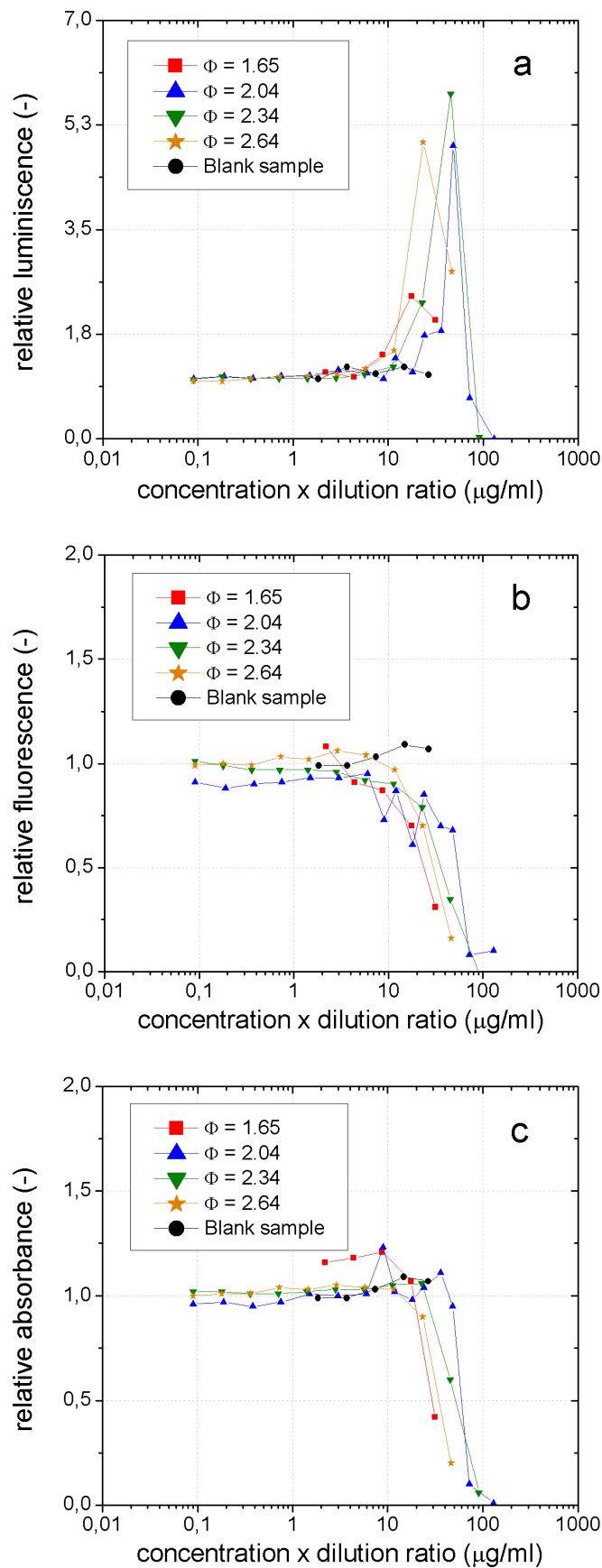


Figure A.4.: Dose-response curves of the bacterial SWITCH test for wet samples of soot precursor particles (cold trap I) obtained from an ethylene/oxygen premixed flame at 120 mbar and different burning stoichiometries (Φ). a) Relative luminescence. b) Relative fluorescence. c) Relative absorbance.

The same SWITCH test described above is carried out for wet samples obtained from a diesel engine. The experimental conditions for the collection of these wet samples and the results of the corresponding TOC analyses are described in chapter A.2. The wet samples resulting from the first cold trap are used for the biological test. The corresponding dose-response curves of the bacterial SWITCH test are presented in figure A.5. Once again the given concentrations are final concentrations in the SWITCH test.

In figure A.5a the steep increase of the relative luminescence for concentrations above approximately $5 \mu\text{g}/\text{mL}$ is a clear indication of the genotoxic effect of these wet samples.

The evolution of the dose-response curves for the relative fluorescence and the relative absorbance (figures A.5b and A.5c) demonstrates that these samples are also cytotoxic. The threshold for genotoxicity ($F_i > 2$) is reached for concentrations ranging from 10 to $15 \mu\text{g}/\text{mL}$. The threshold for cytotoxicity ($Lux_{rel} < 0.5$) is reached at slightly higher concentrations between 20 to $25 \mu\text{g}/\text{mL}$.

These results, however, must be carefully interpreted. As explained in chapter A.2, the amount of organic carbon found in these wet samples is not correlated with the observed soot precursor particle distributions. For this reason, the observed genotoxic and cytotoxic effects may not be related solely to the presence of soot precursor particles. It is expected that other species of pyrogenic and/or perogenic origin are present in the wet samples. These substances could contribute to the observed genotoxic and cytotoxic reactions. Once again a pre-separation of the different fractions constituting the samples by for instance size exclusion chromatography would be recommendable.

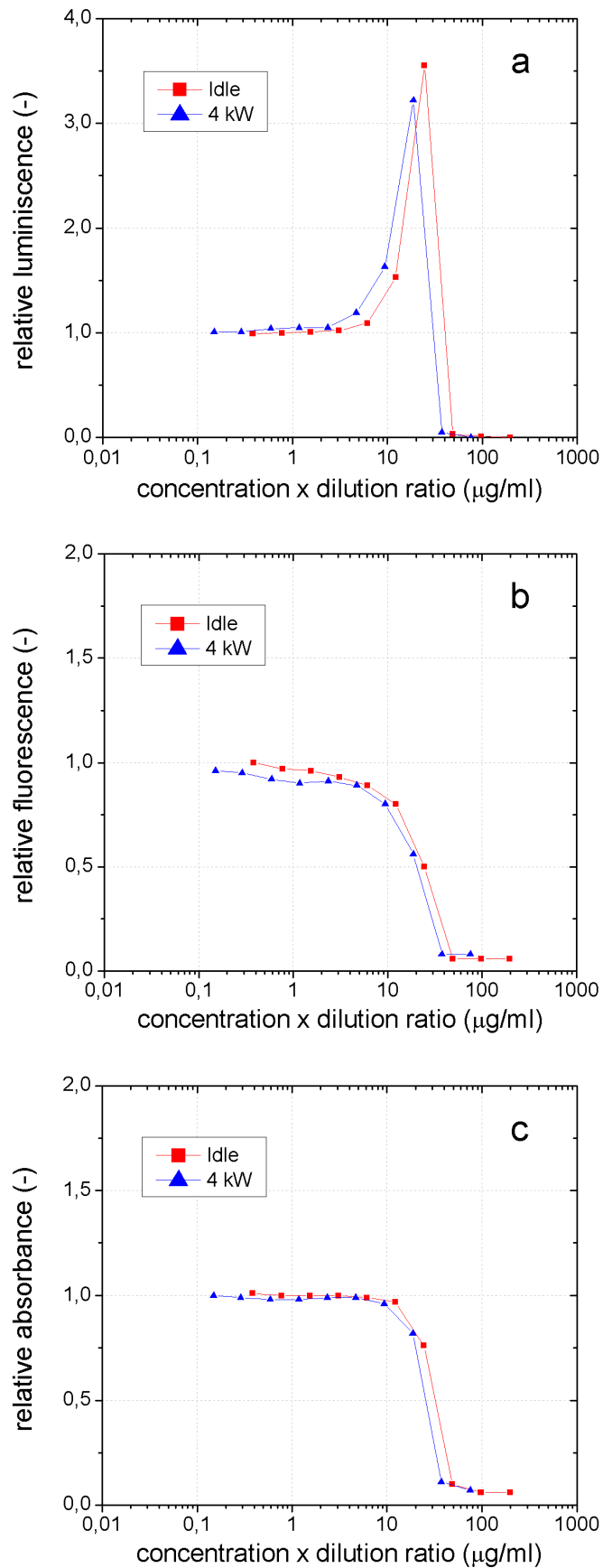


Figure A.5.: Dose-response curves of the bacterial SWITCH test for wet samples of soot precursor particles (cold trap I) obtained from a diesel engine at different operating conditions. a) Relative luminescence. b) Relative fluorescence. c) Relative absorbance.

B. Other Sampling Line Effects

B.1. Influence of the Residence Time

The coagulation behavior of soot precursor particles is of particular importance. It implies a possible change in the measured mass distributions but, in addition, it is of relevance for the emission probability of soot precursor particles. D'Alessio et al. [29, 80, 92] have calculated very low coagulation coefficients for soot precursor particles in flames. This matches their prediction of high emission rates of these particles into the atmosphere.

For this reason it is interesting to study the coagulation behavior of soot precursor particles in the sampling line. This can be done for example by varying the residence time of the sample in the sampling line. With increasing residence time and due to coagulation among soot precursor particles, a decrease in particle number concentration together with an increase in particle size is expected. Unfortunately, coagulation is not the only process taking place in such a set-up. Particle wall losses and coagulation with soot particles also decrease the number concentration of soot precursor particles, while adsorption of PAHs onto the existing particles affects their size. Coagulation can not be isolated from these other processes and consequently the coagulation coefficient of soot precursor particles is very difficult to estimate.

Particle losses originate due to the interaction between the particles and the wall. This effect is important provided that the sticking coefficient¹ is large (sticking coefficient ~ 1). In this case, as described in the next section, the process is controlled by transport, i.e. by diffusion and thermophoresis. The resulting losses are called diffusion and thermophoretic losses. They are large when dealing with particles smaller than 10 *nm* in diameter.

The number concentration of soot precursor particles is also affected by their loss due to coagulation with larger particles, i.e. due to polydisperse coagulation with soot. Due to geometrical reasons, this coagulation is faster as coagulation between particles of the same size. Consequently, large particles act as sinks for the rapid collection of small ones [53]. This is important in the case of real systems (e.g. exhaust pipe) because the emission probability of soot precursor particles will strongly depend on soot concentration even if the coagulation among soot precursor particles is very slow.

The increase of soot particle diameters due to surface growth through addition of small units (e.g. PAHs) has been reported elsewhere for rich flames. This process, although not explicitly reported for soot precursor particles in the flame, is also predicted by some

¹The sticking coefficient is defined as the ratio between the rate at which particles strike the wall and the rate of adsorption of particles on the wall.

models [82]. At high temperatures (in the flame) such a particle growth occurs due to the formation of new chemical bonds. Under sampling line conditions (lower temperatures) PAHs adhere to the particle surface rather due to intermolecular weak interactions like van der Waals forces.

Adsorption of PAHs onto the existing particles could be reduced or even eliminated by using a thermodenuder. These devices heat the aerosol sample up to 300°C and volatilize organic components adsorbed onto the particles. The heater is followed by a denuder where gases are removed onto active charcoal. The whole system, however, suffers from increased diffusion losses for small particles ($d_p \leq 10 \text{ nm}$). Consequently, the detection efficiency of soot precursor particles is hampered and the coagulation process still affected.

The combined effect of coagulation, particle losses and particle growth due to adsorption of PAHs can be observed in the measurements presented in figures B.1 and B.2. The influence of the residence time of the sample in the sampling line is investigated in two ethylene/air flames ($\Phi = 1.9$ and 2.2 , Burner II) at atmospheric pressure. These flames are measured under variable residence time conditions by drawing samples through a sampling line of variable length consisting of several quartz glass tube pieces ($d_i = 6 \text{ mm}$). In all cases, one 50 cm segment of the sampling line is cooled (see section 4.2). The smallest sampling line length is 90 cm .

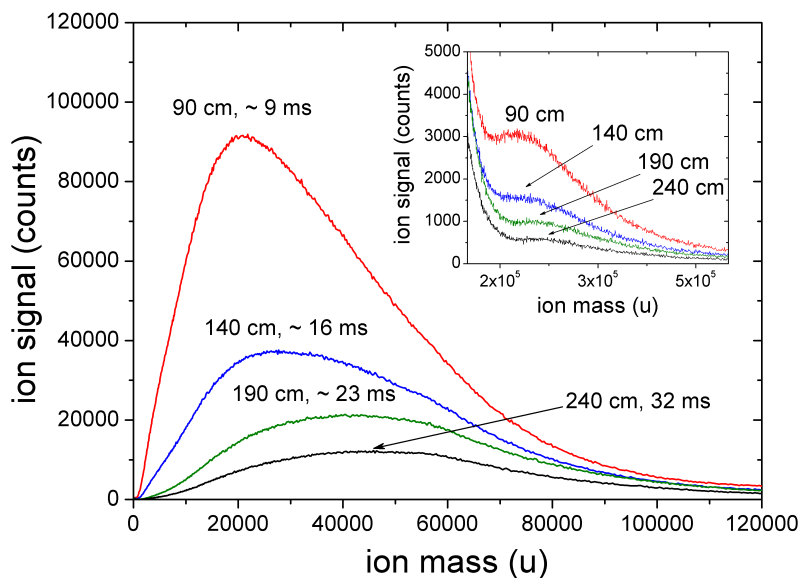


Figure B.1.: Evolution of soot precursor particle and primary soot particle profiles in a sampling line of variable length. Source is an ethylene/air flame ($\Phi = 2.2$) at atmospheric pressure. The length of the sampling line and the corresponding calculated residence times are indicated.

The indicated residence times are calculated for the corresponding sampling line lengths as explained in section 4.1. The initial temperature of the sample is again assumed to be the adiabatic flame temperature of the corresponding flame ($T_{Flame} = 1800 \text{ K}$ at

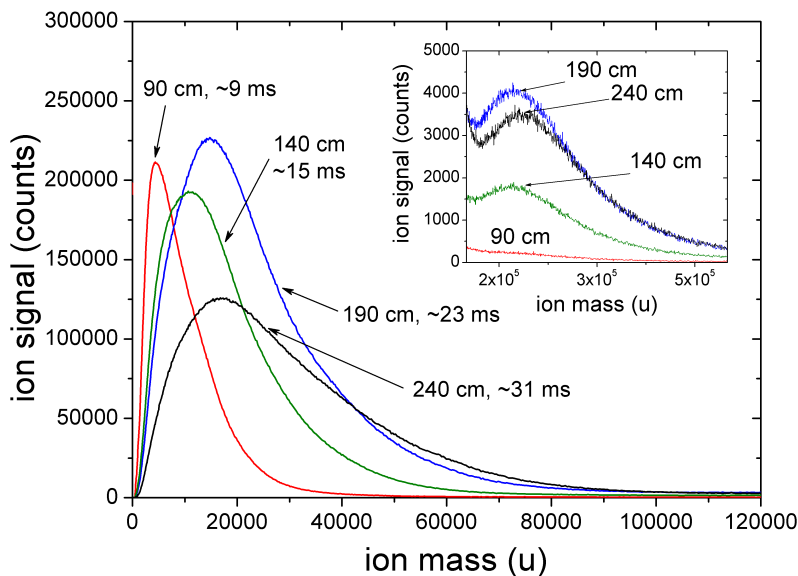


Figure B.2.: Evolution of soot precursor particle and primary soot particle profiles in a sampling line of variable length. Source is an ethylene/air flame ($\Phi = 1.9$) at atmospheric pressure. The length of the sampling line and the corresponding residence times are indicated. The represented curves are averages of several measurements.

$\Phi = 2.2$ and $T_{Flame} = 1960\text{ K}$ at $\Phi = 1.9$) calculated with [81]. The resulting flow rates of 2.47 L/min and 2.37 L/min (by standard conditions) respectively are in good agreement with the measured flows downstream of the sampling line forepump ($\sim 2.25\text{ L/min}$).

It must be noted that the increasing length of the sampling line produces an increase in the pressure drop along the sampling line. The pumping speed is sufficient to assure identical pressure conditions at the valve entrance of the MS and thus identical molecular beam conditions. The pressure at the probe tip, however, depends on the total tube length: When comparing the shortest and the longest sample line, the pressure at the tip of the probe (p_0) increases by a factor ~ 1.5 . This affects the expansion rate of the sample through the nozzle of the probe leading to an increase of the concentration at $x = 0$ of approximately 30%. Therefore, not only the residence time of the sample in the sampling line increases with the sampling line length, but also the concentration at its tip.

Figure B.1 shows the evolution of the soot precursor particle mass distributions with increasing sampling line length. A decrease in signal intensity with increasing residence time can be observed. This is interpreted as a particle number concentration decrease due to coagulation and particle wall losses. As commented above, soot precursor particles are expected to undergo selfreactions as well as reactions with soot particles. A shift of the mass distributions towards larger masses is additionally observed with increasing residence time. This is the consequence of two effects: Coagulation and particle growth due to adsorption of PAHs.

In figure B.2 a similar evolution of the signal intensities is found yet obscured by a

poorer reproducibility. This may be related to the fact that the sensitivity of the system is adapted to each series of measurements according to the experimental conditions (different Φ). For $\Phi = 1.9$ the MCP voltage of the MS is at its highest limit and hence at its detection limit where uncertainties in the signal transmission could play a major role. The change in amplifier setting prevents a direct comparison of the signal intensities (y-axis-scale) of both series of measurements.

Due to the described sampling line effects, changes of the mass distributions are expected even for short sampling lines. Nevertheless, these changes are considered to be small enough to assure a good characterization of soot precursor particles in flames by means of time-of-flight mass spectrometry (see chapter 8). In the examples shown above changes in particle diameter below 2 nm are observed.

B.2. Particle Losses

B.2.1. General Considerations

The particle number concentration of an aerosol can be affected by different particle loss mechanisms during the transport along a sampling line. These mechanisms are considered in the following. Provided that the sticking coefficient of the particles is close to 1 (see page 121), the relevant processes leading to particle losses are diffusion and thermophoresis for the particle size range on study ($d_p \leq 10 \text{ nm}$) [53, 51].

The transport of particles due to a concentration gradient is called diffusion. When an aerosol flows along a sampling line such a concentration gradient is established in the region near the wall of the line as the aerosol particles collide and then adhere to it. The diffusion of aerosol particles to the walls of a tube with circular cross section in a fully developed laminar flow can be calculated as a function of the dimensionless deposition parameter μ [53],

$$\mu = \frac{DL}{\dot{V}} \quad (\text{B.1})$$

where D is the diffusion coefficient of the particles, L the length of the tube and \dot{V} the volumetric flow rate through the tube.

Equation B.2, yields the penetration P (fraction of entering particles that exit) as a function of μ with an accuracy of 1% for all values of μ .

$$\begin{aligned} P &= \frac{N_{out}}{N_{in}} = 1 - 5.50 \mu^{2/3} + 3.77 \mu \quad \text{for } \mu < 0.009 \\ P &= 0.819 \exp(-11.5 \mu) + 0.0975 \exp(-70.1 \mu) \quad \text{for } \mu \geq 0.009 \end{aligned} \quad (\text{B.2})$$

where N is the particle number concentration.

Thus, the diffusive fractional loss can be calculated as follows:

$$\text{Diffusive Fractional Loss} = \frac{N_{in} - N_{out}}{N_{in}} = 1 - P \quad (\text{B.3})$$

The diffusion coefficient (D), necessary for the calculation of the deposition parameter (μ), can be expressed as

$$D = \frac{kTC_c}{3\pi\eta d_p} \quad (\text{B.4})$$

where k is the Boltzmann's constant, T the absolute temperature, C_c the slip correction factor, η the dynamic viscosity and d_p the particle diameter.

While the dynamic viscosity is independent of pressure, the slip correction factor depends on pressure and on particle diameter. For air, the slip correction factor can be calculated for different pressures using the following equation [53]:

$$C_c = 1 + \frac{1}{pd_p} [15.60 + 7.00 \exp(-0.059pd_p)] \quad (\text{B.5})$$

where p is the absolute pressure in kPa and d_p the particle diameter in μm .

According to this set of equations the particle diffusive wall losses could be estimated for different experimental conditions as shown in the following sections. In each experimental case the Reynold's number (Re) was first calculated to assure laminar flow conditions ($Re < 2300$). To this end, air flow along the sampling line was considered and the following equation was applied:

$$Re = \frac{\rho \dot{V} d_i}{S_i \eta} \quad (\text{B.6})$$

where ρ is the density of the gas, \dot{V} the volumetric flow, d_i the tube (sampling line) inner diameter and S_i the cross section of the tube.

When a temperature gradient is established in a gas, an aerosol particle experiences a force in the direction of decreasing temperature [53]. This effect is called thermophoresis. For small particles the velocity of thermophoresis V_{th} is given by Waldmann and Schmitt [109] as

$$V_{th} = \frac{-0.55\eta \nabla T}{\rho T_p} \quad \text{for } d_p < \lambda \quad (\text{B.7})$$

where ∇T is the temperature gradient, T_p the absolute temperature of the particles and λ the gas mean free path.

Unfortunately, the calculation of thermophoretic losses in the sampling line is complicated due to lack of knowledge on the thermal gradients across the sample probe. Thus, just a crude estimation can be carried out. To this end, the temperature gradient is calculated considering an average gas temperature in the center of the sampling line ($\bar{T}_c = \frac{T_1 - T_L}{2}$) and an average ambient temperature of $25^\circ C$. T_1 and T_L are measured

using thermocouples (see figures 4.1 and 3.1). Additionally, the absolute temperature of the particles is considered to be equal to \bar{T}_c . For simplification, once again, the flow gas mixture is assumed to be air and its density is calculated considering average pressure and temperature values.

The obtained thermophoretic velocity is used to calculate the radial distance (x_{th}) that particles cover during the estimated residence time in the sampling line.

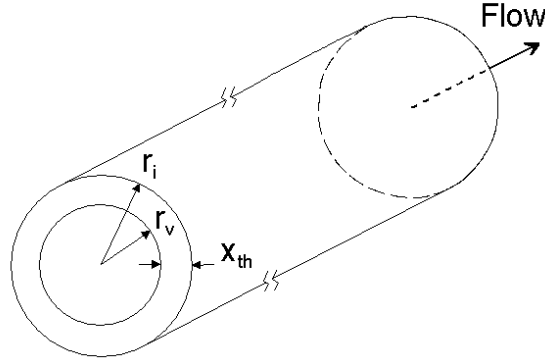


Figure B.3.: Schematic representation of the sampling line.

Considering that all particles reaching the wall adhere to it, the fractional loss due to thermophoresis results from:

$$\text{Thermophoretic Fractional Loss} = \frac{S_i - S_v}{S_i} \quad (\text{B.8})$$

where S_i is the original cross section of the sampling line and S_v the virtual cross section of the sampling line filled up with particles that will not reach the wall of the sampling line. Considering the corresponding circular cross section ($S = \pi r^2$) and $r_v = r_i - x_{th}$:

$$\text{Thermophoretic Fractional Loss} = \frac{2x_{th}}{r} - \left(\frac{x_{th}}{r}\right)^2 \quad (\text{B.9})$$

This set of equations is used to calculate the diffusive and thermophoretic fractional losses for different experimental conditions. The obtained values are presented below and compared with the estimations made by means of mass spectrometry.

B.2.2. Variation of the Stoichiometry

A similar experiment as the one described in section B.1 is carried out using the low pressure burner. In this case, it is attempted to isolate the effect of particle losses due to diffusion and thermophoresis (wall effects) allowing a better estimation of their extent.

The idea of the experiment is that by changing the stoichiometry of the flame the relative contribution of coagulation, wall effects and particle growth in the sampling line can be varied.

The rate of change of the number concentration of soot precursor particles due to coagulation and wall effects can be expressed using an extended version of the Smoluchowski equation (see equation 4.1) as follows:

$$\frac{dN_i}{dt} = -K_i \cdot N_i^2 - N_i \sum_{j=1, j \neq i}^{\infty} K_{ji} N_j - K_{Wall} \cdot N_i \quad (\text{B.10})$$

where the subindex i represents soot precursor particles and the subindex j represents soot particles, i.e. two classes of particles are considered.

The term $-K_i N_i^2$ describes reasonably the loss of soot precursor particles due to coagulation within the class (monodisperse coagulation), as explained in chapter 4.1. The term $N_i \sum_{j=1, j \neq i}^{\infty} K_{ji} N_j$ describes the loss of soot precursor particles due to coagulation with larger particles (soot), i.e. due to polydisperse coagulation. The last term $-K_{Wall} N_i$ represents the particle losses due to the interaction between the particles and the wall.

As shown in section 6.1.2 higher soot precursor particle concentrations are in general obtained for richer flames. In addition, higher concentrations of soot particles are expected. This increases inevitably the rate of coagulation since it is strongly concentration dependent (quadratic as shown in equation B.10). Moreover, also higher concentrations of gas phase species (PAHs) are expected the richer the flame. This favors particle growth due to adsorption of PAHs.

On the contrary, for not too rich flames the loss of precursor particles due to coagulation should be small. In addition, due to initial low concentrations of PAHs, particle growth can be probably switched off. In this case, the global extent of wall particle losses may be estimated by comparing the particle mass distributions (intensity variation) obtained for two different sampling line lengths (different residence times).

To this end the measurements presented in section 6.1.1 are repeated under the same experimental conditions (160 *mbar*) except for the increased length of the tubing connecting the low pressure burner and the MS. This means that the tube length of 25 *cm* of the earlier experiment is increased to 80 *cm*. By so doing only a minor change of the viscous pressure drop occurs so that the data referring to different residence times are directly comparable.

Some results are presented in figure B.4. Here the corresponding residence time of the sample in the sampling line is additionally indicated. This residence time is estimated using equations 4.5, 4.8 and 4.10. Air flow along the sampling line is assumed together with an initial sample temperature of 2700 *K* (adiabatic flame temperature of an ethylene/oxygen flame at $\Phi = 2.50$ and atmospheric pressure [81]). The latter is a good approximation since the adiabatic flame temperature is just slightly pressure dependent. The cooling of the sample due to the expansion through the ceramic nozzle is taken into account using equation 4.11. The pressure above the solenoid valve at the end of the sampling line remained constant for all measurements and thus $p_L = 15$ *mbar*. Considering all these simplifications, the calculated volume flow through the ceramic nozzle

$\dot{V} = 0.50 \text{ L/min}$ is in good agreement with the measured flow (0.60 L/min) downstream of the sampling line forepump.

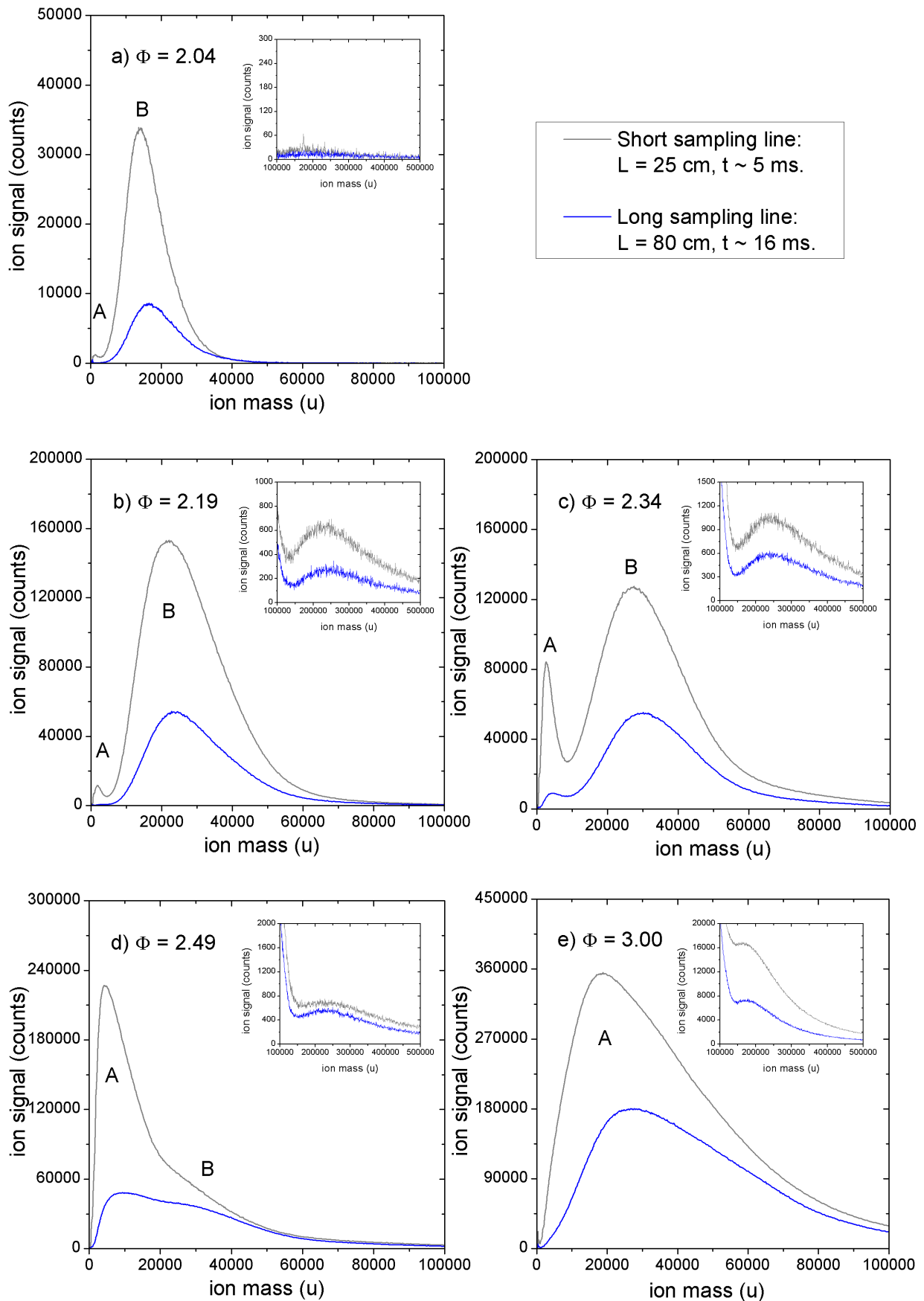


Figure B.4.: Average particle mass distributions in a premixed ethylene/oxygen flame at 160 mbar for two different sampling line lengths. a) $\Phi = 2.04$. b) $\Phi = 2.19$. c) $\Phi = 2.34$. d) $\Phi = 2.49$. e) $\Phi = 3.00$ and reduced MCP voltage. Note the different scales of the y axes.

For all stoichiometries between $2.04 \leq \Phi \leq 2.49$ a clear intensity decay is observed below 100000 u when comparing the "short" and the "long" sampling line measurements. In this stoichiometry range, the particle mass distributions do not show any significant shift towards larger masses with increasing length of the sampling line indicating that there is no significant particle growth and coagulation among soot precursor particles.

At $\Phi > 2.49$ the particle mass distributions below 100000 u show not only a decay in signal intensity but also a shift towards larger masses for a increased residence time in the sampling line. This shift is a clear indicator of the onset of surface growth and coagulation of soot precursor particles. In this range, coagulation of soot precursor particles with primary soot particles probably becomes also important. Thus the observed intensity decay is a combined consequence of wall losses and coagulation.

The soot precursor particle losses along the sampling line are estimated using this set of measurements. For this purpose the relative change in intensity of the maximum of each of the observed modes (mode A and B) is considered when particle growth and coagulation among soot precursor particles can be neglected and coagulation with large particles is also considered small ($2.04 \leq \Phi \leq 2.49$). Thus this fractional particle losses, labeled as experimental total fractional loss, are calculated for $\Delta L = 55 \text{ cm}$ following the expression

$$Exp. Fract. Loss = \frac{N_{in} - N_{out}}{N_{in}} = \frac{S_{Short \text{ s. line}} - S_{Long \text{ s. line}}}{S_{Short \text{ s. line}}} \quad (B.11)$$

where S is the maximal signal intensity of each mode. The results are shown in tables B.1 and B.2.

In addition, a theoretical fractional particle loss is calculated taking into account diffusive and thermophoretic processes. To this end, the mass data at maximal intensity for each of the observed modes are transformed to particle diameter (see section 8.2). Complementary, experimental data like \bar{T} , \bar{p} , \dot{V} and ΔL are considered. The resulting diffusive and thermophoretic fractional losses are also summarized in tables B.1 and B.2. The theoretical fractional loss arises from the sum of diffusive and thermophoretic fractional losses.

Φ	d_p	Exp. Total Fractional Loss	Diffusive Fractional Loss	Thermophoretic Fractional Loss	Theoretical Fractional Loss
(-)	(nm)	(%)	(%)	(%)	(%)
2.34	1.9	89	68	12	80
2.49	2.3	79	57	12	69

Table B.1.: Experimental and theoretic (diffusive and thermophoretic) fractional loss of soot precursor particles (mode A) at different equivalence ratios.

As expected from the theory, the diffusive wall particle losses strongly depend on particle size and decrease for increasing d_p . The thermophoretic particle losses, however, are

Φ	d_p	Exp. Total Fractional Loss	Diffusive Fractional Loss	Thermophoretic Fractional Loss	Theoretical Fractional Loss
(-)	(nm)	(%)	(%)	(%)	(%)
2.04	3.3	75	39	12	51
2.19	3.9	64	32	12	44
2.34	4.2	57	29	12	41

Table B.2.: Experimental and theoretic (diffusive and thermophoretic) fractional loss of soot precursor particles (mode B) at different equivalence ratios.

independent from particle size when $d_p < \lambda$ and therefore for all cases equal to 12%. The addition of both effects is also particle size dependent and, consequently, the theoretic fractional loss reflects this trend.

The experimental total fractional loss shows higher values than the calculated theoretic fractional loss. This could indicate that the loss of soot precursor particles due to coagulation with soot particles is probably not completely negligible in this stoichiometry range even if soot concentration is expected to be low. Nevertheless, for this set of measurements the particle loss due to diffusive and thermophoretic effects seem to be the dominating effect.

For the sake of completeness the same experiment is carried out at 120 *mbar*. This time the measurements presented in section 6.1.2 are repeated under the same experimental conditions except for the increased length of the sampling line, now 80 *cm*. The residence time of the sample in the sampling line is estimated as explained above. The calculated volume flow through the ceramic nozzle $\dot{V} = 0.37$ *L/min* is once again in good agreement with the measured flow (0.35 *L/min*) downstream of the sampling line forepump. Some of the results are shown in figure B.5.

In this series of measurements, as for the measurements shown in figure B.4, a decay in signal intensity is observed when comparing the measurements carried out with the short sampling line to the ones carried out with the longer line. The measurements at $\Phi = 2.19$, however, do not follow the general trend. The low signal intensities under these experimental conditions suggest that uncertainties in the signal transmission could play a role and thus these measurements can be considered as an outlier.

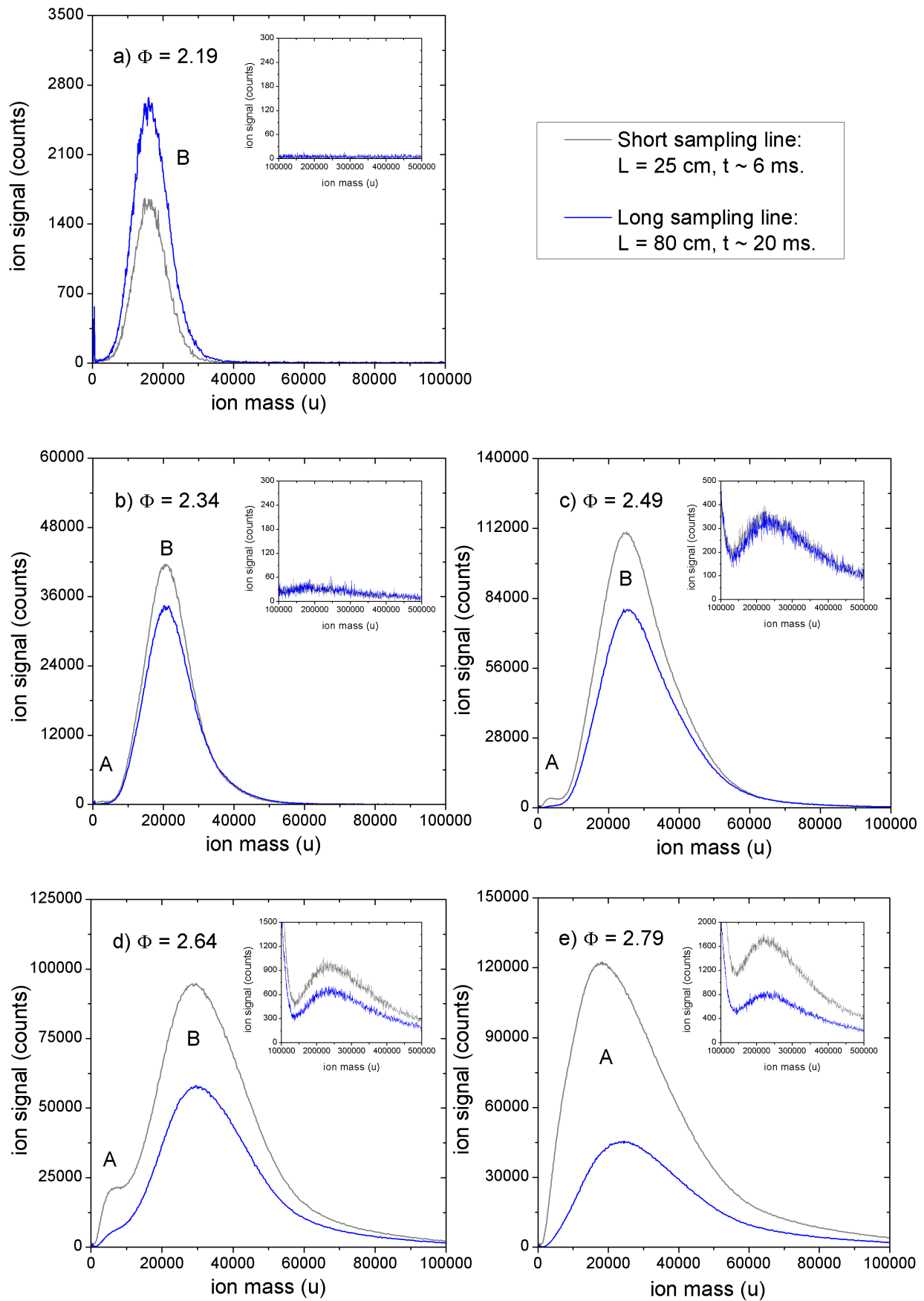


Figure B.5.: Average particle mass distributions in a premixed ethylene/oxygen flame at 120 mbar for two different sampling line lengths. a) $\Phi = 2.19$. b) $\Phi = 2.34$. c) $\Phi = 2.49$. d) $\Phi = 2.64$. e) $\Phi = 2.79$. Note the different scales of the y axes.

For this set of measurements the stoichiometry above which significant surface growth and coagulation effects are observed is $\Phi = 2.64$. This value is slightly higher than in the case of the 160 *mbar* flame due to the shift of the soot threshold, as explained in section 6.1.2.

For all stoichiometries between $2.19 \leq \Phi \leq 2.64$ just an intensity loss is observed when comparing the "short" and the "long" sampling line measurements. This reflects the effect of diffusive and thermophoretic particle wall losses together with the effect of polydisperse coagulation.

The experimental total fractional loss of soot precursor particles as well as the theoretic fractional loss are calculated as previously explained. In this case the dependence of particle losses on particle diameter, as expected from the theory, is not observed in the obtained experimental total fractional loss: While the theoretical losses decrease with increasing particle diameter due to the reduced diffusive loss, the experimental fractional loss shows an increase. Additionally, a general overestimation is found when calculating the theoretic fractional loss.

Both points are in disagreement with the results explained above for the measurements carried out at 160 *mbar*. At 160 *mbar* the experimental fractional loss shows the trend expected from the theory (a decay with increasing particle size) and, moreover, the calculated theoretic fractional loss is lower than the experimental total fractional loss.

Φ (-)	d_p (<i>nm</i>)	Exp. Total Fractional Loss (%)	Diffusive Fractional Loss (%)	Thermophoretic Fractional Loss (%)	Theoretic Fractional Loss (%)
2.34	3.8	18	44	17	61
2.49	4.0	28	42	17	59
2.64	4.3	39	39	17	56

Table B.3.: Experimental and theoretic (diffusive and thermophoretic) fractional loss of soot precursor particles (mode B) at different equivalence ratios.

Since differences in the sticking coefficient are not expected between the particles measured at 160 *mbar* and the ones sampled at 120 *mbar*, the disagreement between both series of measurements cast doubt on the reliability of the experimental data. The measurements presented above show intensity fluctuations as large as $\pm 30\%$ and consequently the calculated experimental total fractional loss can just be considered a crude approximation.

These measurements, however, indicate that particle losses are not negligible. Assuming significant sticking coefficients, diffusion, thermophoresis and coagulation with soot particles are the responsible driving forces leading to soot precursor particle losses. Due to these particle losses short sampling lines are in any case advisable. The main characteristics of the measured particle mass distributions remain observable for sampling line lengths above 1 *m*.

List of Figures

1.1.	World primary energy consumption of 2005 [3].	16
1.2.	History and projections of the world total primary energy consumption [4].	17
1.3.	Rough picture for soot formation as published by Bockhorn [16].	20
2.1.	Schematic diagram of the arrangement of the TOF-MS.	23
2.2.	Mass spectra of an ethylene/air flame. a) Continuous extraction. b) Pulsed extraction with time lag focusing. Note: Only narrow portions of the spectra are shown.	24
2.3.	Schematic representation of the pulsed sampling system coupled to the TOF-MS.	26
2.4.	Schematic representation of the two different arrangements of the sampling system. a) Cross arrangement. b) Axial arrangement.	29
2.5.	Mass spectra of an ethylene/air flame at different pressures at the valve entrance. a) Ionization volume adjusted to the axis of the ion optics. b) Ionization volume displaced 4 mm in the direction of the molecular beam.	30
2.6.	Schematic representation of the signal processing chain.	32
3.1.	Schematic representation of the low pressure burner coupled to the TOF-MS.	36
4.1.	Schematic representation of the sampling line.	40
4.2.	Residence time (t), pressure at the tip of the probe (p_0) and resulting expansion ratio ($E = \frac{p_{Flame}}{p_0} \cdot \frac{T_0}{T_{Flame}}$) calculated for different inner diameters of the sampling line.	42
4.3.	Particle mass distributions as a function of sample temperature. Source is an ethylene/air flame ($\Phi = 1.98$, Burner II) at atmospheric pressure. The original spectra are smoothed for clarity.	44
4.4.	Schematic diagram of the modified ionization chamber.	47
5.1.	Relationship between electron energy and degree of ionization for a mass spectrometer with an electron impact ion source as published by Middleditch [79].	48
5.2.	Particle mass spectra from a premixed ethylene/air flame ($\Phi = 2.1$, Burner I) at atmospheric pressure and different laser power densities. a) Low mass range from 500 to 100000 u . b) Upper mass range from 100000 to 500000 u .	51

5.3. Mass spectra of a premixed ethylene/air flame ($\Phi = 2.1$, Burner I) at atmospheric pressure at different MCP operation voltage. At MCP = 10 kV saturation effects are observed.	52
5.4. Particle mass spectra of a premixed ethylene/air flame ($\Phi = 2.1$, Burner I) at atmospheric pressure and two different laser power intensities.	53
6.1. Average particle mass distributions in a premixed flame at atmospheric pressure (Burner I) and different equivalence ratios. a) $\Phi = 1.76$. b) $\Phi = 1.80$. c) $\Phi = 1.85$. d) $\Phi = 1.89$. e) $\Phi = 2.01$. f) $\Phi = 2.28$. Note the different scales of the y axis.	57
6.2. Evolution of the particle mass distributions in a premixed flame at atmospheric pressure ($\Phi = 1.80$, Burner I) for different heights above the burner. Note the different scales of the y axis.	58
6.3. Evolution of the particle mass distributions in a premixed flame at atmospheric pressure ($\Phi = 2.10$, Burner I) for different heights above the burner. Note the different scales of the y axes.	59
6.4. Simplified representation of a resonant two photon ionization. Note that not all possible energy transfer pathways like spontaneous emission (fluorescence), intramolecular internal conversion, etc. have been represented.	61
6.5. a) Evolution of the particle mass distributions for different laser power densities ranging from 0.05 to 0.79 MW/cm ² (smoothed). b) Dependence of signal intensities of mode B (peaking at 20000 u) on the laser power density. Source: Premixed ethylene/air flame ($\Phi = 1.85$, Burner I) at atmospheric pressure.	62
6.6. a) Evolution of the particle mass distributions for different laser power densities ranging from 0.67 to 8.40 MW/cm ² (smoothed). b) Corresponding dependence of signal intensities of mode B (at 20000 u) on the laser power density. Source: Premixed ethylene/air flame ($\Phi = 1.85$, Burner I) at atmospheric pressure.	62
6.7. Dependence of normalized signal intensities of mode B (at 20000 u) on the laser power density. Source: Premixed ethylene/air flame ($\Phi = 1.85$, Burner I) at atmospheric pressure.	63
6.8. Dependence of signal intensities of a) mode A (25000 u) and b) mode C (215000 u) on the laser power density. Source: Premixed ethylene/air flame ($\Phi = 2.1$, Burner I) at atmospheric pressure.	64
6.9. Evolution of the ion mass distributions along the axis of a premixed ethylene/air flame ($\Phi = 1.80$, Burner II). The flame is stabilized by means of a 70 L/min shroud of nitrogen.	65
6.10. Evolution of the ion mass distributions along the axis of a premixed ethylene/air flame ($\Phi = 1.80$, Burner II). The flame was stabilized by means of a 70 L/min shroud of nitrogen. A background measurement is included.	66

6.11. Evolution of the ion mass distributions along the axis of a premixed ethylene/air flame ($\Phi = 1.80$, Burner II). The flame was stabilized by means of a 70 <i>L/min</i> shroud of compressed air.	67
6.12. Mass weighted integrals of soot precursor particles along the axis of a co-flow stabilized ethylene/air flame ($\Phi = 1.80$, Burner II). The flame edge at $HAB = 40$ <i>mm</i> is indicated.	68
6.13. Average particle mass distributions in a premixed ethylene/oxygen flame at 160 <i>mbar</i> and different equivalence ratios. a) $\Phi = 1.89$. b) $\Phi = 2.04$. c) $\Phi = 2.19$. d) $\Phi = 2.34$. e) $\Phi = 2.49$. f) $\Phi = 3.00$ and reduced MCP voltage. Note the different scales of the y axes.	70
6.14. Average particle mass distributions in a premixed ethylene/oxygen flame at 120 <i>mbar</i> and different equivalence ratios. a) $\Phi = 2.04$. b) $\Phi = 2.19$. c) $\Phi = 2.34$. d) $\Phi = 2.49$. e) $\Phi = 2.64$. f) $\Phi = 2.79$. Note the different scales of the y axis.	73
7.1. Number concentration and diameter of soot particles measured by EEPS in the exhaust gas of a diesel power generator at idle and 4 <i>kW</i> load operating conditions.	78
7.2. Number concentration and diameter of soot particles measured by EEPS in the exhaust gas of a gasoline power generator at idle and 4 <i>kW</i> load operating conditions.	78
7.3. Particle mass spectra of the exhaust gas of a diesel power generator at different operating conditions.	79
7.4. Particle mass spectra of the exhaust gas of a diesel power generator at different operating conditions. Measurements carried out under fragmenting ionization conditions.	80
7.5. Particle mass spectra of the exhaust gas of a gasoline power generator at different operating conditions.	81
7.6. Particle mass spectra of the exhaust gas of a gasoline power generator at different operating conditions. Measurements carried out under fragmenting ionization conditions.	81
8.1. Effect of data recording by means of time bins of constant width on the particle mass distribution. Source of the measured distribution: Premixed ethylene/air flame at atmospheric pressure, $\Phi = 1.85$ and $HAB = 12$ <i>mm</i>	85
8.2. Mean particle diameter at different equivalence ratios in a premixed flame at atmospheric pressure as obtained by means of MS.	87
8.3. Mean particle diameter at different heights above the burner in a premixed flame at atmospheric pressure as obtained by means of MS. a) $\Phi = 1.85$. b) $\Phi = 2.10$	87

8.4.	Mean particle diameter data obtained by means of laser induced incandescence in a premixed flame at atmospheric pressure a) at different equivalence ratios and $HAB = 12\text{ mm}$ and b) at different heights above the burner and $\Phi = 2.10$	89
8.5.	Mass weighted integrals of soot precursor particles for different stoichiometries. Source: Premixed ethylene/air flame at atmospheric pressure.	98
8.6.	Mass weighted integrals of soot precursor particles for different stoichiometries. Source: Premixed ethylene/oxygen flame at 120 mbar	99
A.1.	Cold trap set-up.	104
A.2.	Collecting efficiency of the cold trap system as a function of the sampling flow rate. Source: Ethylene/air premixed flame (Burner II).	108
A.3.	Estimated soot precursor particle mass concentration as a function of the flame stoichiometry. Source: Ethylene/oxygen flame at 120 mbar	112
A.4.	Dose-response curves of the bacterial SWITCH test for wet samples of soot precursor particles (cold trap I) obtained from an ethylene/oxygen premixed flame at 120 mbar and different burning stoichiometries (Φ). a) Relative luminescence. b) Relative fluorescence. c) Relative absorbance.	118
A.5.	Dose-response curves of the bacterial SWITCH test for wet samples of soot precursor particles (cold trap I) obtained from a diesel engine at different operating conditions. a) Relative luminescence. b) Relative fluorescence. c) Relative absorbance.	120
B.1.	Evolution of soot precursor particle and primary soot particle profiles in a sampling line of variable length. Source is an ethylene/air flame ($\Phi = 2.2$) at atmospheric pressure. The length of the sampling line and the corresponding calculated residence times are indicated.	122
B.2.	Evolution of soot precursor particle and primary soot particle profiles in a sampling line of variable length. Source is an ethylene/air flame ($\Phi = 1.9$) at atmospheric pressure. The length of the sampling line and the corresponding residence times are indicated. The represented curves are averages of several measurements.	123
B.3.	Schematic representation of the sampling line.	126
B.4.	Average particle mass distributions in a premixed ethylene/oxygen flame at 160 mbar for two different sampling line lengths. a) $\Phi = 2.04$. b) $\Phi = 2.19$. c) $\Phi = 2.34$. d) $\Phi = 2.49$. e) $\Phi = 3.00$ and reduced MCP voltage. Note the different scales of the y axes.	129
B.5.	Average particle mass distributions in a premixed ethylene/oxygen flame at 120 mbar for two different sampling line lengths. a) $\Phi = 2.19$. b) $\Phi = 2.34$. c) $\Phi = 2.49$. d) $\Phi = 2.64$. e) $\Phi = 2.79$. Note the different scales of the y axes.	132

List of Tables

8.1. Experimental results on the nature of soot precursor particles as reported by D'Alessio et al. and Dobbins et al.	94
8.2. Calculated adiabatic flame temperatures for different flames [81].	96
8.3. Main characteristics of the different soot precursor particles detected in the current work.	97
A.1. Results of TOC analysis for different sampling flow rates. Source: Ethylene/air premixed flame at $\Phi = 1.9$ (Burner II). Filter interference $\sim 11 \mu\text{g}/\text{mL } C$	107
A.2. Results of TOC analysis for different sampling flow rates. Source: Ethylene/air premixed flame at $\Phi = 2.2$ (Burner II). Filter interference $\sim 11 \mu\text{g}/\text{mL } C$	107
A.3. Number concentration of soot precursor particles in two different ethylene/air flames at atmospheric pressure ($HAB = 12 \text{ mm}$, Burner II).	110
A.4. Results of TOC analysis for different Φ . Source: Ethylene/oxygen premixed flame at 120 mbar . Filter interference $\sim 30 \mu\text{g}/\text{mL}$	111
A.5. Mass concentration of soot precursor particles in an ethylene/oxygen flame at 120 mbar as a function of Φ . Filter interference $\sim 30 \mu\text{g}/\text{mL}$	112
A.6. Results of TOC analysis for different operating conditions of the diesel engine. Filter interference $\sim 30 \mu\text{g}/\text{mL}$	113
A.7. Results of TOC analysis for different operating conditions of the gasoline engine. Filter interference $\sim 11 \mu\text{g}/\text{mL}$	113
B.1. Experimental and theoretic (diffusive and thermophoretic) fractional loss of soot precursor particles (mode A) at different equivalence ratios.	130
B.2. Experimental and theoretic (diffusive and thermophoretic) fractional loss of soot precursor particles (mode B) at different equivalence ratios.	131
B.3. Experimental and theoretic (diffusive and thermophoretic) fractional loss of soot precursor particles (mode B) at different equivalence ratios.	133

Bibliography

- [1] Standard reference database of the National Institute of Standards and Technology. NIST Chemistry WebBook: <http://webbook.nist.gov/chemistry/>, 2005.
- [2] Crude oil, the supply outlook. Energy Watch Group, 2007.
- [3] *International Energy Annual 2005*. Energy Information Administration, U.S. Department of Energy, 2007.
- [4] *International Energy Outlook 2007*. Energy Information Administration, U.S. Department of Energy, 2007.
- [5] *Newsletter 80*. The Association for the Study of Peak Oil and Gas (ASPO), 2007.
- [6] *Vision ein Schweizer Energieversorgung mit Zukunft: Ressourcen und Technologien, Grünbuch 2007*. Ökozentrum Langebruck, 2007.
- [7] J.B. Anderson. Molecular beams and low density gasdynamics. In P.P. Wegener, editor, *Gasdynamics*, volume 4. Marcel Dekker, INC., 1974.
- [8] J.B. Anderson, R.P. Andres, and J.B. Fenn. Supersonic nozzle beams. In *Advances in Chemical Physics*, volume 10, chapter 8, pages 275–317. 1966.
- [9] B. Atakan, A.T. Hartlieb, J. Brand, and K. Kohse-Höinghaus. An experimental investigation of premixed fuel-rich low pressure propene/oxygen/argon flames by laser spectroscopy and molecular-beam mass spectrometry. *Twenty-Seventh Symposium (International) on Combustion*, 27, Issue 1:435–444, 1998.
- [10] A.C. Barone, A. D'Alessio, and A. D'Anna. Morphological characterization of the early process of soot formation by atomic force microscopy. *Combust. Flame*, 132:181–187, 2003.
- [11] C. Baumstark-Khan, K. Cioara, P. Rettberg, and G. Horneck. Determination of geno- and cytotoxicity of groundwater and sediments using the recombinant SWITCH test. *J. Environ. Sci. and Health*, pages 245–263, 2005.
- [12] C. Baumstark-Khan, C.E. Hellweg, and N. Stojicic. Institute of Aerospace Medicine, DLR, Köln. Private communication.
- [13] C. Baumstark-Khan, R.A. Khan, P. Rettberg, and G. Horneck. Bacterial *Lux-Fluoro* test for biological assessment of pollutants in water samples from urban and rural origin. *Anal. Chim. Acta*, 487:51–60, 2003.

- [14] Y. Le Beyec. Cluster impacts at *keV* and *MeV* energies: Secondary emission phenomena. *Int. J. Mass Spectrom. Ion Proc.*, 174:101–117, 1998. And citations therein.
- [15] R. Bähnisch. Electronic laboratory, DLR, Stuttgart. Private communication.
- [16] H. Bockhorn. A short introduction to the problem. In H. Bockhorn, editor, *Soot Formation in Combustion*, pages 3–7. Springer-Verlag, 1994.
- [17] K. Bruhn. Untersuchungen zur Temperatur- und Druckabhängigkeit der Rußbildung in vorgemischten laminaren Ethylen-Luft Flammen. Master’s thesis, Institut für Physikalische Chemie, Georg-August-Universität, Göttingen, 1988.
- [18] H. Burtscher, U. Baltensperger, N. Bukowiecki, P. Cohn, C. Hüglin, M. Mohr, U. Matter, S. Nyeki, V. Schmatloch, N. Streit, and E. Weingartner. Separation of volatile and non-volatile aerosol fractions by thermodesorption: Instrumental development and applications. *J. Aerosol Sci.*, 32:427–442, 2001.
- [19] H. Burtscher, L. Scherrer, H.C. Siegmann, A. Schmidt-Ott, and B. Federer. Probing aerosols by photoelectric charging. *J. Appl. Phys.*, 53:3787–3791, 1982.
- [20] H. Burtscher and A. Schmidt-Ott. In situ measurement of adsorption and condensation of a polyaromatic hydrocarbon on ultrafine C particles by means of photoemission. *J. Aerosol Sci.*, 17:699–703, 1986.
- [21] H. Burtscher and H.C. Siegmann. Monitoring of PAH-emissions from combustion processes by photoelectric charging. *J. Aerosol Sci.*, 101:327–332, 1994.
- [22] R. Campargue. High intensity supersonic molecular beam apparatus. In J.H. De Leeuw, editor, *Rarefied Gas Dynamics*, volume 2 of *4th Symposium*, pages 279–298. Academic Press, 1966.
- [23] R. Campargue. Progress in overexpanded supersonic jets and skimmed molecular beams in free-jet zones of silence. *J. Phys. Chem.*, 88:4466–4474, 1984.
- [24] C.J. Campbell and J.H. Laherrere. The end of cheap oil. *Scientific American*, 1998.
- [25] H.X. Chen and R.A. Dobbins. Crystallogenesis of particles formed in hydrocarbon combustion. *Combust. Sci. Technol.*, 159:109–128, 2000.
- [26] S.A. Ciatti, J.P. Hessler, K.O. Lee, A.M. Tentner, and J. Zhu. Investigation of nano-particulate production from low temperature combustion. *SAE 2005-01-0128*, pages 125–134, 2005.
- [27] A. D’Alessio, A. D’Anna, A. D’Orsi, P. Minutolo, R. Barbella, and A. Ciajolo. Precursor formation and soot inception in premixed ethylene flames. *Twenty-Fourth Symposium (International) on Combustion*, pages 973–980, 1992.

-
- [28] A. D'Alessio, A. D'Anna, G. Gambi, and P. Minutolo. The spectroscopic characterisation of UV absorbing nanoparticles in fuel rich soot forming flames. *J. Aerosol. Sci.*, 29:397–409, 1998.
- [29] A. D'Alessio, A. D'Anna, P. Minutolo, L.A. Sgro, and A. Violi. On the importance of surface growth in soot formation in premixed flames. *Proc. Combust. Inst.*, 28:2547–2554, 2000.
- [30] R.A. Dobbins. Soot inception temperature and the carbonization rate of precursor particles. *Combust. Flame*, 130:204–214, 2002.
- [31] R.A. Dobbins. Hydrocarbon nanoparticles formed in flames and diesel engines. *Aerosol Sci. and Tech.*, 41:485–496, 2007.
- [32] R.A. Dobbins, R.A. Fletcher, and H.-C. Chang. The evolution of soot precursor particles in a diffusion flame. *Combust. Flame*, 115:285–298, 1998.
- [33] R.A. Dobbins, R.A. Fletcher, and W. Lu. Laser microprobe analysis of soot precursor particles and carbonaceous soot. *Combust. Flame*, 100:301–309, 1995.
- [34] R.A. Dobbins and H. Subramaniasivam. Soot precursor particles in flames. In H. Bockhorn, editor, *Soot Formation in Combustion*, pages 290–301. Springer-Verlag, 1994.
- [35] J.L. Franklin, J.G. Dillard, H.M. Rosenstock, J.T. Herron, K. Draxl, and F.H. Field. *Ionization potentials, appearance potentials and heats of formation of gaseous positive ions*. National Standard Reference Data System, 1969.
- [36] G.W. Fraser. The ion detection efficiency of microchannel plates (MCPs). *Int. J. Mass Spectrom.*, 215:13–30, 2002.
- [37] M. Frenklach and H. Wang. Detailed modelling of soot particle nucleation and growth. *Twenty-Third Symposium (International) on Combustion*, pages 1559–1566, 1990.
- [38] M. Frenklach and H. Wang. Detailed mechanism and modelling of soot particle formation. In H. Bockhorn, editor, *Soot Formation in Combustion*, pages 292–301. Springer-Verlag, 1994.
- [39] Sheldon K. Friedlander. *Smoke, Dust and, Haze: Fundamentals of aerosol dynamics*. Oxford University Press, 2000.
- [40] N.A. Fuchs. *The Mechanics of Aerosols*. Pergamon, 1964.
- [41] L. Fulcheri, Y. Schwob, F. Fabry, G. Flamant, L.F.P. Chibante, and D. Laplaze. Fullerene production in a 3-phase AC plasma process. *Carbon*, 38:797–803, 2000.

- [42] Roger Gilmont. *Thermodynamic Principles for Chemical Engineers*. Prentice Hall, Inc., 1959.
- [43] I.S. Gilmore and M.P. Seah. Ion detection efficiency in SIMS: Dependencies on energy, mass and composition for microchannel plates used in mass spectrometry. *Int. J. Mass Spectrom.*, 202:217–229, 2000.
- [44] Irvin Glassman. *Combustion*. Academic Press, 1977.
- [45] H.H. Grotheer. Institute of Combustion Technology, DLR, Stuttgart. Private communication.
- [46] J. Happold. Institute of Combustion Technology, DLR, Stuttgart. Private communication.
- [47] J. Happold. *Nanokristallite aus geschichteten polyzyklischen aromatischen Kohlenwasserstoffen als Bausteine der Rußbildung*. PhD thesis, Fakultät Luft- und Raumfahrttechnik und Geodäsie, Universität Stuttgart, 2007.
- [48] J. Happold, H.-H. Grotheer, and M. Aigner. Distinction of gaseous soot precursor molecules and soot precursor particles through photo ionization mass spectrometry. *Rapid Commun. Mass Spec.*, 21:1247–1254, 2007.
- [49] J.M. Hayes. Analytical spectroscopy in supersonic expansions. *Chem. Rev.*, 87:745–760, 1984.
- [50] B.S. Haynes and H.Gg. Wagner. Soot formation. *Prog. Energy Combust. Sci.*, 7:229–273, 1981.
- [51] Ch. Helsper. Probleme der Staubprobenahme bei der Filterprüfung. *Filtrieren und Separieren*, 1:1–7, 1995.
- [52] H. Hepp. *Large Molecules and Ultrasmall Particles in Diffusion Flames*. PhD thesis, Swiss Federal Institute of Technology, 1996.
- [53] William C. Hinds. *Aerosol Technology: Properties, behavior, and measurements of airborne particles*. John Wiley & Sons, Inc., 1999.
- [54] K.-H. Homann. Fullerenes and soot formation - New pathways to large particles in flames. *Angew. Chem. Int. Ed.*, 37:2434–2451, 1998.
- [55] K.-H. Homann and H. Wolf. Charged soot in low-pressure acetylene/oxygen flames. *Twenty-First Symposium (International) on Combustion*, 21:1013–1021, 1998.
- [56] T. Ishiguro, Y. Takatori, and K. Akihama. Microstructure of diesel soot particles probed by electron microscopy: First observation of inner core and outer shell. *Combust. Flame*, 108:231–234, 1997.

-
- [57] G.W. Israel and S.K. Friedlander. High-speed beams of small particles. *J. Colloid and Interface Sci.*, 24:330–337, 1967.
- [58] R.A.W. Johnstone and M.E. Rose. *Mass spectrometry for chemists and biochemists*. Cambridge University Press, second edition, 1996.
- [59] Stefan Kaesdorf. *Bedienungsanleitung des Massenspektrometers*, 2004.
- [60] S.R. Kanjarkar and C.Wahl. Institute of Combustion Technology, DLR, Stuttgart. Private communication.
- [61] A. Kantrowitz and J. Grey. A high intensity source for the molecular beam. *Rev. Sci. Instr.*, 22:328, 1951.
- [62] D.B. Kittelson. Engines and nanoparticles: A review. *J. Aerosol Sci.*, 29:575–588, 1998.
- [63] N. Klippel and T. Nussbaumer. Feinstaubbildung in Holzfeuerungen und Gesundheitsrelevanz von Holzstaub im Vergleich zu Dieseleruss. In *9. Holzenergie-Symposium*, pages 21–40. ETH Zürich, 2006.
- [64] R. Koppelaar. *World Oil Production & Peaking Outlook*. Peak Oil Netherlands Foundation, 2005.
- [65] R. Kovacs. *On-line Multi-Photonen-Ionisations-Massenspektrometrie an aromatischen Kohlenwasserstoffen und Fullerenen in Flammen*. PhD thesis, Technische Hochschule Darmstadt, 1996.
- [66] Lambda Physik. *User Manual OPTex*.
- [67] A. Lamprecht, B. Atakan, and K. Kohse-Höinghaus. Fuel-rich flame chemistry in low-pressure cyclopentene flames. *Twenty-Eighth Symposium (International) on Combustion*, 28, Issue 2:1817–1824, 2000.
- [68] Erich Leiter. *Strömungsmechanik nach Vorlesung von K. Oswatitsch*. Friedr. Vieweg & Sohn, 1978.
- [69] P. Liu, P.J. Ziemann, D.B. Kittelson, and P.H. McMurry. Generating particle beams of controlled dimensions and divergence: I. Theory of particle motion in aerodynamic lenses and nozzle expansions. *Aerosol Sci. Technol.*, 22:293–313, 1995.
- [70] P. Liu, P.J. Ziemann, D.B. Kittelson, and P.H. McMurry. Generating particle beams of controlled dimensions and divergence: II. Experimental evaluation of particle motion in aerodynamic lenses and nozzle expansions. *Aerosol Sci. Technol.*, 22:314–324, 1995.
- [71] David M. Lubman. *Lasers and Mass Spectrometry*. Oxford University Press, 1990.

- [72] B.A. Mamyrin, V.I. Karataev, D.V. Shmikk, and B.A. Zagulin. The mass-reflectron, a new nonmagnetic time-of-flight mass spectrometer with high resolution. *Sov. Phys.-JETP*, 37:45–48, 1973.
- [73] M.M. Maricq. Size and charge of soot particles in rich premixed ethylene flames. *Combust. Flame*, 137:340–350, 2004.
- [74] M.M. Maricq. A comparison of soot size and charge distributions from ethane, ethylene, acetylene, and benzene/ethylene premixed flames. *Combust. Flame*, 144:730–743, 2006.
- [75] T.P. Martin, T. Bergmann, U. Näher, H. Schaber, and U. Zimmermann. Detection of large fullerene clusters. *Nucl. Instr. and Meth. in Phys. Res. B*, 88:1–5, 1994.
- [76] C.S. McEnally, L.D. Pfefferle, B. Atakan, and K. Kohse-Höinghaus. Studies of aromatic hydrocarbon formation mechanisms in flames: Progress towards closing the fuel gap. *Progress in Energy and Combustion Science*, 32, Issue 3:247–294, 2006.
- [77] C.M. Megaridis and R.A. Dobbins. Comparison of soot growth and oxidation in smoking and non-smoking ethylene diffusion flames. *Combust. Sci. and Tech*, 66:1–16, 1989.
- [78] H.A. Michelsen. Understanding and predicting the temporal response of laser-induced incandescence from carbonaceous particles. *J. Chem. Phys.*, 118:7012–7045, 2003.
- [79] Brian S. Middleditch, editor. *Practical Mass Spectrometry*. Plenum Press, 1979.
- [80] P. Minutolo, G. Gambi, A. D’Alessio, and S. Carlucci. Spectroscopic characterisation of carbonaceous nanoparticles in premixed flames. *Atmospheric Environment*, 33:2725–2732, 1999.
- [81] Chris Morley. Gaseq: Chemical equilibria in perfect gas, Version 0.76. <http://www.gaseq.co.uk>.
- [82] I. Naydenova, M. Nullmeier, J. Warnatz, and P.A. Vlasov. Detailed kinetic modeling of soot formation during shock-tube pyrolysis of C_6H_6 : Direct comparison with the results of time-resolved laser-induced incandescence (LII) and CW-laser extinction measurements. *Combust. Sci. and Technol.*, 176:1667–1703, 2004.
- [83] R. Niessner. The chemical response of the photo-electric aerosol sensor (PAS) to different aerosol systems. *J. Aerosol Sci.*, 17:705–714, 1986.
- [84] R. Niessner, W. Robers, and P. Wilbring. Laboratory experiments on the determination of polycyclic aromatic hydrocarbon coverage of submicrometer particles by laser-induced aerosol photoemission. *Anal. Chem.*, 61:320–365, 1986.

- [85] R. Niessner and P. Wilbring. Ultrafine particles as trace catchers for polycyclic aromatic hydrocarbons: The photoelectric aerosol sensor as a tool for in situ sorption and desorption studies. *Anal. Chem.*, 61:708–714, 1989.
- [86] G. Oberdörster, E. Oberdörster, and J. Oberdörster. Nanotoxicology: An emerging discipline evolving from studies of ultrafine particles. *Environ. Health Perspect.*, 113:823–839, 2005.
- [87] H. Pokorny, M. Thierley, H.-H. Grotheer, and M. Aigner. The fast coagulation of combustion generated particles (NOC). In *Proc. European Combustion Meeting "ECM2005"*. The Combustion Institute, 2005.
- [88] L. Prandtl, K. Oswatitsch, and K. Wiegardt. *Führer durch die Strömungslehre*. Friedr. Vieweg & Sohn, 1990.
- [89] Robert Bosch GmbH. *Kraftfahrtechnisches Taschenbuch*, 24 edition, 2002.
- [90] E.A. Rohlfing, D.M. Cox, and A. Kaldor. Production and characterization of supersonic carbon cluster beams. *J. Chem. Phys.*, 81:3322–3330, 1984.
- [91] R.K. Schlüter. Messung von Nanopartikeln im Abgas von Verbrennungsmotoren mittels TOF-Massenspektrometrie. Master's thesis, Universität Stuttgart, 2005.
- [92] L.A. Sgro, G. Basile, A.C. Barone, A. D'Anna, P. Minutolo, A. Borghese, and A. D'Alessio. Detection of combustion formed nanoparticles. *Chemosphere*, 51:1079–1090, 2003.
- [93] L.A. Sgro, A. De Filippo, G. Lanzuolo, and A. D'Alessio. Characterization of nanoparticles of organic carbon (NOC) produced in rich premixed flames by differential mobility analysis. *Proc. Combust. Inst.*, 31:631–638, 2007.
- [94] L.A. Sgro, P. Minutolo, G. Basile, and A. D'Alessio. UV-visible spectrometry of organic carbon particulate sampled from ethylene/air flames. *Chemosphere*, 42:671–680, 2001.
- [95] Eran Sher, editor. *Handbook of Air Pollution from Internal Combustion Engines*. Academic Press, 1998.
- [96] K. Siegmann, H. Burtscher, and H. Hepp. PAH-Profiles and growth mechanism of soot particles in diffusion flames. *J. Aerosol Sci.*, 24, Suppl. 1:373–374, 2005.
- [97] V. Smil. Energy in the twentieth century: Resources, conversions, costs, uses, and consequences. *Rev. Energy Environ.*, 25:21–51, 2000.
- [98] Vaclav Smil. *Energy at the Crossroads: Global Perspectives and Uncertainties*. 2003.
- [99] S.E. Stein and A. Fahr. High-temperature stabilities of hydrocarbons. *J. Phys. Chem.*, 89:3714, 1985.

- [100] C.B. Stipe, J.H. Choi, D. Lucas, C.P. Koshland, and R.F. Sawyer. Nanoparticle production by UV irradiation of combustion generated soot particles. *J. of Nanoparticle Research*, 6:467–477, 2004.
- [101] R. Stirn, K.P. Geigle, and W. Meier. Institute of Combustion Technology, DLR, Stuttgart. Private communication.
- [102] J.W. Tester, E.M. Drake, M.J. Driscoll, M.W. Golay, and W.A. Peters. *Sustainable Energy: Choosing among the options*. Massachusetts Institute of Technology, 2005.
- [103] M. Thierley. *Charakterisierung von Nanopartikeln aus Verbrennungsprozessen*. PhD thesis, Fakultät Luft- und Raumfahrttechnik und Geodäsie, Universität Stuttgart, 2007.
- [104] M. Thierley, H.-H. Grotheer, M. Aigner, Z. Yang, A. Abid, B. Zhao, and H. Wang. On existence of nanoparticles below sooting threshold. *Proc. Combust. Inst.*, 31:639–647, 2007.
- [105] A. Violi. Modeling of soot particle inception in aromatic and aliphatic premixed flames. *Combust. Flame*, 139:279–287, 2004.
- [106] A. Violi, G.A. Voth, and A.F. Sarofim. Kinetic Monte Carlo-molecular dynamics approach to model soot inception. *Combust. Sci. Technol.*, 176:991–1005, 2004.
- [107] Walter Wagner. *Strömung und Druckverlust*. Vogel Verlag, 2001.
- [108] R.L. Vander Wal. Soot precursor carbonization: Visualization via simultaneous LIF-LII and characterization via TEM. *Twenty-Sixth Symposium (International) on Combustion*, pages 2269–2275, 1996.
- [109] L. Waldmann and K.H. Schmitt. Thermophoresis and diffusiophoresis of aerosols. In C. N. Davis, editor, *Aerosol Science*. Academic Press, London, 1966.
- [110] M. Weiss, P.J.T. Verheijen, J.C.M. Marijnissen, and B. Scarlett. On the performance of an on-line time-of-flight mass spectrometer for aerosols. *J. Aerosol Sci.*, 28:159–171, 1997.
- [111] B.L. Wersborg, J.B. Howard, and G.C. Williams. Physical mechanisms in carbon formation in flames. *Fourteenth Symposium (International) on Combustion*, pages 929–940, 1973.
- [112] W.C. Wiley and I.H. McLaren. Time-of-flight mass spectrometer with improved resolution. *Rev. Sci. Instr.*, 26(12):1150–1157, 1955.
- [113] B. Zhao, Z. Yang, Z. Li, M.V. Johnston, and H. Wang. Particle size distribution of incipient soot in laminar premixed ethylene flames: effect of flame temperature. *Proc. Combust. Inst.*, 30:1441–1448, 2005.

- [114] B. Zhao, Z. Yang, J. Wang, M.V. Johnston, and H. Wang. Analysis of soot nanoparticles in a laminar premixed ethylene flame by scanning mobility particle sizer. *Aerosol Sci. Technol.*, 37:611–620, 2003.
- [115] U. Zimmermann, U. Näher, S. Frank, T.P. Martin, and N. Malinowski. Characterization of a source of large clusters. In T.P. Martin, editor, *Large clusters of Atoms and Molecules*, pages 511–530. Kluwer Academic Publishers, 1996.